Magmatism and Metallogeny of the Astaneh-Nezam Abad Area, Sanandaj-Sirjan Zone, West-Central Iran

Doctoral Thesis
(Dissertation)

to be awarded the degree of

Doctor rerum naturalium (Dr. rer. nat.)

submitted by

MOHAMMAD ALI NEKOUVAGHT TAK

from Tehran, Iran

approved by the Faculty of Energy and Economic Sciences
Technical University of Clausthal

Date of oral examination
19 February 2008

Chairperson of the Board of Examiners: Prof. Dr. H. Y. Schenk-Mathes

Chief Reviewer: Prof. Dr. Bernd Lehmann

Reviewer: Prof. Dr. Kurt Mengel

This dissertation was undertaken at the Economic Geology Group of the Institute of Mineralogy and Mineral Resources of the Technical University of Clausthal.

The children of Humanity are each other's limbs
That share an origin in their creator
When one limb passes its days in pain
The other limbs cannot remain easy
You who feel no pain at the suffering of others
It is not fitting you be called human

Die Kinder Adams sind aus einem Stoff gemacht,
als Glieder eines Leibs von Gott, dem Herrn, erdacht.
Sobald ein Leid geschieht nur einem dieser Glieder,
dann klingt sein Schmerz sogleich in Ihnen allen wieder.
Ein Mensch, den nicht die Not der Menschenbrüder rührt,
verdient nicht, dass er noch des Menschen Namen führt
Saadi (1184-1283 AD)

To my family
and
memory of my father

Table of contents

Content Page

Acknowledgments IV

Abstract V

Chapter 1 1

1 Introduction 1

1.1 General 1

1.2 Objectives 1

1.3 Methodology 1

1.4 Regional geology 2

1.5 Economic geology 4

1.6 Geology of the Shazand quadrangle 5

Chapter 2 8

2 Magmatism 8

2.1 Petrography 8

2.1.1 Astaneh intrusion 8

2.1.2 Nezam Abad-Malmir complex 8

2.1.2.1 Granodiorite 9

2.1.2.2 Quartzdiorite-tonalite 9

2.1.2.3 Pegmatites 10

2.1.2.4 Aplite 10

2.1.3 Gousheh intrusion 11

2.1.4 Shirmazd Mountain 11

2.2 Geochemistry 11

2.2.1 Rock classification 11

2.2.2 Petrogenesis 11

2.2.2.1 Variation diagrams of major elements 14

2.2.2.2 Variation diagrams of trace elements 15

2.3 Classification of magma series 18

2.3.1 Alkalinity 18

2.3.2 Aluminosity 18

2.4 Tectonic setting 18

Content Page

2.5 Spider diagrams 18
2.6 Magnetite-ilmenite series and I-S type classification 22
2.7 Isotope data 23

Chapter 3 27
3 Nezam Abad tungsten ore deposit 27
3.1 Introduction 27
3.2 Mine geology 28
3.3 Vein mineralogy 29
3.4 Comments on scheelite, tourmaline and arsenopyrite 36
3.4.1 Scheelite 36
3.4.2 Tourmaline and the source of boron 40
3.4.3 Arsenopyrite 47
3.5 Hydrothermal alteration 47
3.6 Geochemistry of the ore deposit 51
3.7 Oxygen isotope data 52

Chapter 4 54
4 Astaneh gold prospect 54
4.1 Introduction 54
4.2 Geology of the prospect 55
4.3 Alteration 57
4.4 Mineralization 57
4.5 Ore mineralogy 57
4.6 Paragenetic sequence 64
4.7 Geochemistry 64
4.8 Isotope data 65

Chapter 5 67
5 Deh Hossein Sn-Au-Cu prospect 67
5.1 Introduction 67
5.2 Geology of the prospect 67
5.3 Alteration 68

Content Page

5.4 Mineralization 70
5.5 Ore mineralogy 70
5.6 Paragenetic sequence 76
5.7 More comments on sphalerite 76
5.8 Geochemistry 78
5.9 Isotope data 80

Chapter 6 81
6 Conclusion and proposed genetic model 81

References 86

Appendix 1 94
Appendix 2 97
Appendix 3 100
Appendix 4 101
Appendix 5 104
Appendix 6 105

Acknowledgments

This Ph.D thesis was supported by a research grant of German Academic Exchange Services (DAAD) for stay in Germany and studies at the Institute of Mineralogy and Mineral Resources, Technical University of Clausthal. I would like to thank, Prof. Bernd Lehmann for constructive comments throughout this research. I am obliged to express my gratitude for his careful scrutiny of the manuscript and patience to conduct this research to the end.

This research has benefitted scientifically and logistically from the following individuals:

Special acknowledgment must be made to Dr. Eike Gierth for his valuable support during ore microscopy study. Prof. Kurt Mengel is appreciated for constructive scientific discussions. Fred Türck and Ulf Hemmerling are thanked for computer assistance and sample preparation, respectively. Helga Vollbrecht is thanked for administrative support. I wish to appreciate the patience of Klaus Herrmann for his help with electron microprobe analysis.

Special thanks must go to Prof. Kamal Bazargani at Department of Geology, Tehran University, for his motivation and scientific discussions during the last 16 years. I wish to thank Eng. M. T. Korehee, chief of the Geological Survey of Iran, for providing necessary facilities during field work. Much credit is due to Eng. Hojat Jahangiri, expert of Geological Survey of Iran for immense help during field work and elucidating local geologic aspects of the study area. Eng. Ahmad Kazemi, former expert of the Remote Sensing department of the Geological Survey of Iran is acknowledged for processing of satellite images, collaboration during field work and constructive comments. I am sincerely grateful to my Ph.D colleagues who did not deny their kind assistance wherever and whenever it was needed.

Last but not least, I would like to express my everlasting gratitude to my wife, Arefeh, for her unlimited supports throughout our common life. Without her sacrifices, motivation and kindness this research would not have been materialized. My son, Dana, gave me energy and motivation by his birth, laugh and cry to overcome difficulties and fulfil this research.

Abstract

The Astaneh-Nezam Abad area is located in the NW-SE trending Sanandaj-Sirjan continental arc of west-central Iran. Mesozoic low-grade regional metamorphic rocks are intruded by Mid-Jurassic, Late Cretaceous and Eocene I-type, calc-alkaline, peraluminous to metaluminous felsic intrusions of ilmenite-series affinity. The dominantly crustal nature of this magmatism is indicated by initial $^{87}Sr/^{86}Sr$ ratios and ε_{Nd} values of 0.705-0.711 and -0.4 to -6.3 for the Astaneh granite/granodiorite and 0.707-0.712 and –3.2 to –6.4 for the Nezam Abad quartzdiorite, respectively.

The study area hosts three ore deposits/prospects: (1) The Nezam Abad tungsten deposit is of vein type with quartz-tourmaline W±Sn ± Au mineralization hosted by Eocene quartzdioritic units of the composite Nezam-Abad-Malmir intrusion. Ore minerals include scheelite, cassiterite, and a variety of sulfide minerals with locally high amounts of invisible gold. (2) The Astaneh gold prospect consists of gold-bearing quartz-pyrite-chalcopyrite-arsenopyrite veins and disseminations in altered microgranite of the Eocene Shirmazd intrusion. The mineralized microgranite has initial $^{87}Sr/^{86}Sr$ around 0.705 and positive ε_{Nd} of 1.7 to 2.0, i.e. displays more mantle input than the other intrusive rocks. (3) The polymetallic (Sn-Au-Cu) Deh Hossein prospect is characterized by quartz-sulfide veins and their gossans in Jurassic meta-sedimentary rocks. Gold, cassiterite and a variety of sulfide minerals occur in quartz veins and disseminated in the meta-sedimentary host rock. The sulfide assemblage of chalcopyrite-arsenopyrite-pyrite-pyrrhotite defines a relatively low oxidation state of the hydrothermal system.

Hydrothermal alteration is not pervasive and, apart from strong tourmalinization at Nezam Abad, is characterized by weak sericitization, chloritization, silicification and minor carbonatization. Overall, the sulfide content is low. Gold occurs as free visible Au in quartz and in alluvial deposits, as well as invisible in arsenopyrite. Bismuth minerals, including, bismuthinite, native bismuth and Bi-Te-Pb-S phases in arsenopyrite, are common.

Sulfur isotope data on arsenopyrite (-0.7‰ $\delta^{34}S$) and chalcopyrite (0.4‰ $\delta^{34}S$) support an igneous sulfur origin for the Astaneh system. The $\delta^{18}O$ values of hydrothermal quartz from Nezam Abad (11.9 to 13.6‰), Astaneh (11.5 to 13.3‰) and Deh Hossein (15.5 to 19.4‰) confirm the magmatic or magmatic-metamorphic origin of the hydrothermal fluids.

The mineral deposits studied have a geochemical Te-Au-Bi-As-Sb-Ag signature in common, are relatively low in base metals, low in oxidation state, and are associated with granitic intrusions of relatively reduced nature (ilmenite series). These are features typical of intrusion-related gold systems. The Nezam Abad and the Astaneh systems are intrusion-hosted, while the Deh Hossein prospect is of proximal type.

The mineralization in the study area is derived from Eocene collisional magmatism during the Alpine orogeny and interaction of magmatic fluids with metamorphic country rocks, and represents an intrusion-related Au mineralization style in the Sanandaj-Sirjan magmato-metamorphic belt.

.

Chapter 1

1. **Introduction**

1.1 **General**

Iran is a rich country in terms of natural resources. Since at least the first millennium BC, metals were explored, mined and metalurgically extracted. The study area, i.e. Astaneh-Nezam Abad is situated in the northern part of the Sanandaj-Sirjan metamorphic-magmatic belt, west-central Iran. This area has long been recognized for Au and W mineralization of hydrothermal origin, but recent exploration of the historical Deh Hossein Sn-Au-Cu prospect with important archeometallurgical aspects, has increased the importance of this area for more detailed studies in order to present a genetic model for finding other similar deposits in Iran. This area covers the Shazand quadrangle (49^{o}00´-49^{o}30´ N, 33^{o}15´-34^{o}00´) with a surface area of about 1100 km^{2}, of which the main intrusions together with three ore deposits/prospects, including Nezam Abad, Astaneh and Deh Hossein were examined in detail.

1.2 **Objectives**

The main objectives of this research are:

- Petrographical and petrological studies of the main intrusions.
- Study of the mineralization, in terms of ore mineralogy, paragenetic sequence, thermometry, alteration and host lithology.
- Presentation of a metallogenetic model.

1.3 **Methodology**

This research is based on field and laboratory studies. Field studies consist of reconnaissance and semi-detailed exploration work including sampling and were carried out through cooperation between the Mine Exploration, Remote Sensing and Geochemistry departments of the Geological Survey of Iran. About 100 bulk rock samples were analyzed by Instrumental Neutron Activation Analysis and Inductively Coupled Plasma Emission methods at Actlabs, Canada, X-Ray Fluorescence Spectrometry at Bundesanstalt für Geowissenschaften und Rohstoffe, Hannover. Electron microprobe and conventional ore microscopy methods were carried out at Institute of Mineralogy and Mineral Resources of the Technical University of Clausthal, Germany. Isotope analysis including (Rb-Sr and Sm-Nd) was performed at Vsegei, St Petersburg, Russia. Stable S and O isotope analyses were done at Münster and Göttingen University, respectively.

1.4 **Regional geology**

The NW-SE trending Zagros orogen system in the W-SW part of the country comprises three parallel belts, including from souhwest to northeast the Zagros fold belt (Stöcklin 1968, Mohajjel et al. 2003), the Sanandaj-Sirjan metamorphic belt (Mohajjel and Ferguson 2000, Mohajjel et al. 2003, Agard et al. 2005) and the Urumieh-Dokhtar magmatic arc (Berberian and Berberian 1981, Mohajjel et al. 2003) (Figs. 1.1, 1.2). The formation of the Sanandaj-Sirjan zone has been ascribed to the generation of the Tethys ocean and its subsequent destruction during Cretaceous and Tertiary convergence and continental crust between the Afro-Arabian and the Eurasian plates (Mohajjel et al. 2003, Agard et al. 2005, Ghasemi and Talbot 2006).

Most authors, including Stöcklin (1968), Berberian and King (1981), Davoudzadeh and Weber-Diefenbach (1987), Hooper et al. (1994), Mohajjel et al. (2003), Agard et al. (2005), correlate the predominantly Mesozoic and Tertiary marine and continental sedimentary sequences of this zone with those of the Central Iranian Block in the east, while Alavi (1994) favors an Arabian affinity. Late Jurassic to Tertiary Alpine compressive tectonic events are characterized in this tectonic zone by norhwest-oriented parallel belts of sedimentary and metamorphic rocks, partly overturned northwest-trending folds to the south and southwest, southwest-verging thrusts, and northwest-trending high-angle reverse faults, which resulted in thickening of the crust and Tertiary uplift of the Sanandaj-Sirjan zone (Stöcklin 1968, Berberian and King 1981, Mohajjel and Ferguson 2000, Mohajjel et al. 2003, Agard et al. 2005, Ghasemi and Talbot 2006).

Late Jurassic to Eocene calc-alkaline magmatism of the Sanandaj-Sirjan with climax during Late Cretaceous is attributed to northeastward subduction underneath Central Iran (Förster 1974, Berberian and Berberian 1981, Berberian and King 1981, Berberian et al. 1982, Agard et al. 2005, Ghasemi and Talbot 2006). Older magmatic activity in the Sanandaj-Sirjan zone, which consists of Late Triassic and Early Jurassic tholeiitic mafic volcanic rocks (Alavi and Mahdavi 1994), is interpreted as remnants of Tethyan oceanic crust (Mohajjel et al. 2003) and Late Proterozoic to early Paleozoic mafic rocks formed during extensional events (Berberian and King 1981).

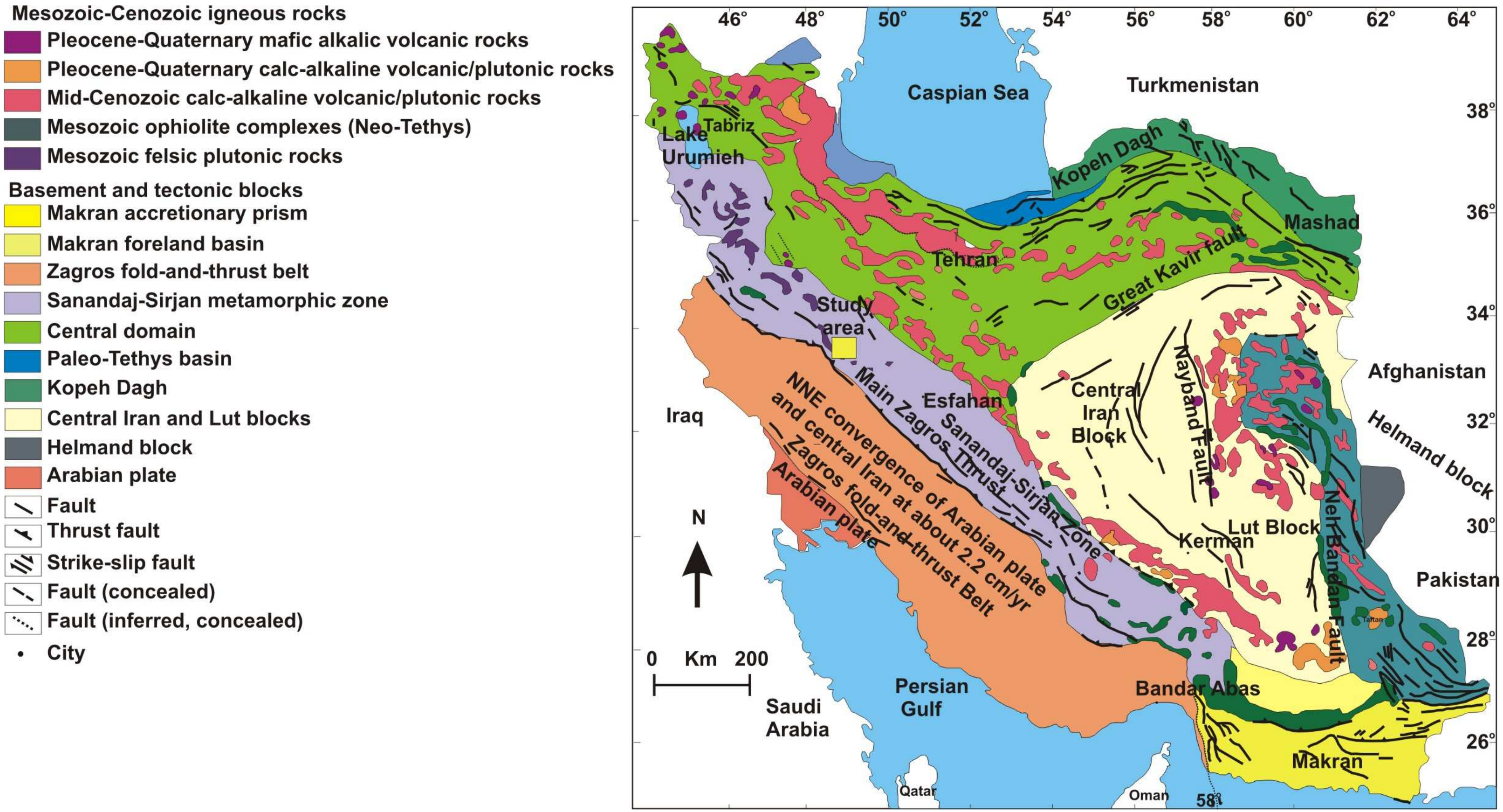

Fig. 1.1: Geology of Iran, illustrating the main tectonic units together with distribution of the Mesozoic-Cenozoic magmatism (modified from Richards et al. 2006).

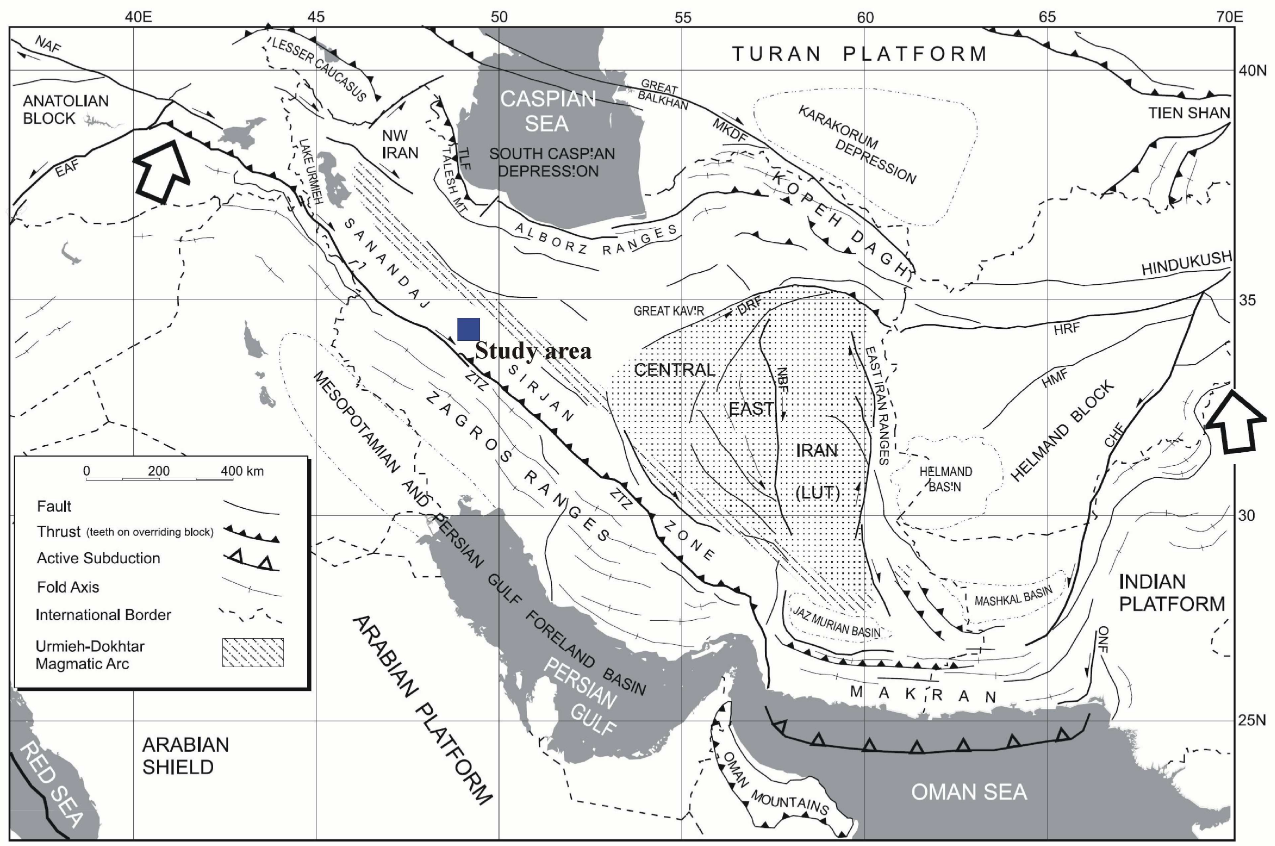

Fig. 1.2: Simplified structural map of Iran and adjacent regions, illustrating position of the study area (after Ramezani and Tucker 2003).

Mohajjel et al. (2003) divided the Sanandaj-Sirjan zone into an outer belt of imbricate thrust slices that includes the Zagros suture and an inner belt or complexly deformed subzone which hosts the study area. This subzone is characterized by abundant Triassic metamorphic rocks in the northwestern part, followed to northeast by a large region of the Late Triassic-Jurassic schist-phyllite-slate, so called Hamadan Phyllite (Mohajjel et al. 2003) (Fig. 1.3). Recent investigations have revealed that a majority of these rocks are metamorphosed equivalents of partly fossiliferous Paleozoic and Mesozoic units (Davoudzadeh et al. 1986, Davoudzadeha and Weber-Diefenbach 1987, Mohajjel et al. 2003, Baharifar et al. 2004). Thus, contrary to some reports of Hercynian (eg. Thieleh et al. 1968, Berberian and Berberian 1981) or older orogenic events, much of the deformation, metamorphism and magmatic events in the Sanandaj-Sirjan zone are related to the closure of the Tethys ocean (Mohajjel et al. 2003).

1.5 **Economic geology**

The Urumieh-Dokhtar magmatic arc hosts porphyry copper and skarn ore deposits (Waterman and Hamilton 1975, Hezarkhani and Williams-Jones 1998, Karimzadeh Somarin and Moayyed 2002) which formed in a typical subduction context (Förster 1974, 1978). The

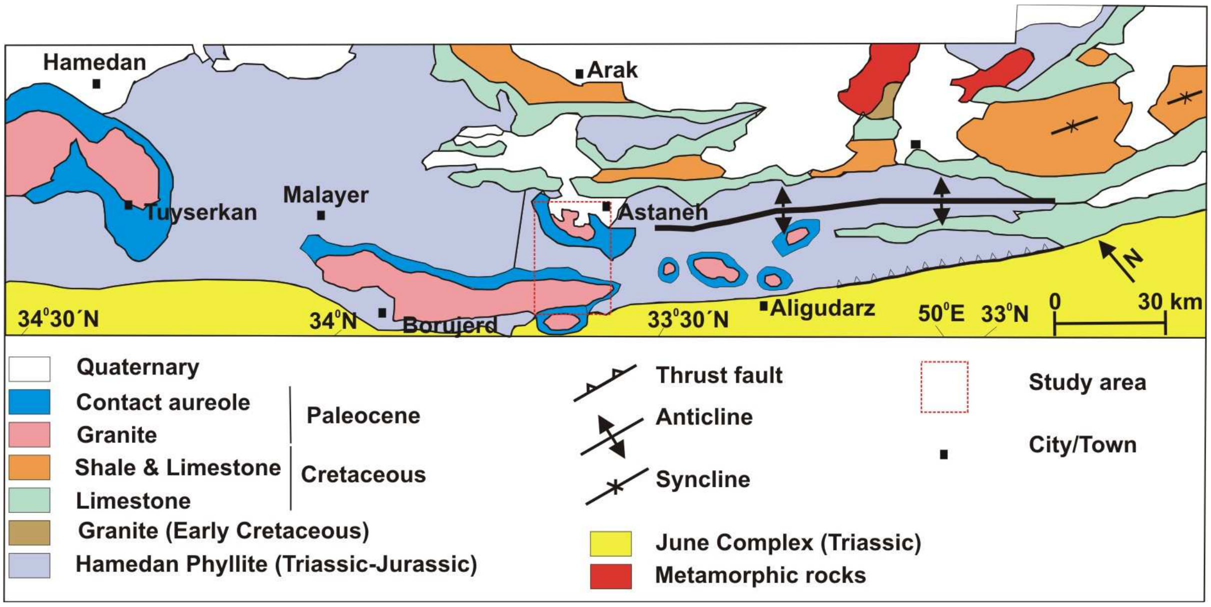

Fig. 1.3: Generalized geological map of southwestern complexly deformed sub-zone, showing the distribution of the Hamadan Phyllite and overlying Cretaceous successions and Paleozoic granite intrusions as well as study area (modified from Mohajjel et al. 2003).

ore deposits of the adjacent Sanandaj-Sirjan zone and their geodynamic setting have been studied to a lesser extent and available data are unsatisfactory. This is due to a complex protracted Late Precambrian to Tertiary evolution, accompanied by multiple deformation events and local greenschist to amphibolite facies metamorphism (Moritz et al. 2006).

This thesis is aimed at improving the knowledge on the metallogeny of the Sanandaj-Sirjan tectonic zone and is based on field and analytical data, gathered on three ore deposits/prospects including the Nezam Abad W-(Sn-Au) ore deposit (chapter three), the Astaneh Au prospect (chapter 4) and the recently explored Deh Hossein Sn-Au-Cu prospect (chapter 5). At the end, a metallogenic model is presented for the entire area (chapter 6).

1.6 **Geology of the Shazand quadrangle**

The study area is located in the northeastern edge of the Zagros belt and southwest of the Urumieh-Dokhtar volcanic arc, i.e. at the west of the active Central Iran microcontinent (Figs. 1.2, 1.3). The geology of the study area is illustrated in Figure 1.4. The lithostratigraphical units are as follows:

- Permian: Volcano-sedimentary rocks, chert-bearing limestone and dolomite. Metamorphosed sandstone and quartzite occur mostly in lower parts. Fusullinid-bearing limestone in the lower parts and Pentacrinus-bearing limestone in the upper parts of this unit, have been ascribed to Permian and Permian-Triassic, respectively.

- Jurassic: The Jurassic series covers a large area of low topography which contains several hundreds km^2 of low-grade metamorphic rocks which are mainly dark shale and sandstone with meta-sandstone and meta-volcanic interbeddings.

The general character of the Jurassic rocks is uniform over the entire area: black-grey to dark greenish-grey shales and phyllites (weathering to a greenish-brown color). The metamorphic grade is low, except in the contact aureoles of intrusive rocks.

Fossils are rather rare and there has been considerable debate on the age of the phyllites. In some places they are followed by Orbitolina limestone (outside the study area), hence Bellon and Braud (1975) proposed a Jurassic age. Thiele et al. (1968) believed that some of the metamorphic rocks were older than Jurassic, whereas Bellon and Braud (1975) stated that all of these low grade metamorphic rocks are Jurassic, with regional metamorphism during the Late Kimmerian.

- Cretaceous: In the northeast of the area, Cretaceous sedimentary rocks appear forming mountain ranges. Near the base, sandy dolomite and sandy limestone overlie Orbitolina limestone, but in the upper part marlstone and shales are dominant. Radfar (1987) proposed the following sequence for the Cretaceous rocks of the region from bottom to top:

a) Conglomeratic and sandy horizon with 10-15 m thickness. This horizon contains mostly pebbles of Hamedan pelitic schists with different schistosity in comparison with Cretaceous conglomerate, indicating a termodynamic metamorphic phase before transgression of the Cretaceous basin.

b) Volcanic unit including andesite and tuff with about 6-7 m thickness.

c) Dolomitic sandstone, sandy dolomite, sandy limestone and argillic limestone. Paleontological studies confirm an Aptian age.

e) Orbitolina limestone with Aptian-Albian and Albian-Cenomanian ages in the lower and upper parts, respectively.

f) The Uppermost part includes marl and shale with interbedded Cenomanian Orbitolina limestone.

The main intrusions of the study area will be discussed in the chapter 2.

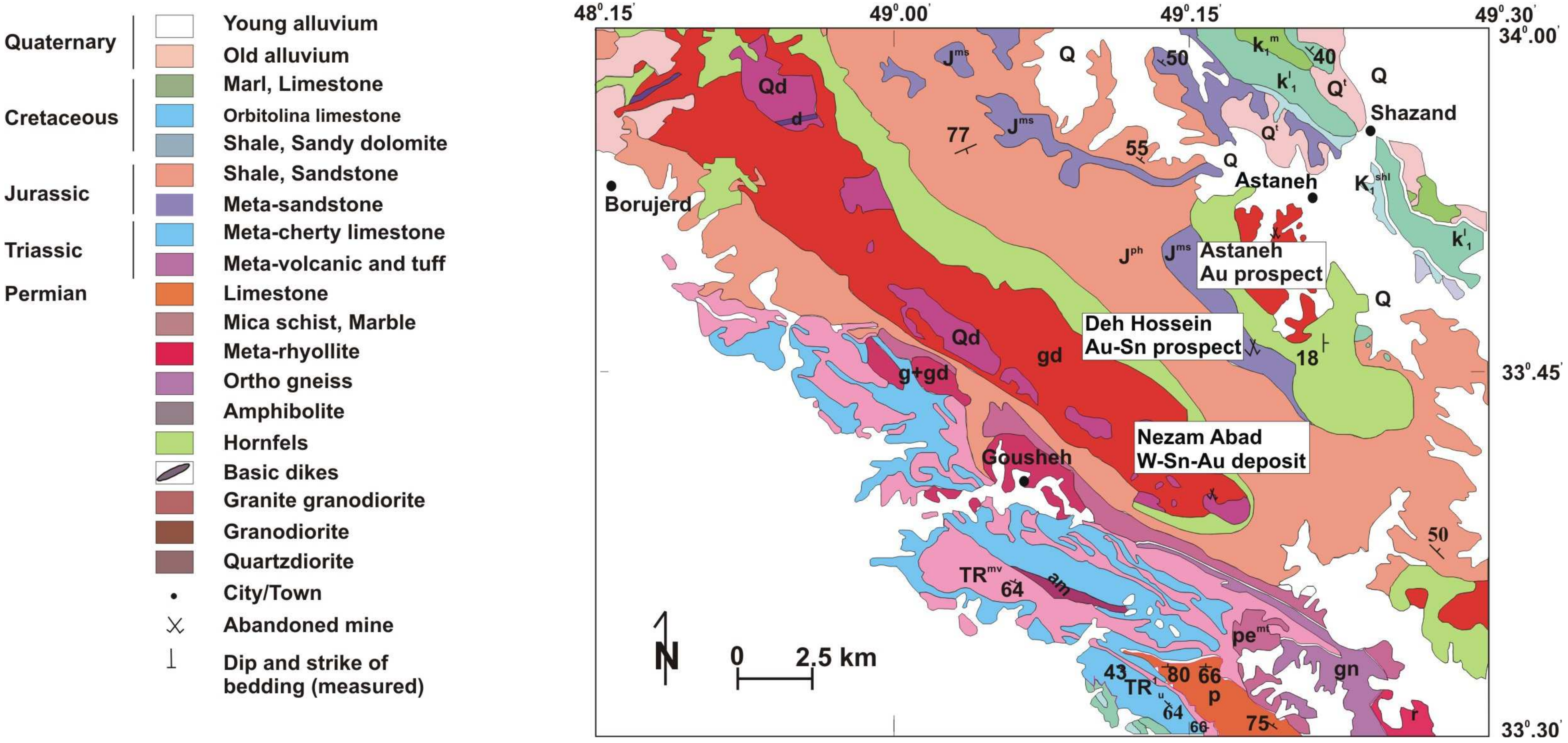

Fig. 1.4: Simplified geological map of the 1: 250,000 Khorram-Abad quadrangle, illustrating geology of the Shazand area (modified from Sahandi et al. 1992).

Chapter 2

2. **Magmatism**

2.1 **Petrography**

Granitic intrusions are ubiquitous in the area and the four most important are: a) Astaneh, a circular intrusion SSW of the city of Shazand, b) Nezam Abad-Malmir complex, the biggest intrusion in the area with an elongate shape, c) Gousheh, separate outcrops of granitic rocks exposed in the area of Gousheh (Fig. 1.4) and d) Shirmazd Mountain, a dome like stock, intruding the Astaneh intrusion (chapter 4).

2.1.1 **Astaneh intrusion**

This intrusion with a surface area of about 30 km^2 is located SSW of the city of Shazand. It has intruded Jurassic schists, giving rise to typical contact metamorphism.

The intrusion appears relatively homogeneous at outcrop scale, although microscopic studies show that it includes biotite granite and granodiorite. The granite is mainly exposed in the northern part, while on the eastern side of the intrusion, granodiorite is more common. The intrusion is intersected by abundant aplite dikes and quartz veins.

Field evidence and microscopic studies show that most of the Astaneh intrusion is made up of granodiorite. The texture is dominantly medium to coarse-grained equigranular, partly porphyritic. The mineralogy of the studied rocks comprises plagioclase (25-30 vol %), orthoclase, microcline, perthite (20-25 vol %), quartz (20-30 vol %), biotite (10-15 vol %), amphibole (5 vol %), muscovite and andalusite (< 1 vol %) and accessory zircon and apatite. Xenoliths are abundant, especially near the eastern margin. Two main xenolite groups have been identified, including quartzdiorite and metamorphic rocks. The first one occurs mainly near the southeastern margin and its mineralogy is amphibole, biotite and plagioclase with a small amount of quartz. Both feldspar and biotite are partially altered. The texture is fine to medium-grained equigranular. Metamorphic xenoliths are present in the Shirmazd valley, west of Astaneh, which consists of pelitic and hornfelsic rocks. Fig 2.1 shows some microscopic photos and Table 2.1 represents a petrographical summary of some of samples studied.

2.1.2 **Nezam Abad-Malmir complex**

This intrusion with a surface area of about 200 km^2 runs parallel to the Zagros Mountains with northwest-southeast trend (Fig. 1.4). The intrusion of this complex into the Jurassic schist and phyllite has led to the formation of typical contact metamorphism, manifested by sillimanite,

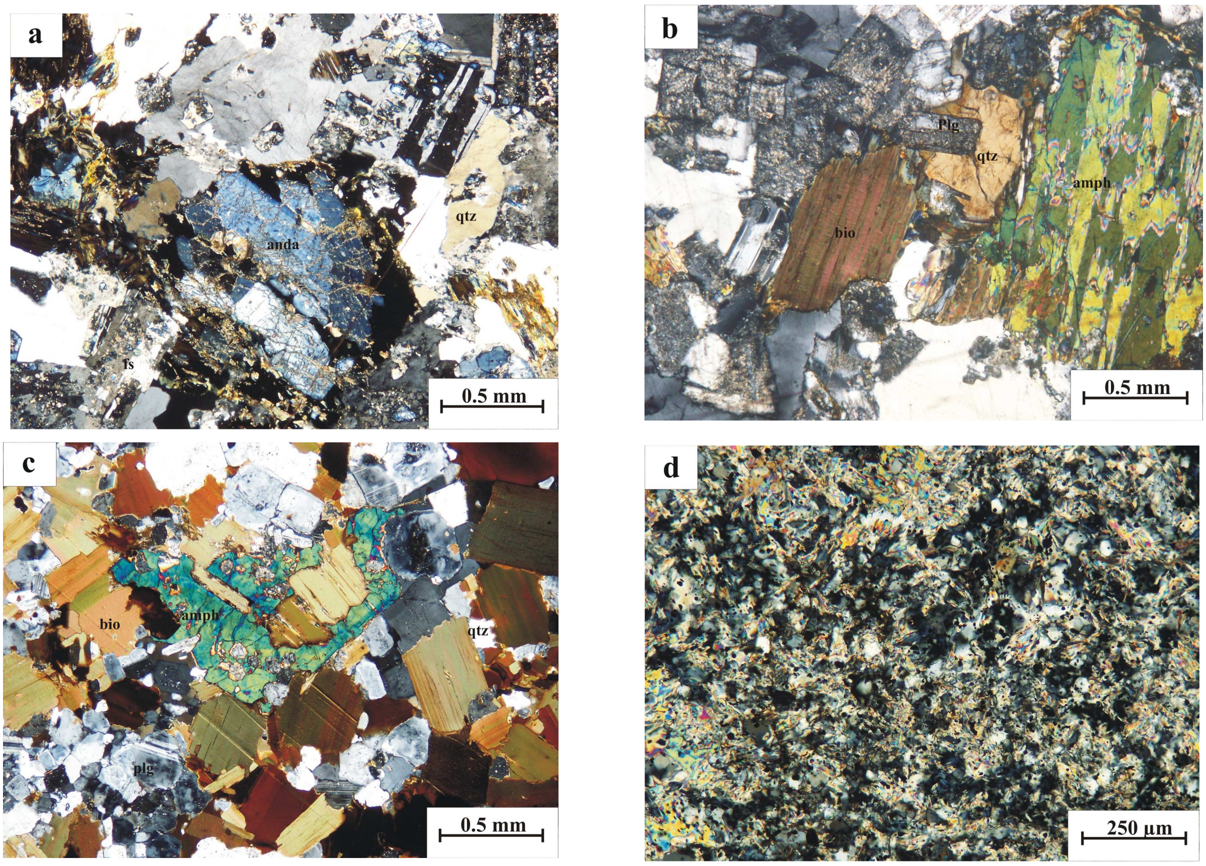

Fig. 2.1: Microphotographs of the Astaneh samples, XPL. a & b Astaneh granodiorite. c quartzdioritic xenolith. d Hornfels with fine-grained equigranular texture.

cordierite and andalusite-bearing hornfels. It was considered formerly to have formed during one phase of intrusive activity (e.g. Radfar 1987). Recent geochronological measurements (e.g. Masoudi 1997), showed that the complex has formed during two main periods. The composition of the complex is mainly granodiorite, partly quartzdiorite and tonalite (Fig. 2.2, Table. 2.2).

2.1.2.1 **Granodiorite**

Most part of the complex is made up of granodiorite. The mineralogy of the granodioritic rocks includes plagioclase (45-50 vol %), orthoclase, microcline and perthite (10-12 vol %), quartz (about 25 vol %), biotite (about 15 vol %), amphibole (about 5 vol %). Accessory minerals are apatite, zircon and tourmaline. The texture is commonly equigranular.

2.1.2.2 **Quartzdiorite-tonalite**

Younger parts of the complex are distinguished by a varied series of minor intrusions, ranging from quartzdiorite to tonalite. These rocks are widely scattered as small intrusions through the southern part of the complex and are related to tungsten mineralization. The mineralogy of these rocks consists of plagioclase (40-50 vol %), biotite (about 20 vol %), quartz (about 10 vol %), hornblende (5-10 vol %), orthoclase, perthite (about 5 vol %), sphene (< 1 vol %). Apatite, zircon and tourmaline occur very rarely.

Table. 2.1: Petrographical summary of representative samples of the Astaneh intrusion.

Sample		Mineralogy		Alteration(s)	Texture	Rock type
	Main	Accessory	Secondary			
AS-9	plg, qtz, fs bio, amph	rt, ap, zr	chl, ser clay, ep	chloritization sericitization carbonatization	granular	granodiorite
AS-10	plg, qtz, bio amph, fs and minor ms	rt, zr, ap	chl, ser clay, ep	chloritization sericitization	granular	granodiorite
AS-16	plg, fs, qtz bio	rt, ap, zr	chl, ser, ep clay	chloritization sericitization	granular	granodiorite
AS-27	qtz, plag, fs bio, minor anda	rt, ap	chl, ser, ep clay	chloritization sericitization	granular	granite
AS-28	plg, qtz, fs, bio amph	rt, ap, zr	chl	chloritization	granular	quartzdioritic xenolith
AS-38	plg, qtz, fs minor bio	rt, zr, ttn	chl, ser clay, ep	sericitization carbonatization chloritization	porphyritic phenocryst: plg, bio, qtz groundmass: qtz, plg	granodiorite
AS-44	plg, fs, qtz amph, bio	rt, ap, ttn	chl, ep, ser	chloritization	microgranular to granular	quartzdioritic xenolith
AS-48	plg, qtz, fs, bio minor amph	rt, ap, ttn	chl, ser	chloritization sericitization	granular	granodiorite
AS-55	qz, ms, chl	-------	-------	-------	microgranular	hornfels
AS-66	plg, qtz, bio amph, anda	ttn, tour rt, ap	chl, ser, ep	chloritization sericitization	equigranular	granite

2.1.2.3 **Pegmatite**

Pegmatites are abundant in the central and northwestern part of the complex. Studies by Radfar (1987) and Masoudi (1994) indicate that these pegmatites are barren and have a simple mineralogy. Radfar (1987) identified the following mineral assemblages: quartz-tourmaline, quartz-feldspar-muscovite, sodic and potassic feldspar-quartz-chlorite-muscovite-tourmaline-garnet. The petrogenesis of the pegmatites has been discussed in detail by Masoudi (1997).

2.1.2.4 **Aplite**

Most aplites are in the quartzdioritic parts of the complex, where the amount of biotite is high. The thickness of aplitic veins varies between 50 cm to 1 m. Their mineralogy is generally quartz, orthoclase-microcline, plagioclase, biotite, and tourmaline as accessory mineral. Secondary minerals are mainly epidote, sericite, chlorite and clay minerals.

2.1.3 **Gousheh intrusion**

This intrusion with a surface of about 40-45 km^2 is located in the area Gousheh-Tavandasht and has intruded metamorphosed Permo-Triassic limestone, dolomite, dolomitic limestone and lavas, giving rise to contact metamorphism with formation of marble and hornfels. The composition is mainly granite, changing partly to granodiorite (Table 2.2 & Fig. 2.3). The mineralogy of the studied rocks comprises quartz (about 20 vol %), plagioclase (about 40 vol %), orthoclase, perthite (about 25 vol %), biotite (about 5 vol %), apatite, zircon and epidote (< 1vol %).

2.1.4 **Shirmazd Mountain**

The Shirmazd Mountain consists of altered and mineralized microgranitic rocks. This Mountain has a dome shape with a radius of 400-600 m and 2450 m height and intrudes the Astaneh intrusion. In hand specimen, altered and mineralized rocks of the Shirmazd Mountain are pinkish to reddish in color with fine-grained microgranular and locally porphyry texture. The main minerals are quartz, feldspar, plagioclase and to a lesser extent biotite. Amphibole occurs very rarely. Feldspar and plagioclase are altered to sericite and clay minerals, while biotites have been altered to chlorite (Table 2.3 & Fig. 2.4). Abundant silica and aplitic veins cut the micrognanitic rocks of the Shirmazd Mountain. Isotope age determination by Rb-Sr method on whole rock has yielded 35.05 ± 0.92 Ma age for the microgranites of the Shirmazd Mountain (Nezafati et al. 2005).

2.2 **Geochemistry**

Geochemical data were used to define different lithologies, characterize magma types and identify the original tectonic setting of the rocks. Some representative samples were analyzed by X-ray fluorescence (XRF), neutron activation (INAA), and inductively coupled plasma emission spectroscopy (ICP) methods. These samples encompass the four main intrusive bodies of the region including the Astaneh, the Nezam Abad, the Goushe intrusions and the Shirmazd Mountain (Appendix 1).

2.2.1 **Rock classification**

Two methods including total alkali-silica (TAS) and Parameters R1 and R2 (De la Roche et al. 1980) were applied to classify the Shazand intrusions (Figs. 2.5 & 2.6).

2.2.2 **Petrogenesis**

In order to clarify possible relationships between different intrusions of the study area, variation diagrams such as Harker plots were applied for both major and trace elements. All diagrams were made against SiO_2 as the index of differentiation.

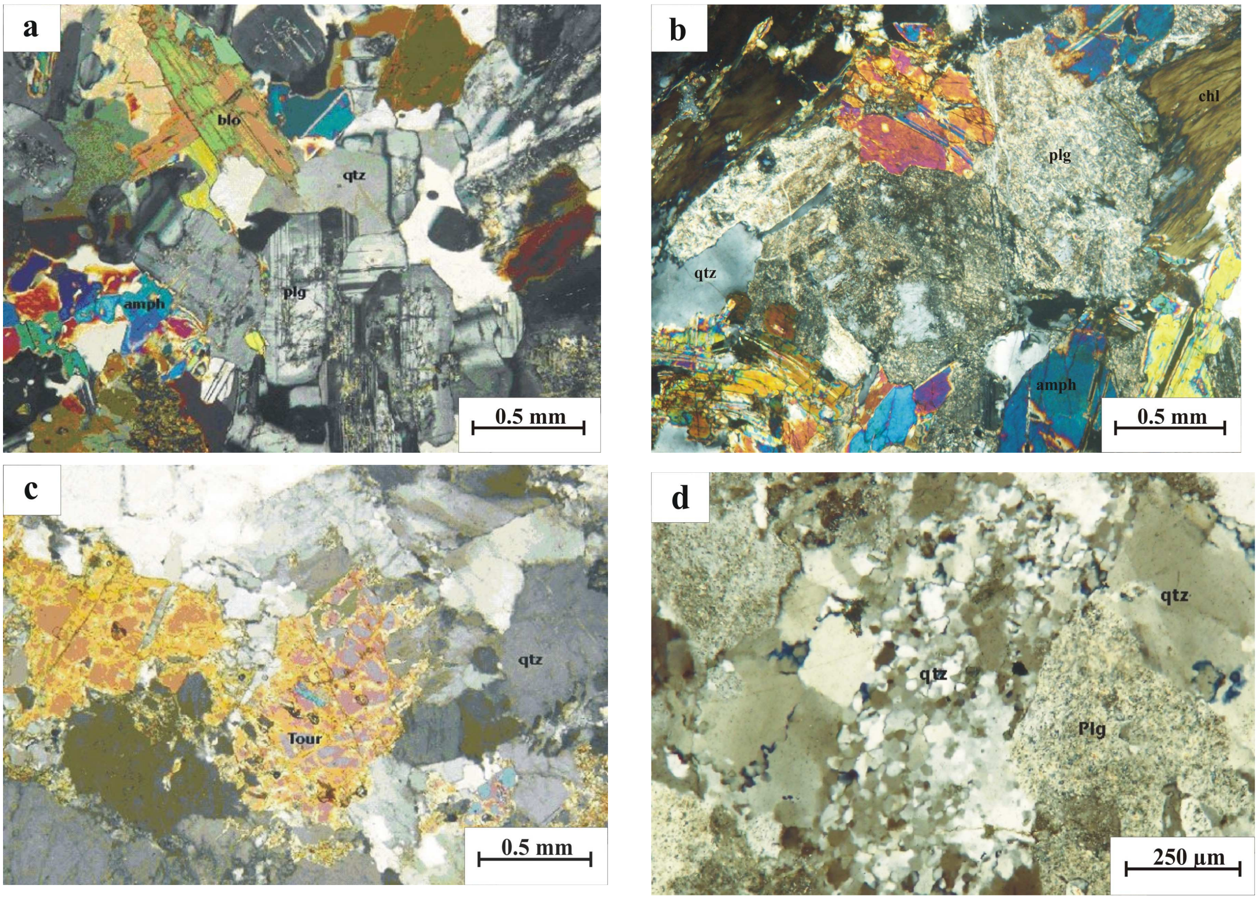

Fig. 2.2: Microphotographs of the Nezam-Abad samples, XPL.a Relatively fresh quartzdiorite with equigranular to porphyry texture. b Altered quartzdiorite. Plagioclase and biotite show sericitization and chloritization, respectively. c Aplite with quartz-tourmaline association. d Aplite with interstitial quartz.

Table. 2.2: Petrographical summary of representative samples of the Nezam Abad and Gousheh intrusions.

Sample	**Mineralogy**			**Alteration(s)**	**Texture**	**Rock Type**
	Main	**Accessory**	**Secondary**			
NZ-18	plg, qtz amph, bio minor, fs	rt, zr, tour	chl, ser, clay	chloritization sericitization	equigranular	quartzdiorite
NZ-22	plg, qtz amph, bio minor fs	rt, zr	chl, ser, clay	chloritization sericitization	equigranular	quartzdiorite
NZ-25	plg, qtz amph, bio minor fs	rt, zr	chl, ser, clay	chloritization sericitization	equigranular	quartzdiorite
NZ-60	plg, fs, bio amph	ap, zr, tour	-----	-----	equigranular	granodiorite
NZ-61	qtz, plg bio, ms anda, amph	ap	chl, clay	chloritization sericitization	equigranular	granodiorite
GO-5	qtz, plg	ap, zr	chl, ser, clay	chloritization	equigranular	granite

NZ: Nezam Abad, GO: Gousheh

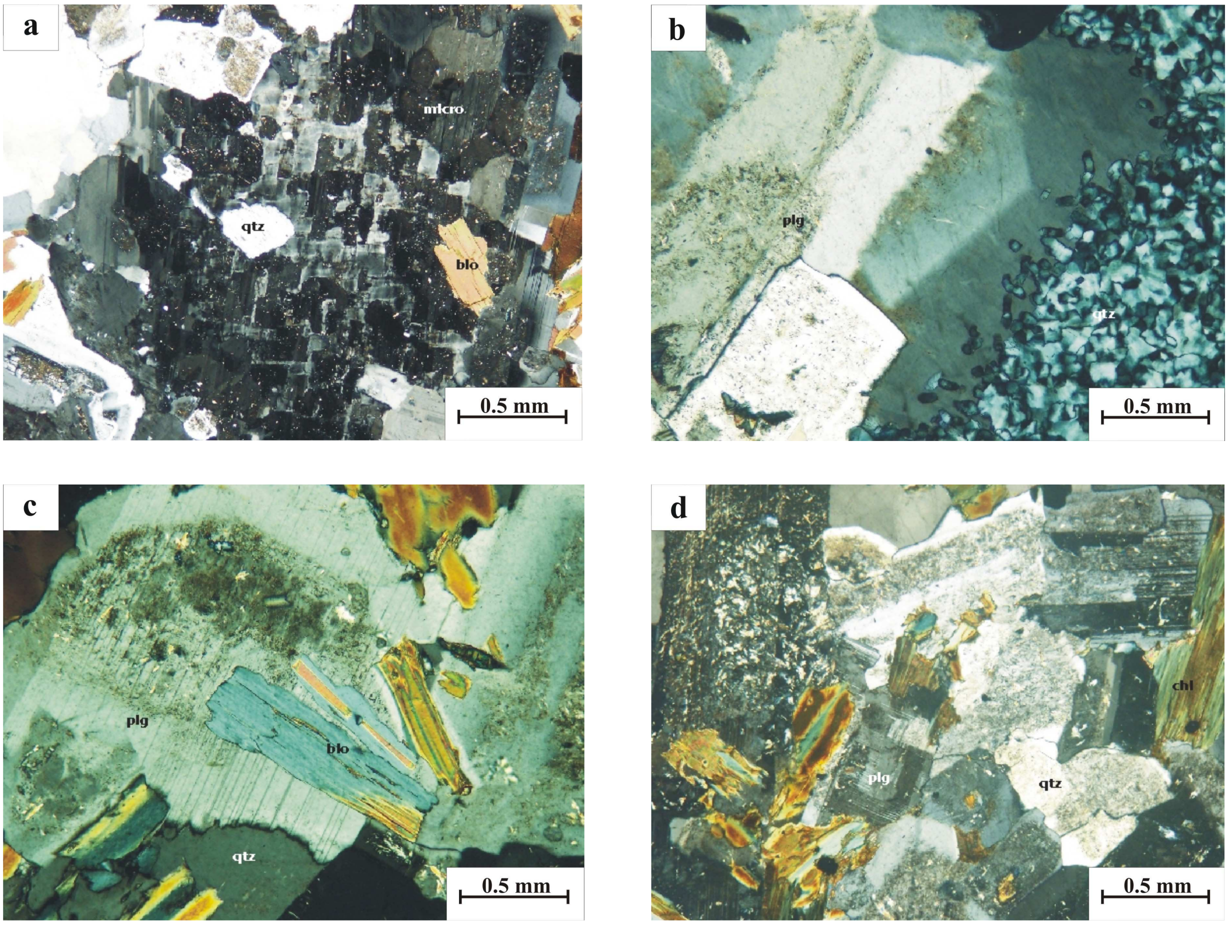

Fig. 2.3: Microphotographs of the Gousheh samples, XPL. a Association of microcline, quartz and biotite. b Plagioclase with late stage fine-grained quartz. c Alteration of biotite to chlorite. d Alteration of plagioclase to sericite

Table. 2.3. Petrographical summary of representative samples of the Shirmazd Mountain.

Sample		Mineralogy		Alteration(s)	Texture	Rock Type
	Main	Accessory	Secondary			
AS-31	qtz, fs, bio minor plg	rt, zr	ser, chl, clay	sericitization chloritization	microequigranular	microgranite
AS-32	qtz, fs, bio minor plg	rt, zr	ser, chl, clay	sericitization chloritization	microequigranular	microgranite
AS-64	qtz, fs, bio minor plg	rt, zr	ser, chl, clay	sericitization chloritization	porphyry	microgranite
AS-100	qtz, fs, bio minor plg	rt, zr	ser, chl, clay	sericitization chloritization	porphyry	microgranite

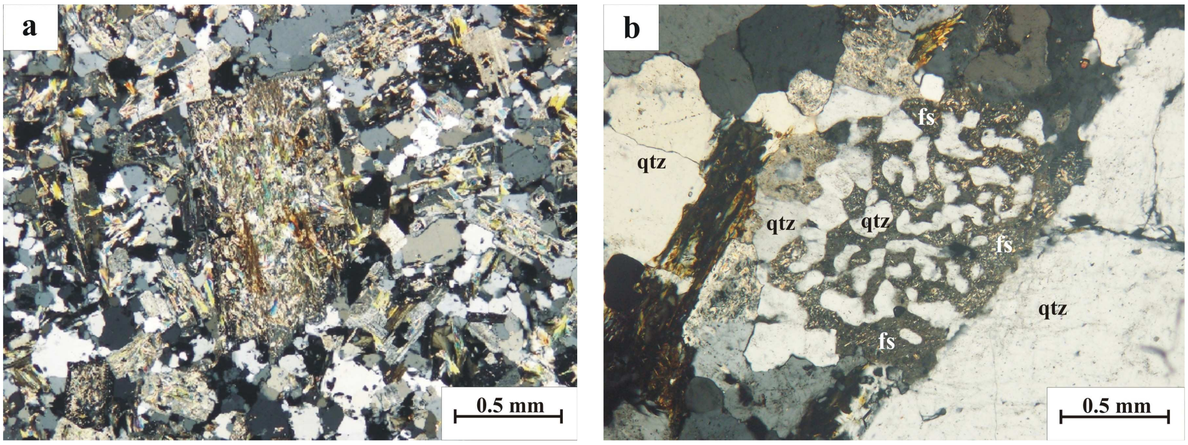

Fig. 2.4. Microphotographs of microgranites of the Shirmaz Mountain, XPL. a Strongly altered phenocryst of alkali feldspar in the quartz matrix. b Graphic texture in microgranite.

2.2.2.1 **Variation diagrams of major elements**

Major element data of the analyzed samples are shown in Figure 2.7. Although the rocks belong to different intrusive bodies with different ages, all samples lie essentially on a single trend with an SiO_2 range between 54 to 75 wt %, indicating that the rocks all followed a similar evolution trend. Only aplitic samples of the Nezam Abad intrusions show sometimes different behavior, likely due to weathering and alteration.

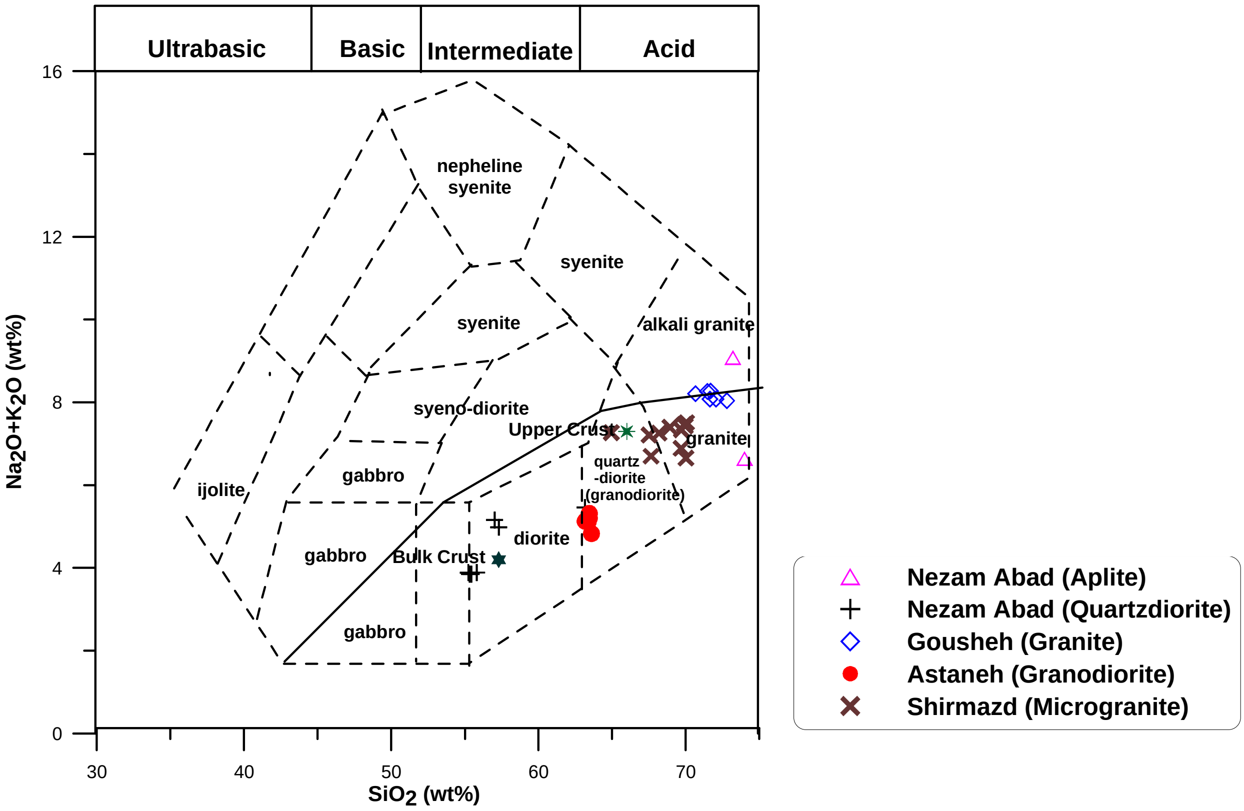

Fig. 2.5: The chemical classification and nomenclature of the representative samples of the Shazand granitoids using the total alkalis vs silica (TAS) diagram of Cox et al. (1979) adapted by Wilson (1989) for plutonic rocks.

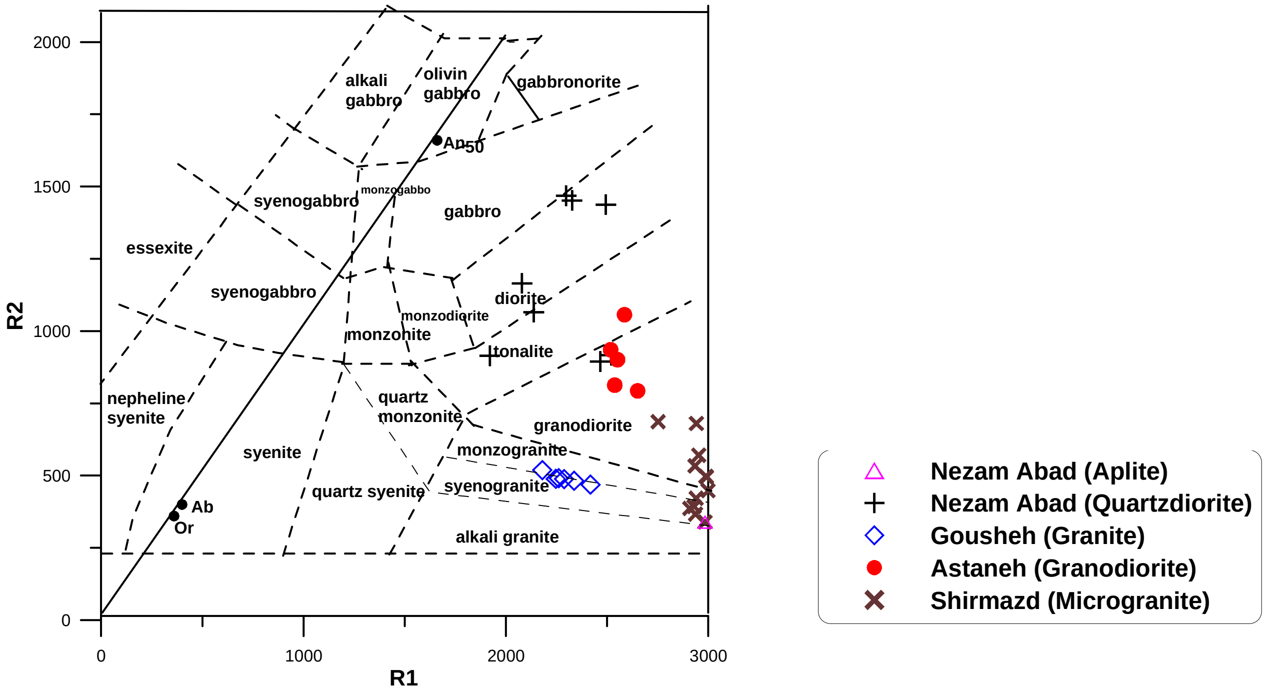

Fig. 2.6: Classification of the Shazand intrusive bodies using the parameters R1 and R2 (De la Roche et al., 1980), calculated from millication proportions. R1= 4Si-11(Na+K)-2(Fe+Ti) R2= 6Ca+2Mg+Al.

The major elements show a trend toward the aplite and more alkaline granites as the most fractionated members. The proportion of mafic phases, i.e. biotite decreases with increasing SiO_2 and mafic minerals are essentially absent or occur very rare in the aplites and more alkaline granites, reflecting very low levels of TiO_2, Fe_2O_3, MnO and MgO. Further crystallization of both apatite and the calcic component of plagioclase has led to correspondingly low levels of CaO and P_2O_5 at high SiO_2. The samples lie on a similar trend for major components such as K_2O and total Fe_2O_3, indicating that fractionation could be the main process in the chemical evolution of these plutonic rocks.

2.2.2.2 **Variation diagrams of trace elements**

Variation diagrams of trace elements are presented for the following groups:

1) **Low-field-strength (LFS) elements**

Low-field-strength elements or large ion lithophile elements (LILE) include Cs, Rb, K, and Ba. To these, may be added Sr, divalent Eu and Pb. Figure 2.8 depicts variation diagrams of LFS elements of the Shazand granitoids.

Data plotted for this group show moderate to good positive (Cs, Rb, Ba) and negative (Sr) elemental trends against SiO_2. As expected, the behavior of Rb and Sr reflects the K_2O and CaO trends, respectively (Fig. 2.8).

2) **High-field-strength (HFS) elements**

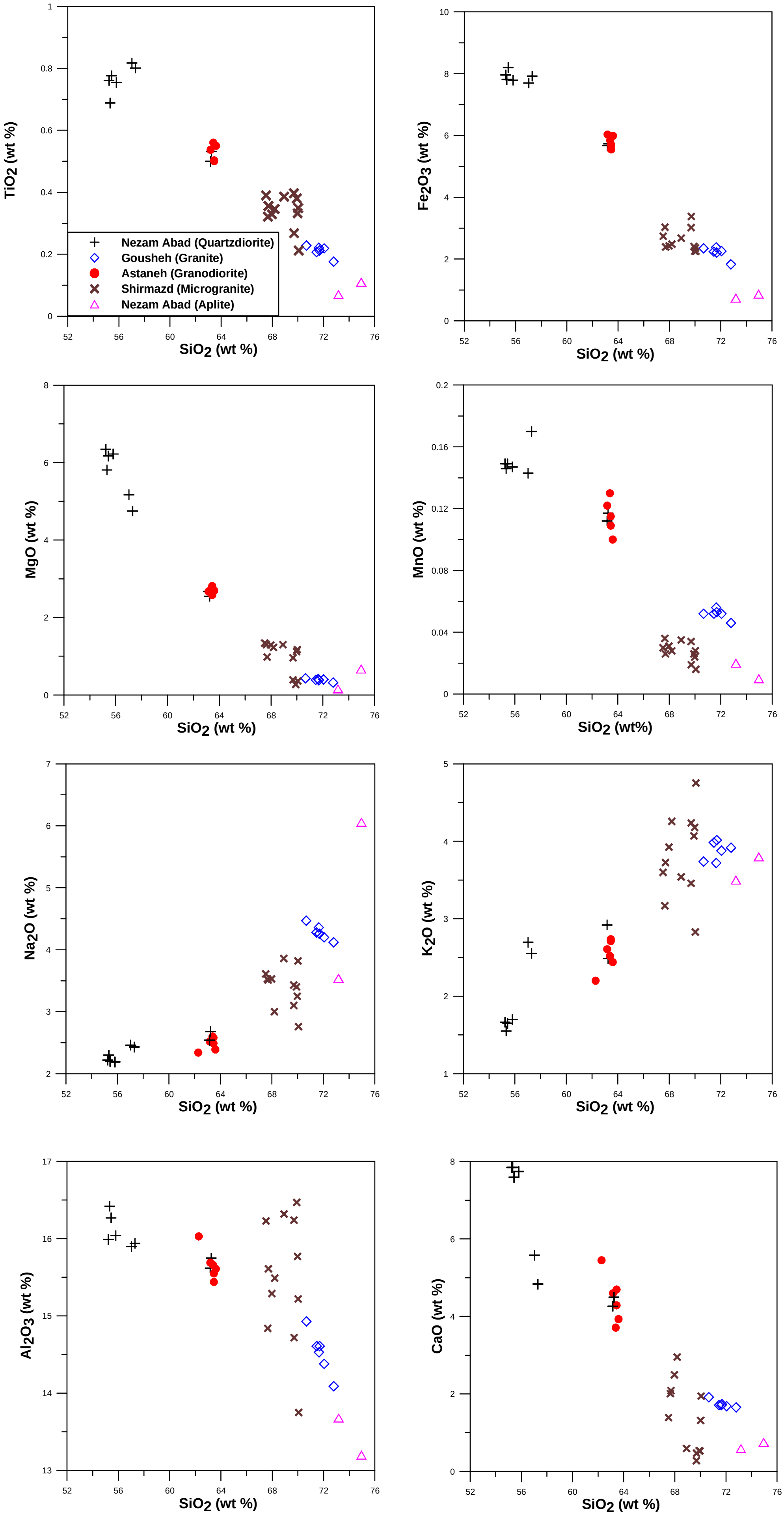

Fig. 2.7: Variation diagrams of major elements of the Shazand granitoids.

This group consists of trace elements with ionic potential > 0.2 such as Th, U, REE, Zr, Hf, Nb and Ta. Figure 2.9 shows their variation diagrams. Of these, Zr indicates weak positive correlation with SiO_2, while the other elements do not show clear correlation.

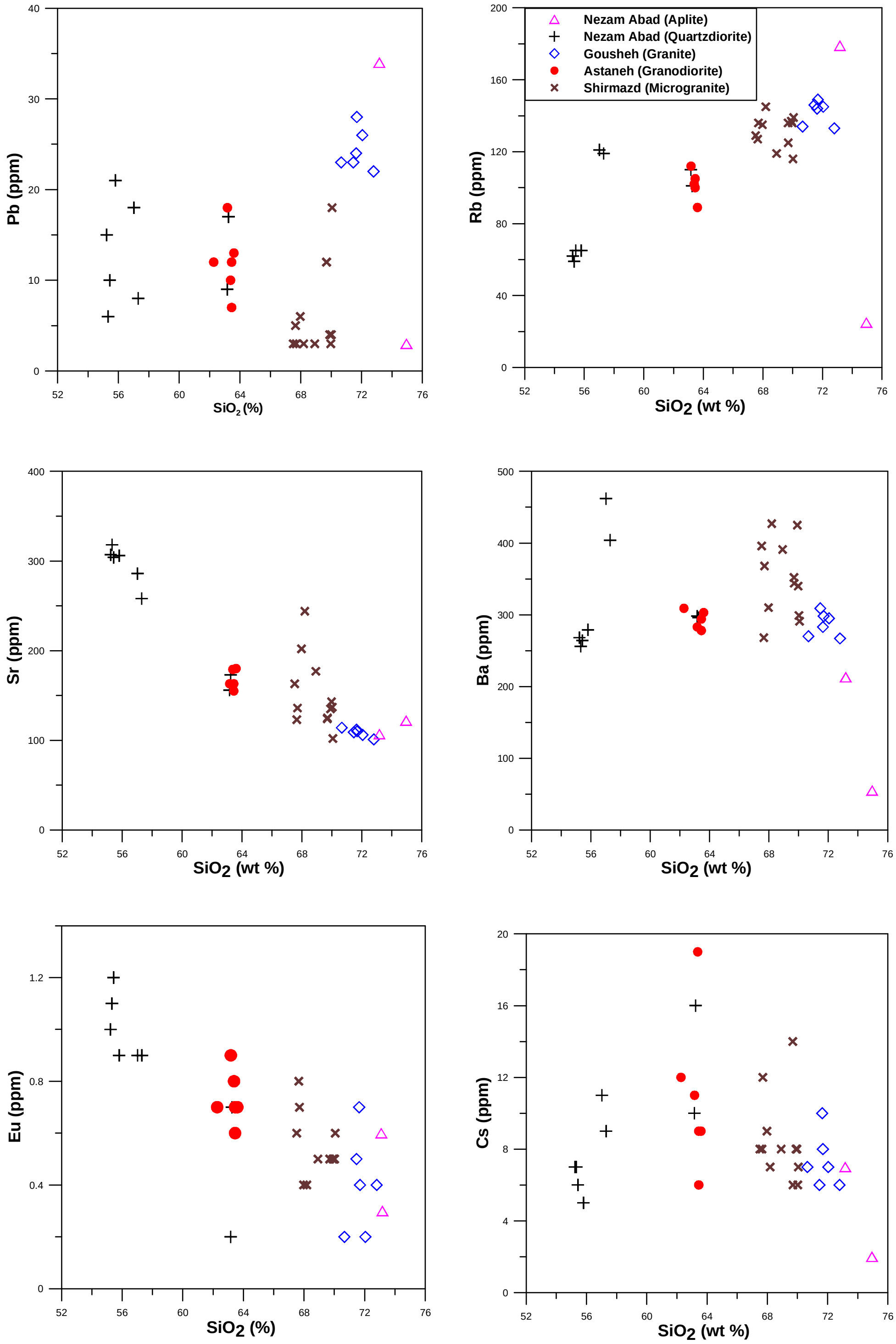

Fig. 2.8: Variation diagrams of low field strength elements of the Shazand granitoids.

3) Rare earth elements (REE’s)

This group comprises elements with atomic numbers 57 to 71. Eu and Ce are shown in Figure 2.8. Figure 2.9 illustrates variation diagrams of some of the other members of this group.

Aplites of Nezam Abad show lower level of rare earth elements, while the three main bodies represent no negative or positive correlation with SiO_2. Probably, concentrations of these elements are controlled by minor phases. Therefore, the data are scattered, being sensitive to small modal variation in apatite, allanite and monazite. In addition the Eu and Ce concentrations are near the detection limit of the analytical methods, and have a large error.

4) **Transition metal elements (TME's)**

Transition metals encompass elements with atomic numbers 21 to 30. Data of Sc, Cr, Co and Ni are presented in Figure 2.10. Clearly, the graphs show compatible behavior of these elements. These are fixed in phases such as biotite, generally entering the 4 and 6-fold coordination sites with Fe^{2+}, Fe^{3+}, Ti^{4+}, Mn^{2+} etc.

2.3 **Classification of magma series**

2.3.1 **Alkalinity**: The Shazand granitoids were classified according to the SiO_2 vs K_2O+Na_2O and AFM diagrams (Figs. 2.11, 2.12). These diagrams show that all the studied samples belong to subalkaline series and are calc-alkaline.

2.3.2 **Aluminosity**

The samples of the Astaneh and Gousheh intrusions are mostly peraluminous, while samples of the Nezam Abad complex and micrgranite of the Shirmazd Mountain are chiefly metaluminous and plot near the boundary of peraluminous and metaluminous (Fig. 2.13). Furthermore, this diagram shows that most of the samples are of I-type. More comments regarding I and S type will be given in the next sections.

2.4 **Tectonic setting**

In order to discriminate tectonic setting of the intrusive bodies, two discrimination diagrams were used (Figs. 2.14, 2.15). The studied samples show a volcanic-arc setting, a fact that correspond to the field evidence and other results.

2.5 **Spider diagrams**

Two ways of normalizing trace element data were applied for the data presentation in multielement plots, including chondritic meteorites and mid-oceanic ridge basalt (MORB) (Figs. 2.16, 2.17). Figure 2.16 shows, enrichment of all elements selected relative to chondrite, although there is a relative decrease from left to right, corresponding to increasing compatibility on partial melting. More mobile LIL elements (Rb, K, Ba, Sr) in all

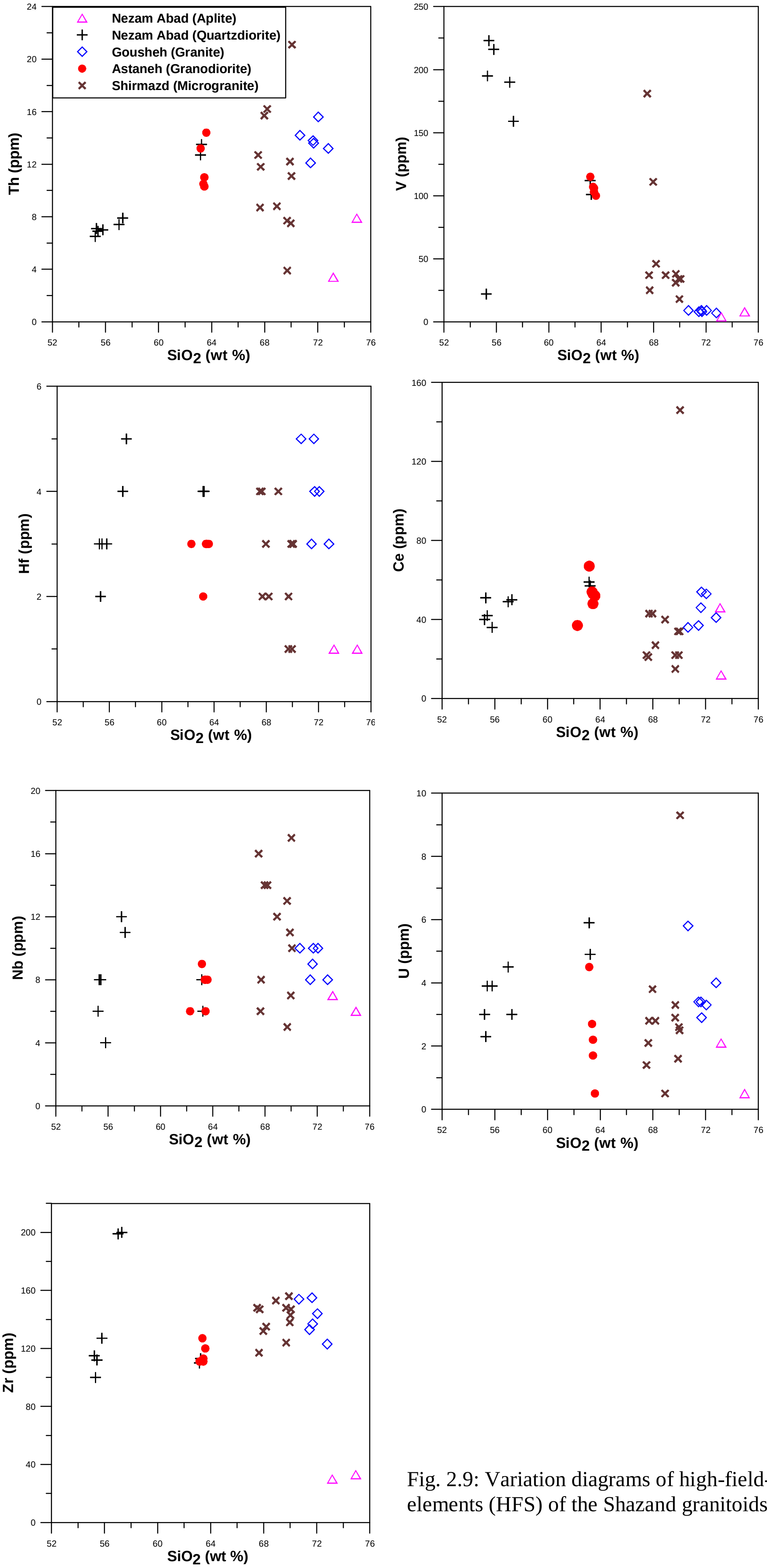

Fig. 2.9: Variation diagrams of high-field-strength elements (HFS) of the Shazand granitoids.

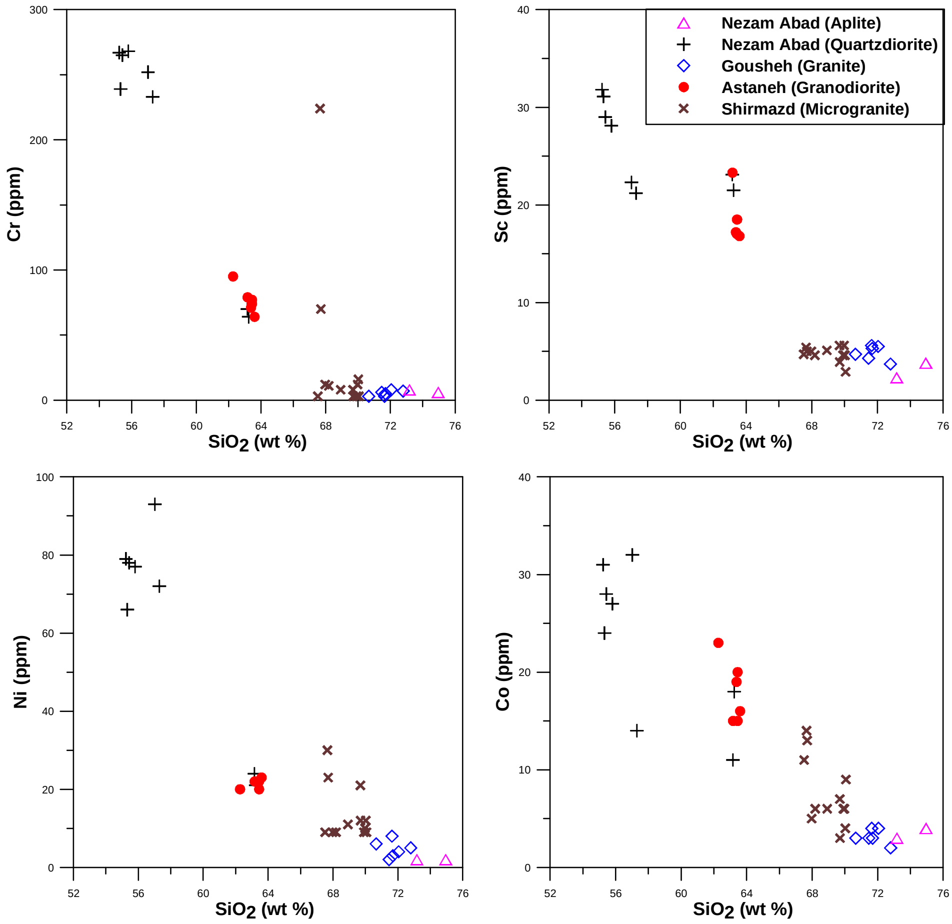

Fig. 2.10: Variation diagrams of transition metal elements of the Shazand granitoids.

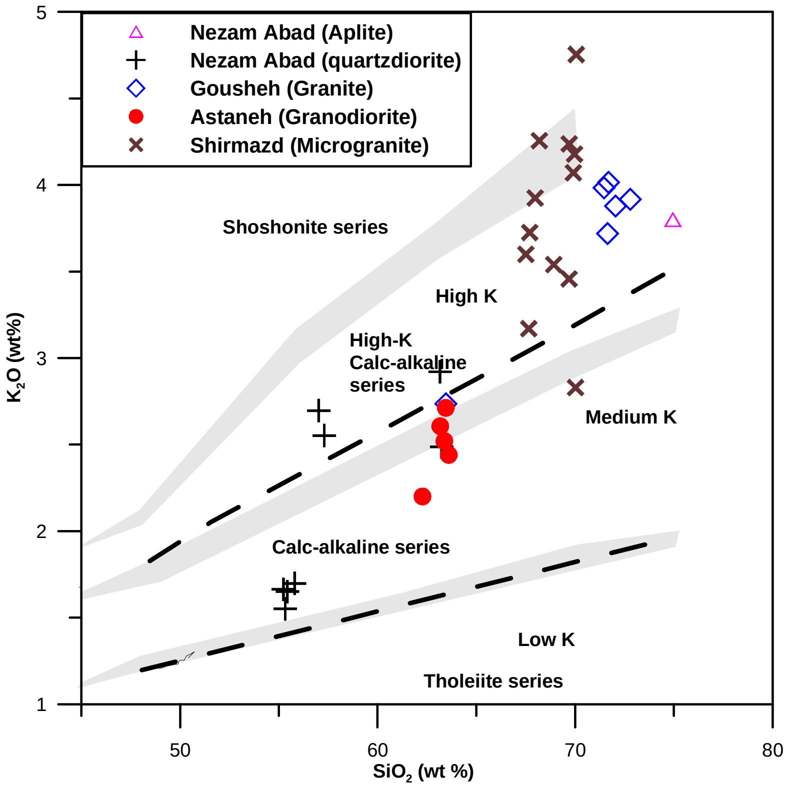

Fig. 2.11: SiO_2 vs K_2O plot of Shazand granitoids (Le Maitre et al. 1989) diagrams.

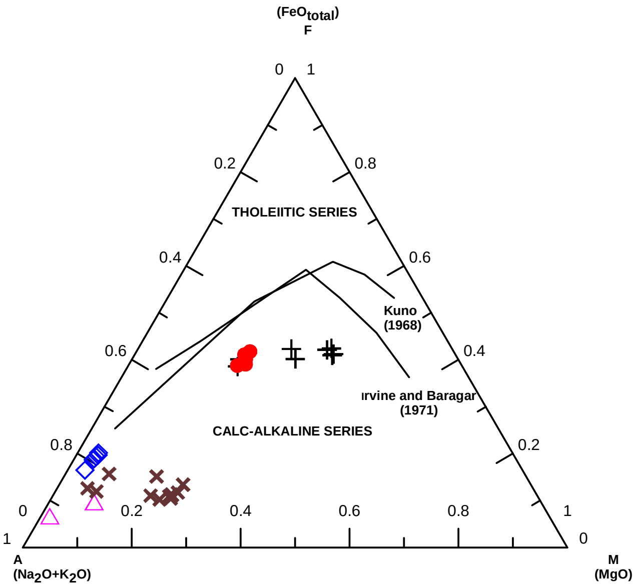

Fig. 2.12: Plot of the Shazand granitoids on AFM diagram showing the boundary between the calc-alkaline field and the tholeiitic field, Kuno (1968) and Irvine & Baragar (1971) (heavy lines).

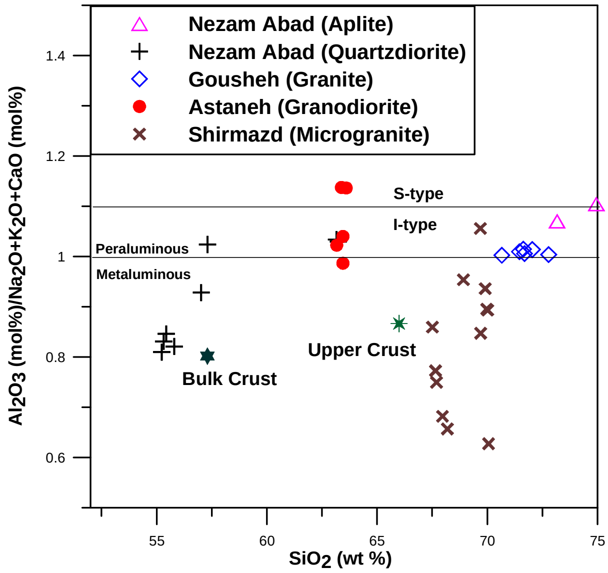

Fig. 2.13: Plot of the Shazand granitoids on aluminnosity-SiO$_2$ variation diagram of Shand (1951), Chappell & White (1974).

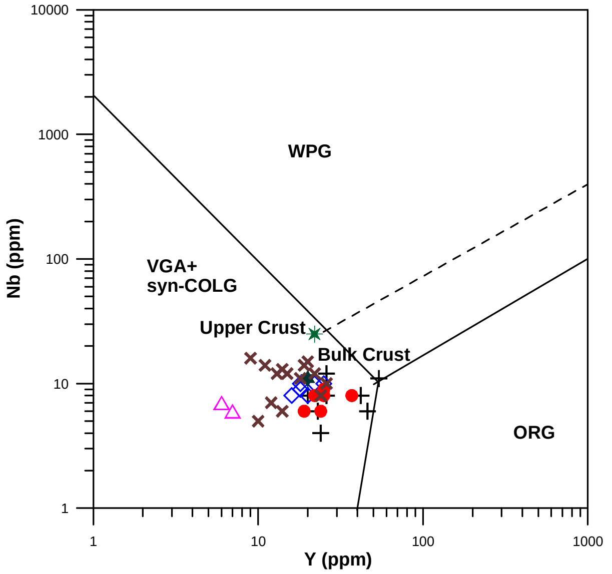

Fig. 2.14: Nb-Y discrimination diagram for granite (after Pearce et al. 1984), showing the fields of volcanic-arc granites (VGA), syn-collisional granites (syn-COLG), within-plate granites (WPG) and ocean-ridge granites (ORG). The broken line is the field boundary for ORG from anomalous ridges.

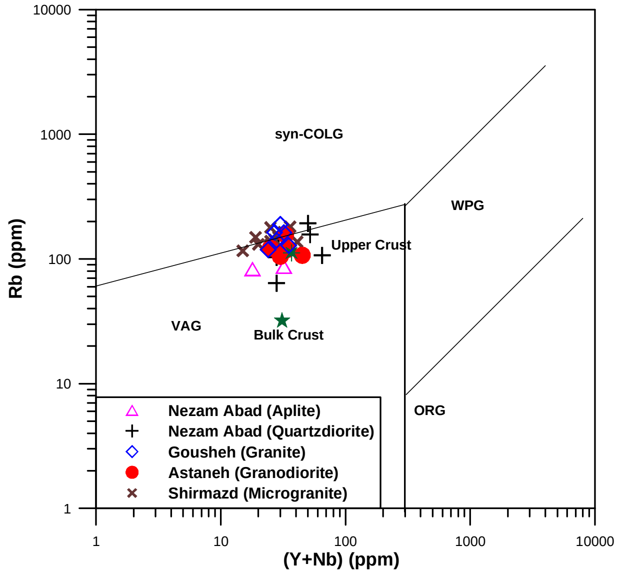

Fig. 2.15: The Rb-(Y+Nb) diagram for granites (after Pearce et al. 1984) showing the fields of syn-collisional granites (syn-COLG), within-plate granites (WPG), volcanic-arc granites (VAG) and ocean-ridge granites (ORG).

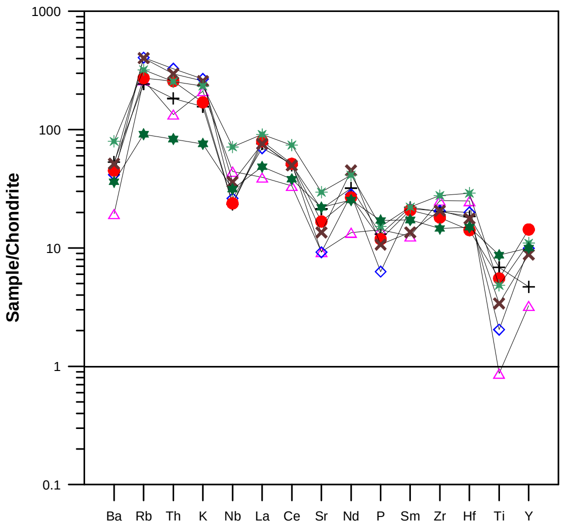

Fig. 2.16: Trace element plot of Shazand granitoids normalized to the composition of chondritic meteorites (Thompson 1982). Upper and mean continental crust from Saunders and Tarney (1984). For source of data see App. 2

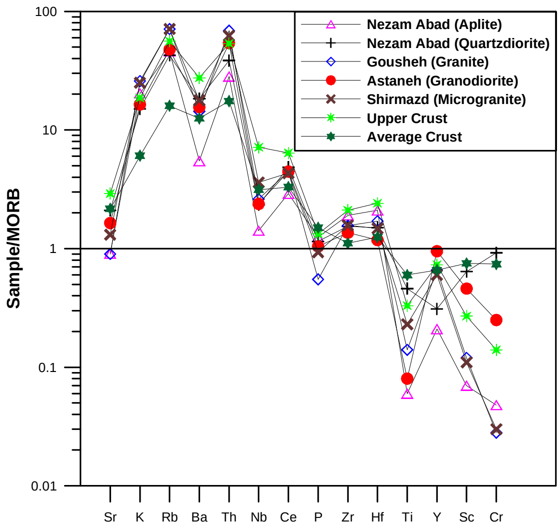

Fig. 2.17: Trace element distribution of the Shazand granitoids normalized to mid-oceanic ridge basalts (Pearce 1983), Sc and Cr from Pearce (1982). See App. 1 and 2 for data base.

samples show enrichment relative to mid-oceanic ridge basalts. This enrichment is typically of the continental crust.

2.6 **Classification of the Shazand granitoids according to Magnetite-Ilmenite series and I-S types**

Some of the criteria of Ishihara (1981) were used to determine the source of the main intrusions (Fig. 2.18, Table 2.4). I-type granitoids are considered to have been generated from igneous source materials and S-type granitoids from sedimentary materials, both originated in the continental crust (White & Chappell 1977). According to White & Chappell (1977), I-type granitoids show a broad compositional spectrum ranging from felsic to mafic with regular inter-element variations within plutons. Correlation diagrams are linear or near linear. On the other hand, the S-type granites are much more restricted and include only rocks with high content of SiO_2. Additionally, their variation diagrams are more irregular than for I-type granites. Field evidence (Gousheh intrusion with alkaline affinity and Nezam Abad with granodiorite to tonalitic composition) together with variation diagrams of the elements coincide with the I-type classification of Chappell & White (1974). According to Ishihara (1981), magnetite series corresponds with I-type, while ilmenite-series can correspond with both I and S types of Chappell & White (1974).

The magnetite- and ilmenite-series granite classification is based on magnetite contents of granitic rocks, and the boundary of the contentens is 0.1 modal percent (Ishihara 1981). As the granite series reflects redox states of granitic magmas, the magnetite- and ilmenite-series correspond to oxidized- and reduced-type, respectively. The distribution of the two granitic series are closely linked to the metallogenic provinces in general, that is, sulfide deposits, such as Cu, Pb, Zn, and Mo, oxide deposits, such as W and Sn, tend to be formed with magnetite- and ilmenite-series granitic rocks, respectively (Ishihara 1981).

2.7 **Isotope data**

The Nezam Abad and the Astaneh intrusions have been dated formerly (Table 2.5). Geochronological results of Masoudi (1997) show that the Nezam Abad complex formed during two main periods (Barremian-Aptian and Maastrichtian), while the Astaneh intrusion formed during the late Albian. On the contrary, the age determination by Farhadian (1991) has revealed slightly younger ages (100.9 ± 1.0 Ma) and (51.8 ± 1.0 Ma) for granodioritic and quartzdioritic parts of the Nezam Abad intrusion, respectively. Age determination of the granodioritic part of the Nezam Abad intrusion via U-Pb dating on single zircon by Farzindoust (2003) has given the oldest age (Table 2.5). Nezafati et al. (2005) reported 35.1±0.9 Ma age for micrograniites of the Shirmad Mountain by Rb-Sr isotope analysis on whole rock. Some samples of the Astaneh intrusion (main phase granodiorite), the Nezam Abad intrusion (main phase quartzdiorite & aplite), hydrothermal tourmaline of the quartz-tourmaline vein in Nezam Abad (chapter 3) and Shirmazd Mountain (microgranite) were analyzed by Rb-Sr and Nd-Sm methods (Table 2.6). The negative ε_{Nd} of quartzdioritic rocks of the Nezam Abad complex and hydrothermal tourmaline (chapter 3) imply a magma, derived from a source with a lower Sm/Nd than Chondritic Uniform Reservoir (CHUR). This means that such rocks and associated hydrothermal tourmaline originated from old crustal rocks whose Sm/Nd had been lowered originally when they separated from CHUR. The T_{DM} age model shows a Proterozoic age of separation of Nd from depleted reservoir. On the contrary, positive ε_{Nd} values of microgranitic rocks of the Shirmazd Mountain, suggest a more mantle-influenced origin (Fig. 2.19).

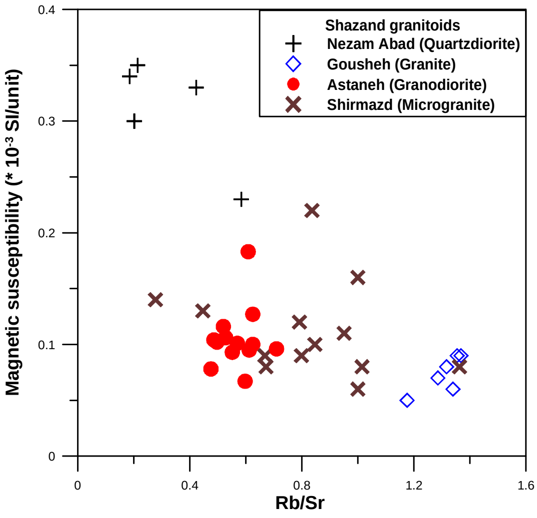

Fig. 2.18: Magnetic susceptibility vs Rb/Sr ratio of the Shazand granitoids.

Table. 2.4: Classification of the Shazand granitoids to the ilmenite/magnetite and I-S type series.

Magnetite Series	Ilmenite Series	Astaneh	Nezam Abad	Gousheh	Shirmazd
Easily recognizable amount of magnetite under the microscope	Practically free of opaque oxide minerals (less than 0.1 vol %), in which ilmenite is consistently seen	Ilmenite-series	Ilmenite-series	Ilmenite-series	Ilmenite-series
High values of magnetic susceptibility (more than 3.0 x 10^{-3} SI/unit)	Low values of magnetic susceptibility (lower than 3.0 x 10^{-3} SI/unit)	Ilmenite-series	Ilmenite-series	Ilmenite-series	Ilmenite-series
Depletion in lithophile element	Enrichment in lithophile elements	Ilmenite-series	Ilmenite-series	Ilmenite-series	Ilmenite-series

I-type	S-type	Astaneh	Nezam Abad	Gousheh	Shirmazd
Relatively high content of sodium (Na_2O) normally more than 3.2 % in felsic varieties and more than 2.2 % in more mafic types	Relatively low content of sodium (Na_2O) normally less than 3.2 % in the rocks with approxmately 5 % K_2O and less than 2.2 % in the rocks with approximately 2 % K_2O	I-type	I-type	I-type	I-type
Al_2O_3/Na_2O+K_2O+CaO (molar ratio) less than 1.1	Al_2O_3/Na_2O+K_2O+CaO (molar ratio) more than 1.1	I-type	I-type	I-type	I-type
Normative diopside or a small amount of normative corundum (less than 1 %)	Large amount of normative corundum (more than 1 %)	I-type	I-type	I-type	I-type
Low initial 87Sr/86Sr (0.704 to 0.707)	High initial 87Sr/86Sr (0.704 to 0.707)	I and Stype	I and Stype	no data	I-S

Table. 2.5: Summary of geochronological data of the Shazand granitoids

Intrusion	Method of dating	Age	Reference
Nezam Abad (quartzdiorite)	K-Ar on hornblende	51.8 ± 1.0 Ma	Farhadian (1991)
Nezam Abad (quartzdiorite)	Rb-Sr on biotite	70.1 ± 1.0 Ma	Masoudi (1997)
Nezam Abad (granodiorite)	K-Ar on biotite	100.9 ± 1.0 Ma	Farhadian (1991)
Nezam Abad (granodiorite)	Rb-Sr on biotite	117.2 ± 1.0 Ma	Masoudi (1997)
Nezam Abad (granodiorite)	U-Pb on single zircon	171.0 ± 1.1 Ma	Farzindoust (2003)
Nezam Abad (aplite)	K-Ar on biotite	30.0 ± 1.0 Ma	Farhadian (1991)
Astaneh (granodiorite)	Rb-Sr on biotite & feldspar	98.9 ± 1.0 Ma	Masoudi (1997)
Shirmazd Mountain (microgranite)	Rb-Sr on bulk rock	35.1 ± 0.9 Ma	Nezafati et al. (2005)

Table. 2.6: Rb-Sr and Nd-Sm isotope data of the Shazand granitoids.

	Sample	Sm	Nd	^{147}Sm/^{144}Nd	^{143}Nd/^{144}Nd	±2σ	Age (Ma)	εNd	Rb	Sr	^{87}Rb/^{86}Sr	±2σ	^{87}Sr/^{86}Sr	±2σ	Initial ^{87}Sr/^{86}Sr	$T_{DM\ (Ga)}$
Nezam Abad																
Main phase																
	NZ-22	3.62	18.43	0.11864	0.512364	4	51.75	-4.83	140.5	263.3	1.5453	130	0.712902	9	0.711766	1.26
	NZ-26	3.55	17.02	0.12618	0.512448	6	51.75	-3.24	73.6	315.2	0.6755	38	0.707583	4	0.707086	1.22
	NZ-27	4.67	23.12	0.12217	0.512283	3	51.75	-6.43	135.6	162.0	2.4230	173	0.713837	5	0.712056	1.44
	NZ-32	4.41	21.36	0.12482	0.512423	4	51.75	-3.72	82.2	386.7	0.6153	44	0.707788	7	0.707336	1.25
Aplite																
	NZ-41	1.41	5.91	0.14427	0.512395	3	30.00	-4.54	212.9	113.0	5.4571	394	0.721074	7	0.718749	1.65
	NZ-43	3.76	17.77	0.12782	0.512347	4	30.00	-5.41	23.3	135.2	0.4980	23	0.710374	32	0.710162	1.42
Tourmaline																
	NZ-36	3.27	13.27	0.14907	0.512432	2	30.00	-3.84	13.6	191.1	0.2064	8	0.707245	5	0.707157	1.69
Astaneh																
Main phase																
	AS-12	3.20	17.91	0.10789	0.512558	7	99.00	-0.44	191.2	221.6	2.4959	388	0.70863	4	0.705123	0.85
	AS-66	5.19	25.06	0.12506	0.512270	2	99.00	-6.28	102.1	183.5	1.6104	104	0.71285	7	0.710587	1.51
Shirmazd																
	AS-109	1.02	7.62	0.08125	0.512696	12	35.00	1.65	221.4	105.6	6.0672	582	0.70767	4	0.704652	0.52
	AS-110	1.88	8.98	0.12658	0.512724	12	35.00	1.99	166.9	348.4	1.3857	10	0.70540	8	0.704709	0.75

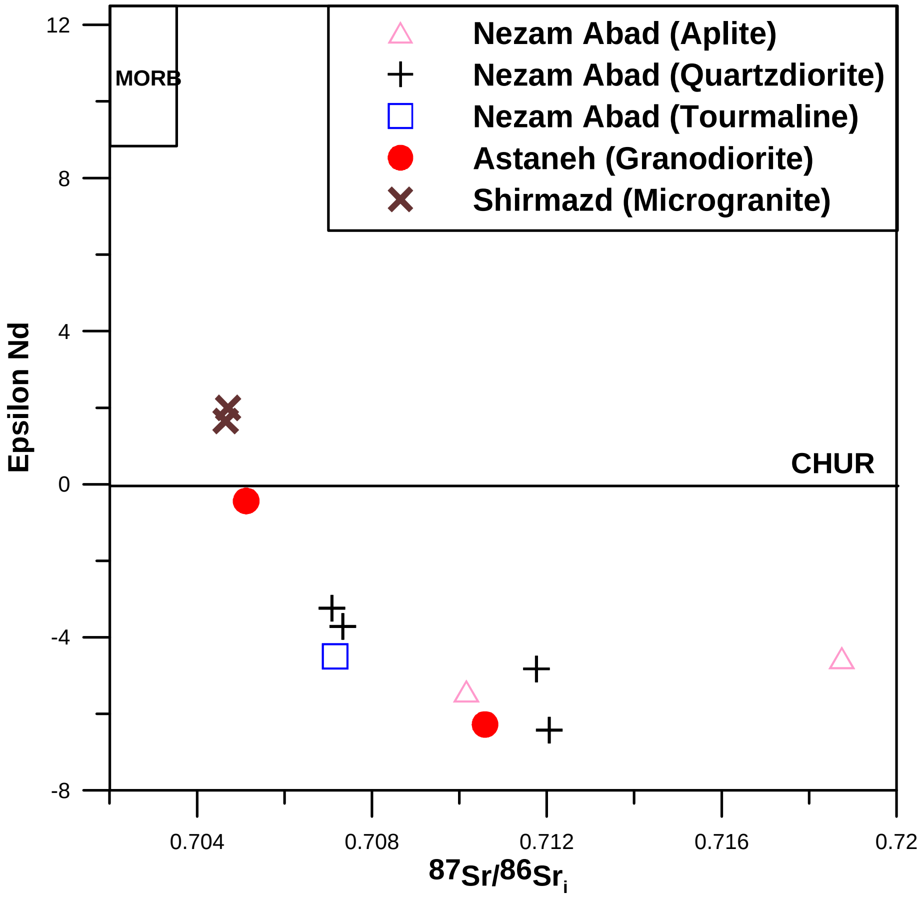

Fig. 2.19: Initial Sr and Nd isotope data for Shazand granitoids.

Chapter 3

3. Nezam Abad W ore deposit

3.1 Introduction

Tungsten mineralization in Iran is related to intrusions of either Mesozoic or Tertiary age (Ghorbani 2002). The first group, is related mostly with Jurassic-Cretaceous acid intrusions in the Sanandaj-Sirjan zone and associated partly with Ag-Au and Sn mineralization. The second group, which is more common is related mainly to Tertiary intrusions with associated Cu, Mo and polymetallic mineralization. Table 3.1 lists and Fig. 3.1 shows the distribution of some of the important tungsten ore deposits and prospects in Iran.

Table. 3.1: Important W ore deposits/ indications in Iran (after Ghorbani 2001).

Ore deposit/ indication	Location	Host rock	Ore minerals
Nezam Abad	southwestern Arak	Cretaceous quartzdiorite	scheelite, cassiterite, sulfides
Chah Kalab	southern Birjand	Jurassic schist, sandstone marble and granite	scheelite, ferberite, sulfides
Chah Palang	southern Anarak	Jurassic schist	Au, wolframite, Bi, sulfide
Deh Hossein	southwestern Nehbandan	Mesozoic rocks	scheelite, wolframite
Tarik Darreh	northwestern Torbate Jam	Jurassic schist	scheelite, arsenopyrite

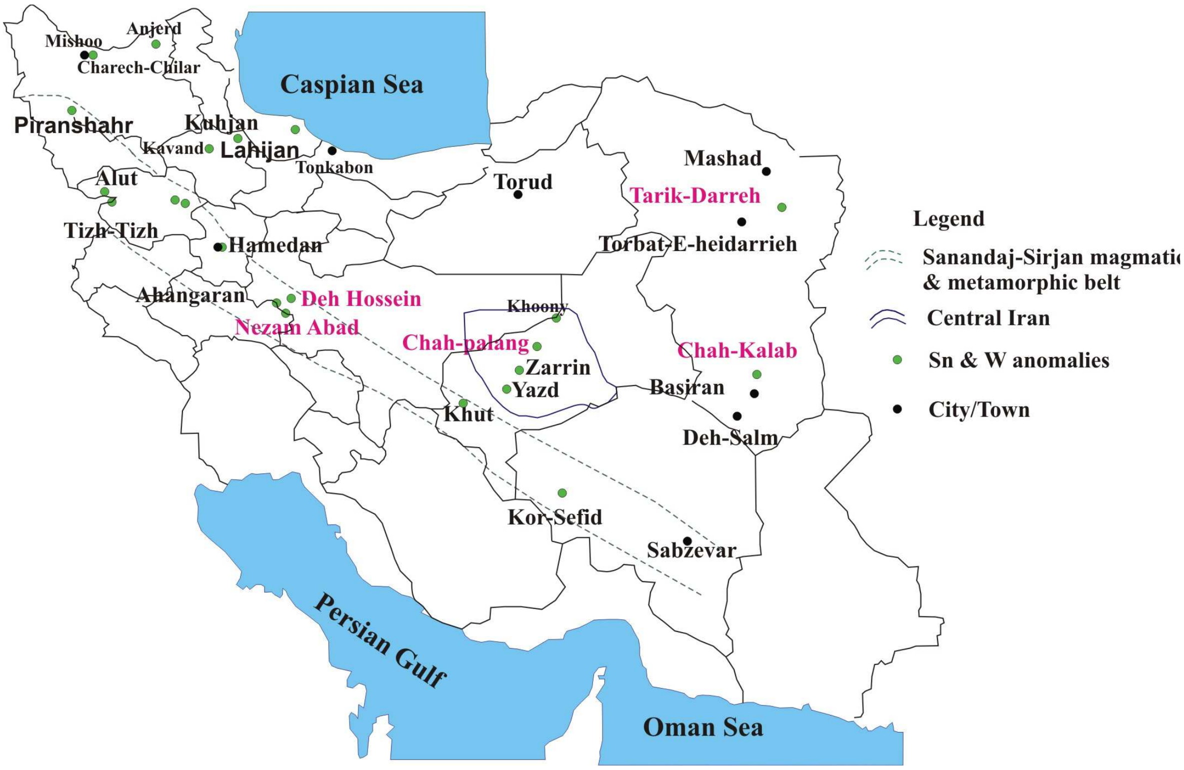

Fig. 3.1: Distribution of the W-Sn ore deposits/prospects in Iran (modified from Jahangiri 1999).

The Nezam Abad mining area has a surface area of about 16 km^2 and is located 4 km southwest of the Nezam Abad village (N 49^{o} 17´ E 33^{o} 40´) (Fig. 1.4). This area has witnessed old and recent exploration activities. Former mining dates back to hundreds of years ago and is manifested by cavings and tunnels. Some people ascribe these old activities to Cu exploration. The goal of more recent has been clearly W and is represented by different trenches, tunnels, boreholes and an abandoned ore dressing plant (Fig 3.2). Jahangiri and Haj Zein Ali (1992) estimated 8000 tons of 0.22 % grade tungsten ore only for the tunnels of the Gorg Valley of the Nezam Abad mining area

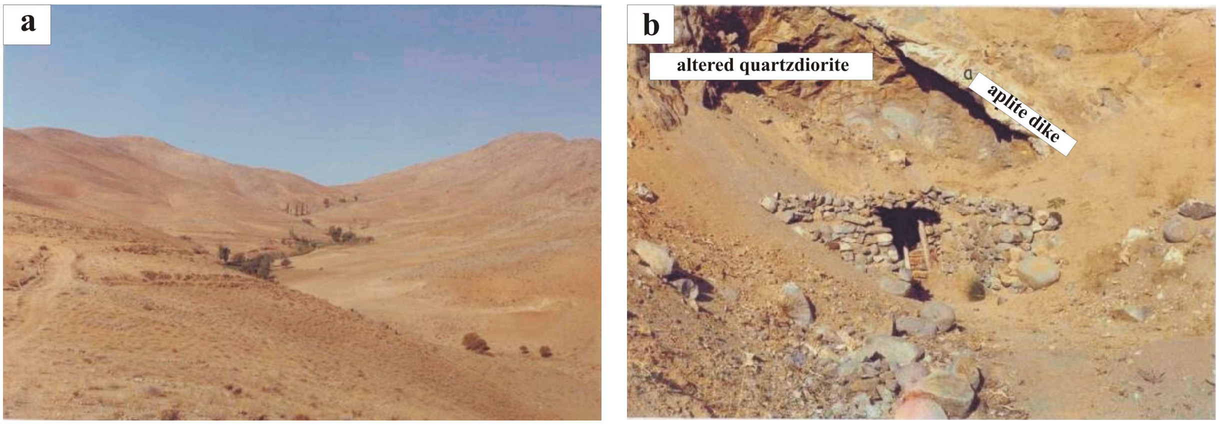

Fig. 3.2: a View of the Nezam Abad mining area. b Exploration tunnel in quartzdiorite, perpendicular to quartz-tourmaline veins, Gorg valley, Nezam Abad mining area.

3.2 **Mine geology**

The geology of the mining area consists mainly of the Nezam Abad intrusive complex (quartzdiorite, tonalite, granodiorite and granite) surrounded by hornfels and Jurassic phyllites (Hamedan schist). Diabasic dikes occur sporadically in these lithologies. Numerous aplite and quartz-tourmaline veins intersect main phase lithologies, particulary quartzdioritic units (Fig. 3.3). Pegmatites with simple mineralogy show remarkable development outside the mining area. The Hamedan Schist has been thermally overprinted by the intrusion of the Nezam Abad complex. Toward the complex, the following facies are distinguishable:

a) Argillaceous schist. These rocks form the outermost part of the metamorphic haloes in the Hamedan Schist with the least thermal effects.

b) Spotted schist. This zone occupies closer parts of the Hameda Schist to the intrusion and is indicated by andalusite and cordierite schists.

c) Hornfels. This zone shows the contact of the Nezam Abad complex and Hamedan Schist and includes different facies comprising micaceous and feldspathic hornfels in the outer and inner parts, respectively. Quartz-tourmaline and aplite veins are explained as follows:

a) Aplite: Aplitic dikes with mostly NW-SE trend (parallel to the Zagros chain) are associated partly with quartz-tourmaline veins (Fig. 3.4). Their thickness varies between 50 cm and 1 m. These rocks have a simple granite mineralogy (Figs. 2.2c, d).

K-Ar isotopic age determination on biotite of an aplitic sample by Farhadian (1991) has given an age of 30 ± 1 Ma (Table 2.4).

b) Quartz-tourmaline veins: These veins are mainly composed of quartz and tourmaline with impregnation of malachite. The NW-SE trending mineralized veins contain scheelite and sulfides and their thickness varies between 0.5 cm and 2 m (Fig. 3.4). More details on tourmaline are given in the next sections.

c) Pegmatite: Pegmatites are developed mainly outside of the study area. These pegmatites are barren and have a simple mineralogy, including quartz, alkali-feldspar, muscovite and tourmaline.

3.3 **Vein mineralogy**

Quartz and tourmaline predominate and comprise more than 95 vol % of the veins. The hydrothermal mineral association of the ore deposit includes scheelite as the only W mineral and a variety of Sn, Cu, As and Bi sulfides with locally elevated Au content. The minerals and their relative age relations were studied in polished and thin sections.

Native elements

Traces of native bismuth and invisible gold occur in the ores. The most persistent of these, bismuth, is closely associated with bismuthinite, both minerals forming inclusions in early arsenopyrite (Fig. 3.5). The presence of bismuthinite demonstrates a relatively high temperature of formation. Bismite occurs as oxide product in arsenopyrite as well. Native gold, despite the partly high gold concentrations found by chemical analysis is invisible, leading to the conclusion that it occurs as invisible gold, either as submicroscopic metallic particles or as chemically bound gold in sulfides (Maddox 1998).

Sulfides

1- **Arsenopyrite**: It occurs as idiomorphic (early crystallization) and idioblastic (late crystallization) grains. Early crystallized grains show cataclastic texture (Figs. 3.5, 3.6). There is not any sign for hypogene replacement. Supergene replacement is evident by covellite, chalcocite and scorodite (Fig. 3.6a). Most arsenopyrite formed early in the vein sequence, associated mainly with pyrrhotite and rare cassiterite (Figs. 3.6b, 3.7c). Inclusions of löllingite ($FeAs_2$) and Bi minerals are abundant (Fig. 3.5b).

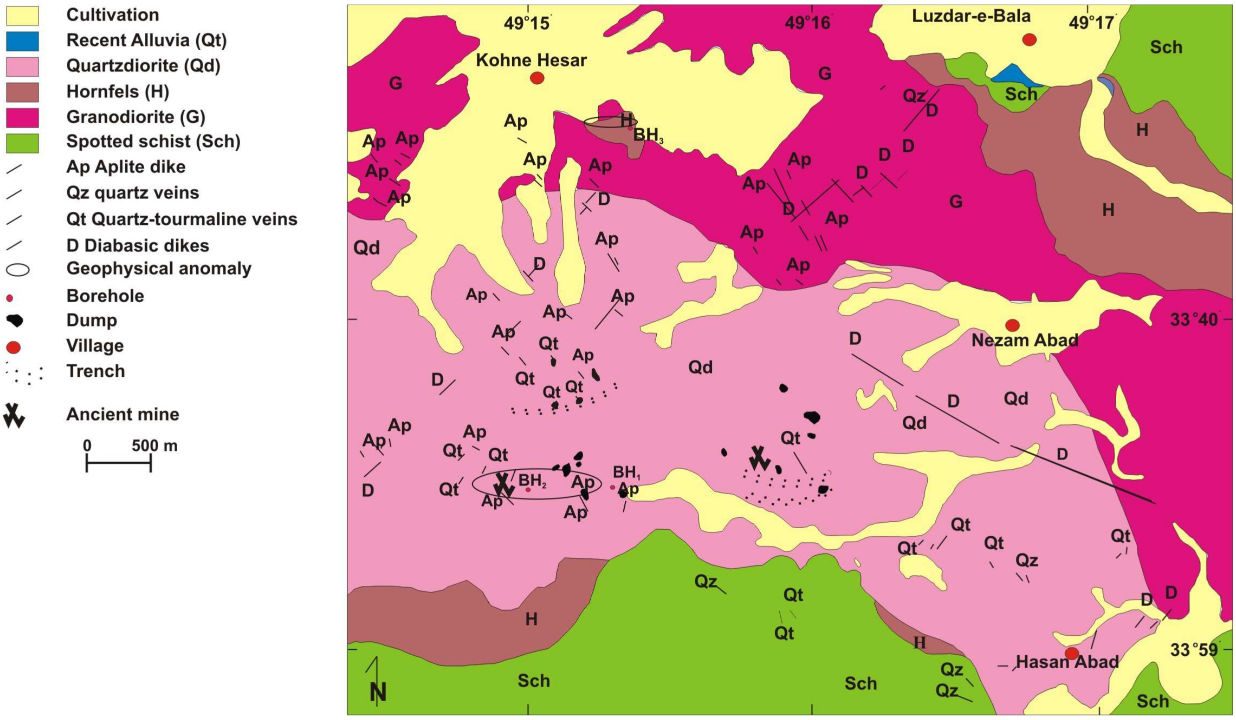

Fig. 3.3: Geological map of the Nezam Abad mining area (modified from Farhadian 1993 & Shamanian1994).

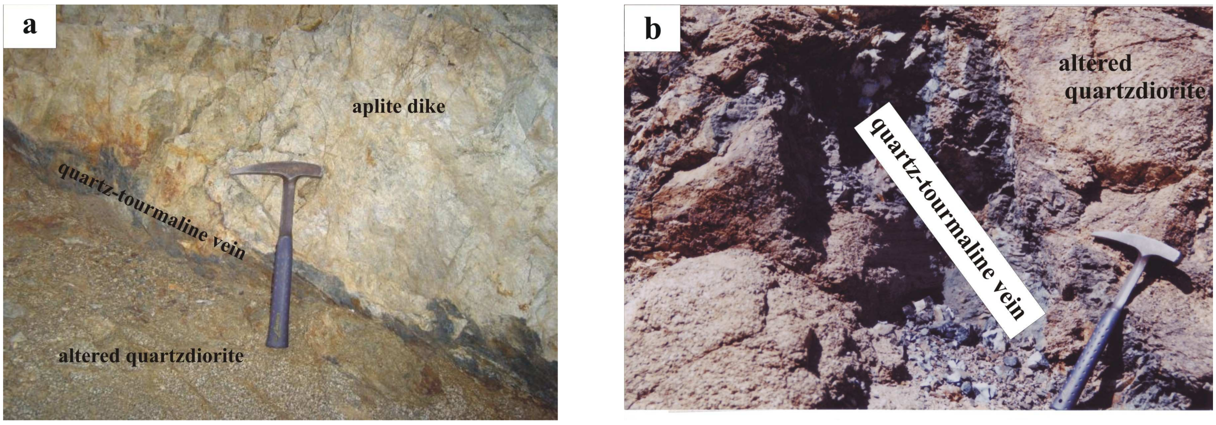

Fig. 3.4: a Altered quartzdiorite intruded by aplitic dike and quartz-tourmaline vein. b Quartz-tourmaline vein in altered quartzdiorite.

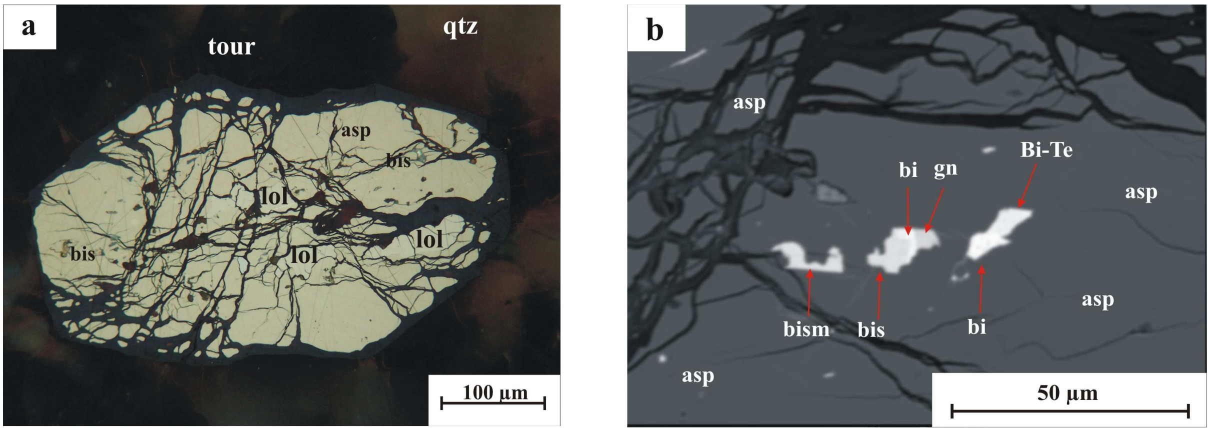

Fig. 3.5: a Cataclastic arsenopyrite with inclusions of bismuth, bismuthinite and löllingite ($FeAs_2$), PPL, oil immersion. b BSE of a section of the arsenopyrite crystal shown in (a).

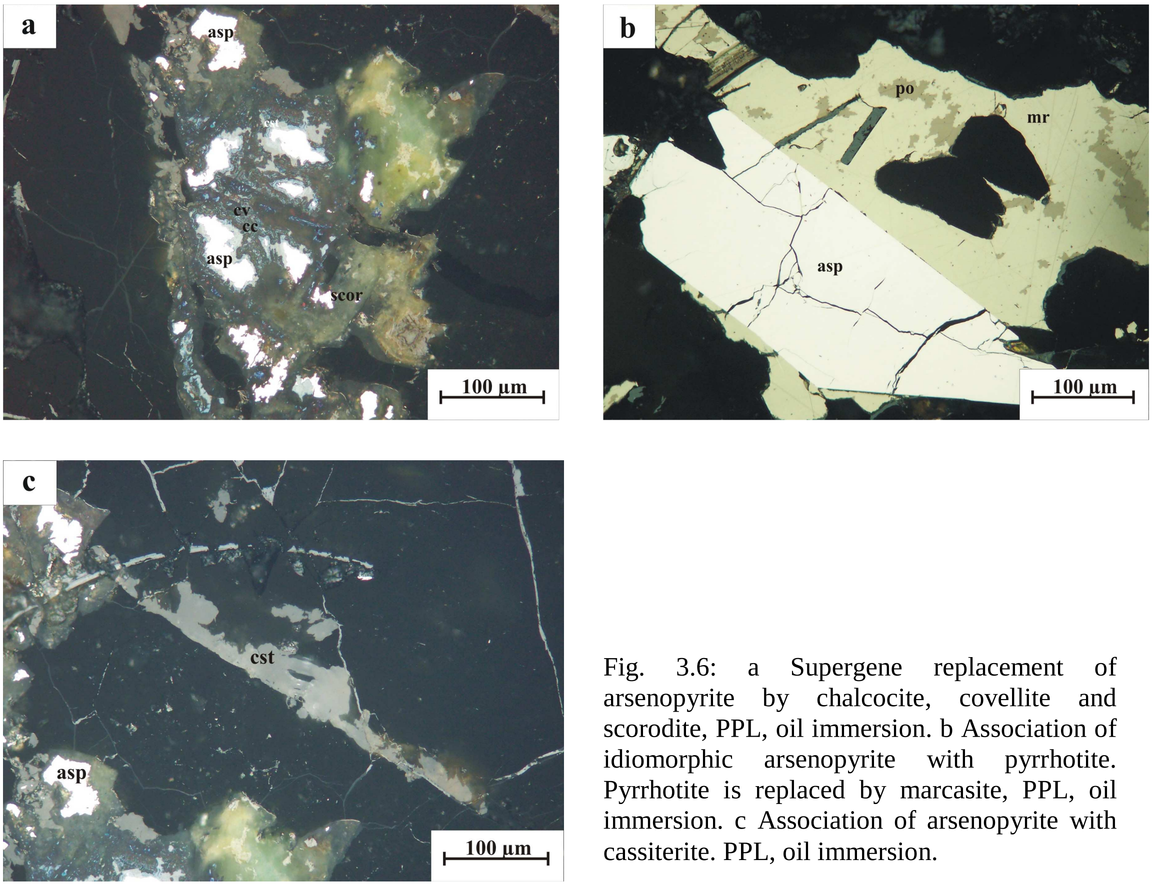

Fig. 3.6: a Supergene replacement of arsenopyrite by chalcocite, covellite and scorodite, PPL, oil immersion. b Association of idiomorphic arsenopyrite with pyrrhotite. Pyrrhotite is replaced by marcasite, PPL, oil immersion. c Association of arsenopyrite with cassiterite. PPL, oil immersion.

2- **Bismuthinite**: Traces of bismuthinite are widespread in the veins. This mineral is usually intergrown with bismuth, both minerals occuring as inclusions in early crystallized arsenopyrite (Figs. 3.5b).

3- **Chalcopyrite**: Chalcopyrite as idioblastic grains is one of the main sulfides in the studied samples and associated mostly with pyrrhotite and rarely arsenopyrite, pyrite and sphalerite. It occurs mainly as tiny veinlets and fracture-filling mineral (Fig. 3.7). Farhadian (1991) reported exsolution of sphalerite and pyrrhotite in chalcopyrite of the drill core samples. Electron microprobe studies on chalcopyrite revealed the presence of cassiterite inclusions (Fig. 3.8).

4- **Marcasite**: Marcasite is very common as a late, hypogene alteration mineral after pyrrhotite. In this mode, it is partly associated with pyrite, both minerals appearing as fine-grained, porous aggregates (Fig. 3.9).

5- **Pyrrhotite**: Pyrrhotite occurs abundantly in the veins, but much was destroyed by the hypogene alteration into marcasite (Fig. 3.10). This replacement corresponds to a worldwide feature of many tin deposits in which an early high-temperature stage of pyrrhotite ± pyrite is followed by a late stage (post cassiterite mineralization) of pyrrhotite alteration to pyrite/marcasite (Kelly & Turneaure 1970). Pyrite or marcasite tend to fully destroy the primary pyrrhotite fabric.

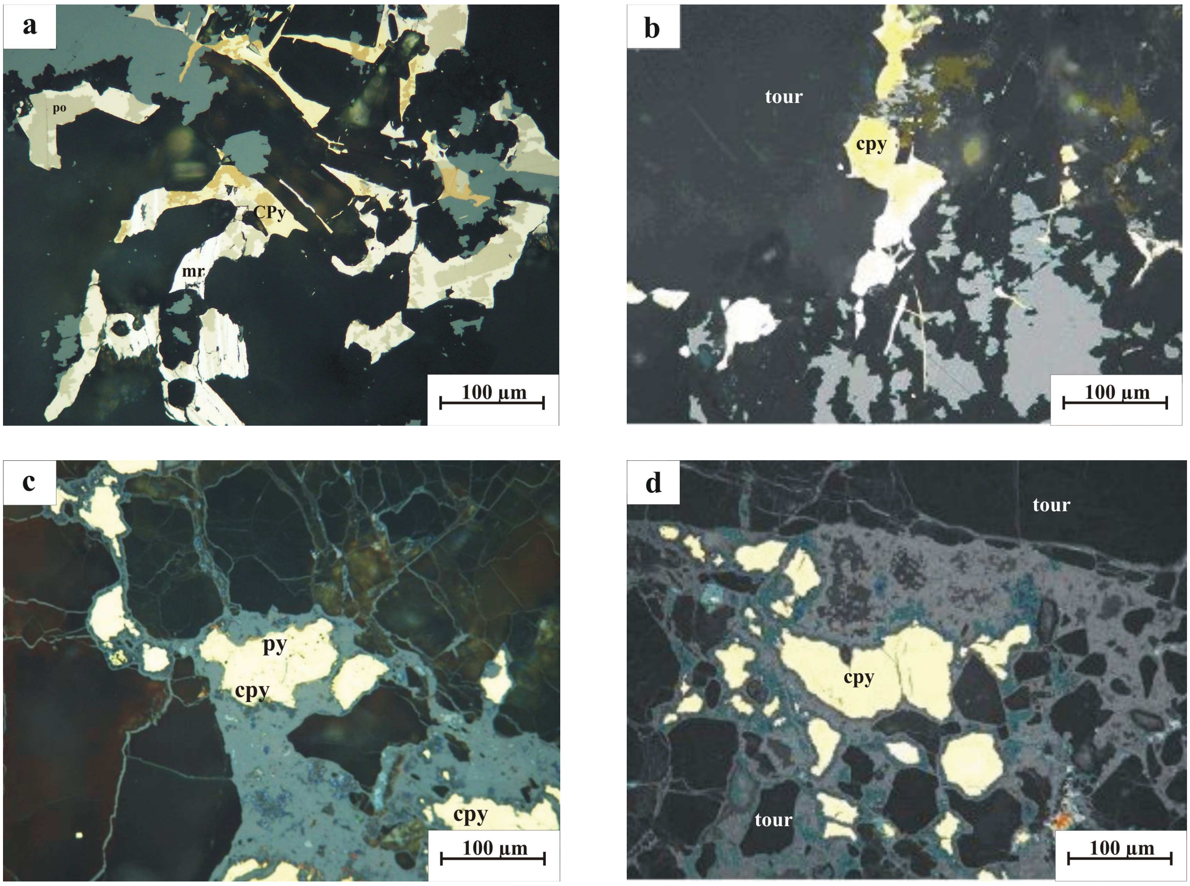

Fig. 3.7: a Association of chalcopyrite with pyrrhotite PPL, oil immersion. b Tiny veinlets of chalcopyrite, PPL, oil immersion. c Association of chalcopyrite and pyrite, PPL, oil immersion. d Brecciated chalcopyrite in tourmaline. PPL, oil immersion

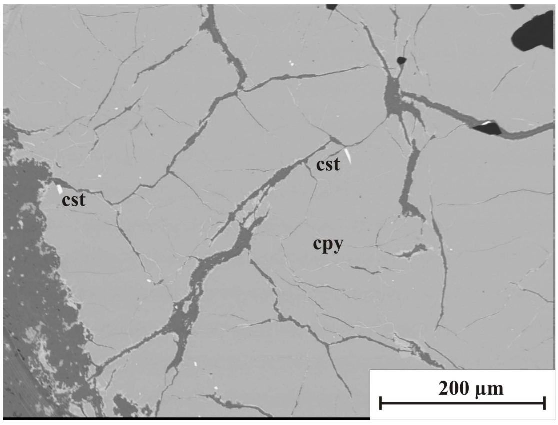

Fig. 3.8: BSE image of chalcopyrite and inclusions of cassiterite.

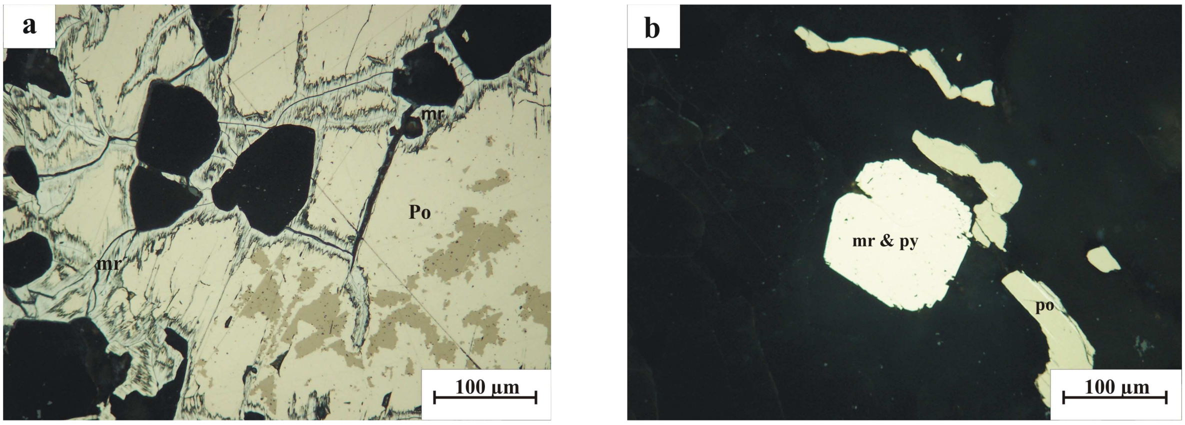

Fig. 3.9: a Hypogene replacement of pyrrhotite by marcasite, PPL, oil immersion. b Aggregate of marcasite and pyrite next to pyrrhotite. PPL, oil immersion.

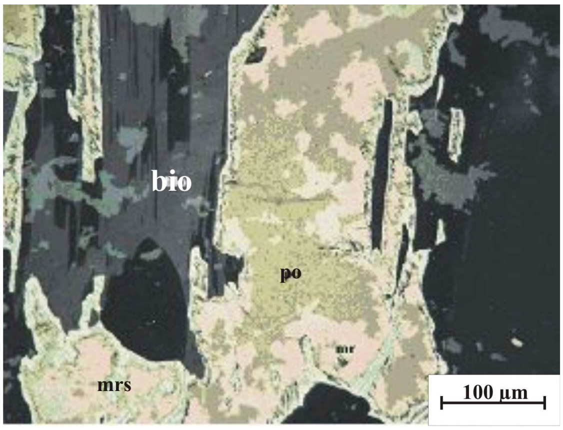

Fig. 3.10: Replacement of pyrrhotite by marcasite. Biotite is evident in this sample. PPL, oil immersion.

6- **Pyrite**: Minor amounts of pyrite are ubiquitous, occurring as idioblastic grains in quartz and fracture-filling in tourmaline or intergrown with marcasite (Fig. 3.11).

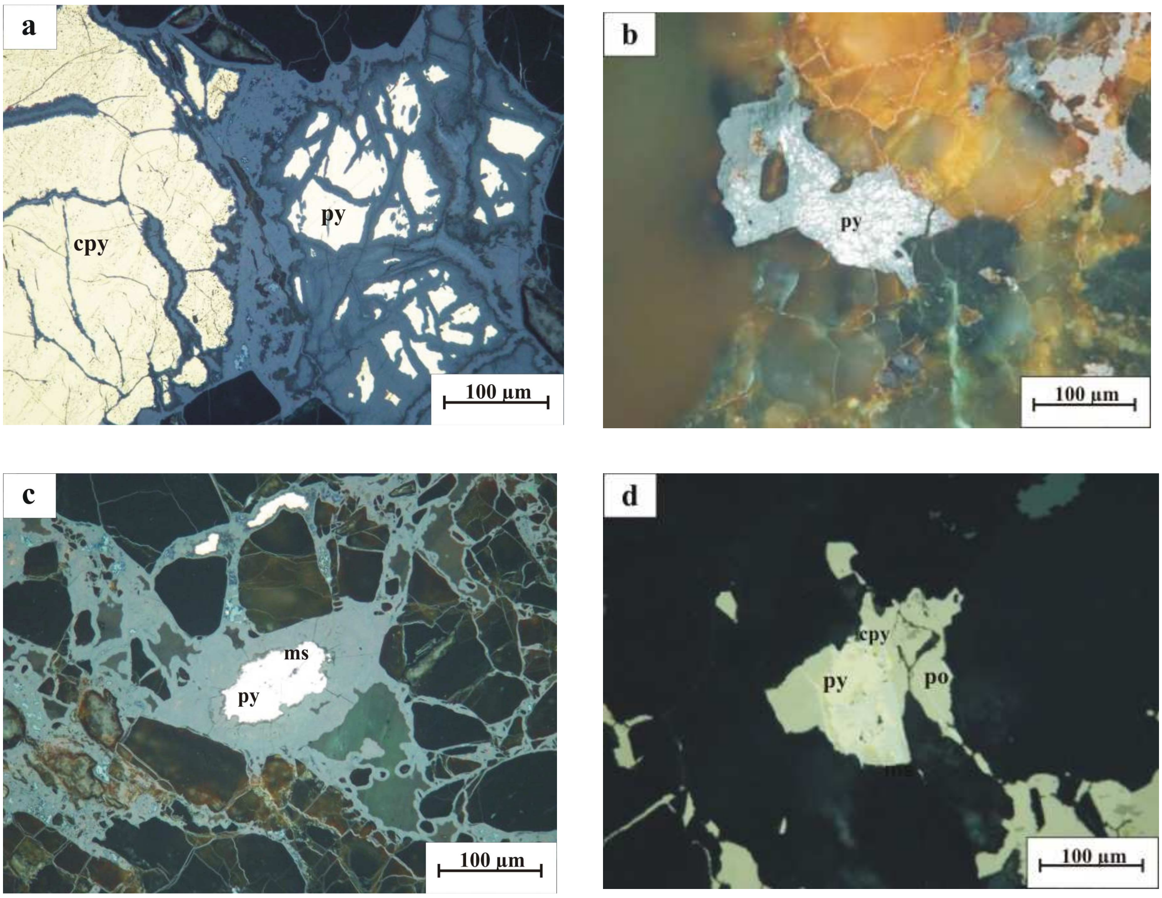

Fig. 3.11: a Association of pyrite with chalcopyrite, PPL, oil immersion. b Brecciated pyrite, PPL, oil immersion. c Fine-grained porous aggregate of pyrite and marcasite, PPL, oil immersion. d Hypogene alteration of pyrrhotite to marcasite and pyrite next to chalcopyrite, PPL, oil immersion.

It shows partly cataclastic texture. The timing of pyrite generations is somehow difficult to decipher, but in general two generations are discernible. The first generation occurs with quartz or tourmaline and the second one is indicated as marcasite-pyrite intergrowth, resulting from hypogene alteration of pyrrhotite.

7- **Sphalerite**: Sphalerite occurs very rare either as small star-like inclusions in arsenopyrite or individual idioblastic grains with pyrrhotite and chalcopyrite. In the first case, sphalerite formed as a primary growth during simultaneous crystallization, rather than exsolution (Fig. 3.12).

8- **Covellite and chalcocite**: Covellite and rarely chalcocite occur as supergene weathering products of arsenopyrite (Fig. 3.7) and chalcopyrite (Fig. 3.8).

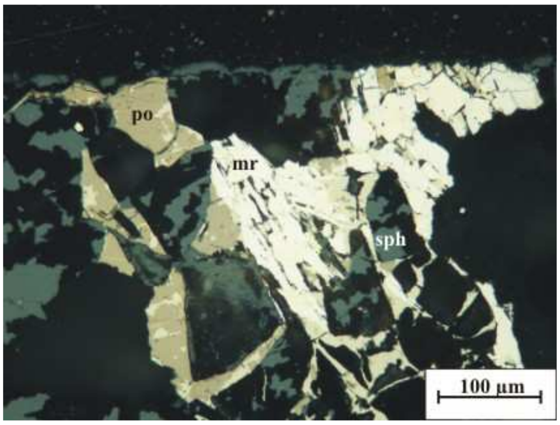

Fig. 3.12. Association of sphalerite with pyrrhotite, PPL, oil immersion.

Oxides

1- **Cassiterite**: Cassiterite occurs either as big elongated or small idioblastic grains in tourmaline and is partly associated with arsenopyrite (Fig. 3.13). It seems that cassiterite is among the earliest vein minerals to have formed. Relative timing of cassiterite and scheelite is disputable, as in the most of the examined specimens the textures are not very clear-cut, but the cassiterite seems to be older.

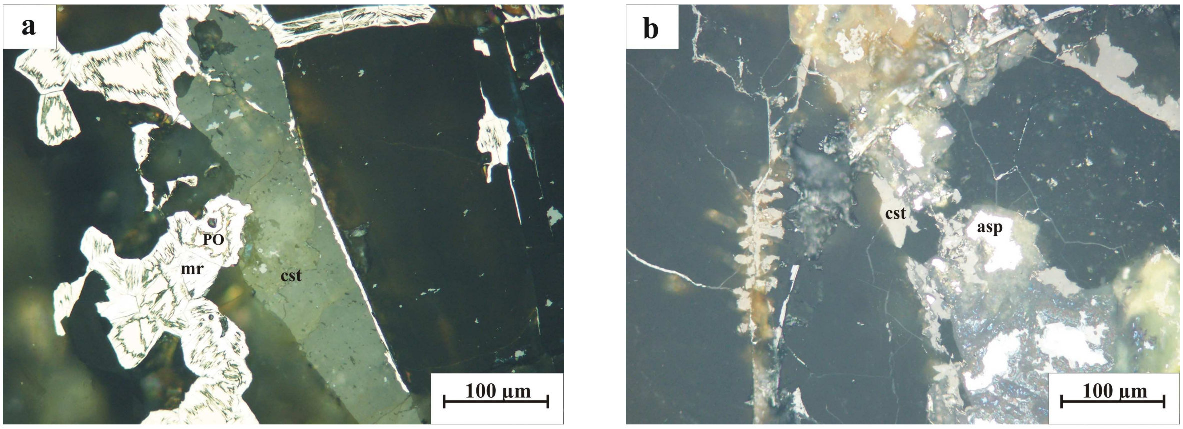

Fig. 3.13: a Big elongated grain of cassiterite in tourmaline next to pyrrhotite. b Small grain of cassiterite in tourmaline next to arsenopyrite, PPL, oil immersion.

2- **Rutile**: Rutile occurs as tiny dispersed grains within the vein quartz and tourmaline (Fig. 3.14). It shows no relation with the main phase of mineralization and possibly formed very early in the paragenetic sequence.

3- **Quartz**: By far the most abundant mineral in the veins, quartz had a prolonged and complex depositional history. As a result of complete vein filling, most of the quartz is massive. Quartz was long lived in the mineralization, overlapping certain other minerals, and its paragenesis is correspondingly complex. The quartz history is further complicated by the fact that the mineral started to form in the earliest vein stages and continued to precipitate in an episodic way into the closing stages of mineralization. Although its deposition was long lived and complicated, the great bulk of the quartz certainly appears to have formed near the onset of vein filling, overlapping to some degree other early minerals like scheelite and tourmaline (Fig. 3.15) and preceding other main sulfides.

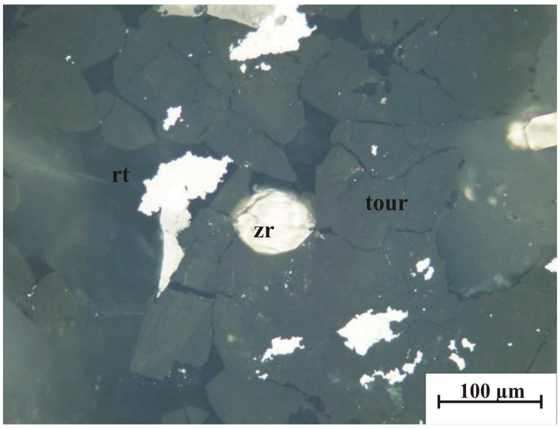

Fig. 3.14: Rutile and idiomorphic zircon with tourmaline, PPL, oil immersion.

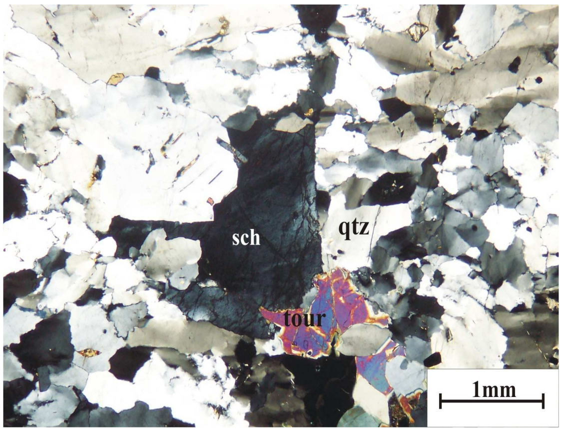

Fig. 3.15: Association of quartz, scheelite and tourmaline, XPL.

4- **Bismite:** Traces of bismite inclusions occur in early arsenopyrite.

5- Limonite: Limonite is fairly common as a secondary weathering product.

Phosphates

Apatite: Electron microprobe study revealed high amounts of fluorapatite inclusions in tourmaline (Fig. 3.16).

Carbonates

Calcite and dolomite: These carbonates occur as thin veinlets together with quartz and tourmaline. Their formation is related to very late phases of mineralization, due to alteration of plagioclase and other Ca and Mg-bearing minerals (Fig. 3.17).

Malachite and azurite:

These are common as secondary minerals, occurring through weathering of Cu ore minerals, mostly chalcopyrite, in the oxidized zone.

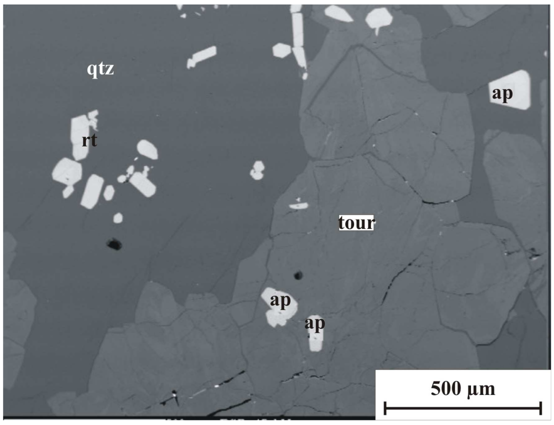

Fig. 3.16: BSE image of apatite inclusions in tourmaline and quartz.

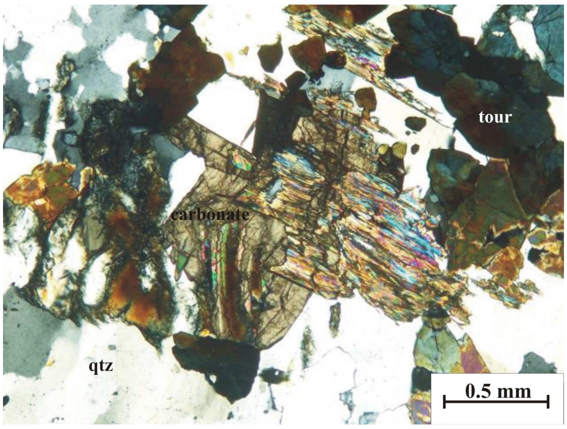

Fig. 3.17: Carbonate in association with quartz and tourmaline, XPL.

Tungstates

Scheelite

Scheelite is the only tungsten-bearing ore mineral in this deposit. In hand specimen, it occurs as disseminated white to pinkish or light green grains in quartz and tourmaline. This association is confirmed by study of polished and thin sections. Scheelite in the studied samples is definitely of primary origin, rather than replacing wolframite (Fig. 3.18).

Silicates

Tourmaline

Tourmaline and quartz are the most important gangue minerals and form the main part of the vein material. Tourmaline and boron are discussed in the next sections.

- Paragenetic sequence

Microscopic and electron microprobe studies of more than 50 polished sections together with field evidence define paragenetic sequence of mineralization (Fig. 3.19). Mineralization took place principally in an early oxide and a late sulfide-rich stage. The oxide stage occurred early in the paragenesis and includes the tungsten mineralization. The study of the paragenesis confirmed an overlap between late scheelite deposition and the main sulfide stage, so that arsenopyrite, pyrrhotite and to a lesser extent chalcopyrite and pyrite were formed partly in the final stages of the W stage. Quartz, rutile, tourmaline, cassiterite and apatite occur together with scheelite in the oxide stage (Fig. 3.19). There are no greisen alteration or Mo mineralization observed in the Nezam Abad area, which may either not exist, or occur at deeper levels not exposed.

3.4 More comments on scheelite, tourmaline and arsenopyrite

3.4.1 Scheelite

Scheelite is the only W-bearing ore mineral in the Nezam Abad mine. The detailed study of polished sections confirmed no replacement of wolframite by scheelite. Secondly, scheelite is pure and shows no solid solution series with other end-members, particularly powellite. The presence of scheelite without wolframite is unusual by comparison with W-Sn greisen-vein deposits elsewhere (Clarke 1983). Scheelite-only mineralization is more typical of stratabound volcano-sedimentary or skarn-hosted W deposits (Hallenstein & Pedersen 1983, Woods & Samson 2000), in which the predominance of scheelite is explained in terms of a Ca-rich environment (Barabanov 1971). Plagioclase can be a major control on scheelite prospect in granite-related greisen-vein deposits (Moore 1977).

Experimental studies of Woods & Samson (2000) on the relative stabilities of scheelite and ferberite are illustrated in the form of three-dimensional plots of the molal concentration ratio Ca/Fe in solution as a function of pH and chloride concentration at selected temperatures and pressures. The surfaces plotted represent the Ca/Fe concentration ratio at which ferberite and scheelite are in equilibrium (Fig. 3.20). At Ca/Fe ratios above the surface, scheelite alone is stable, and at Ca/Fe ratios below the surface, ferberite alone is stable. As it is clear in Figure 3.20, the relative stabilities of scheelite and ferberite are generally not a function of pH. Simple cooling of a solution with a constant Ca/Fe ratio can not result in the replacement of ferberite by scheelite, and field observations of the late-stage replacement of ferberite with scheelite imply an increase in the Ca/Fe ratio of the ore-forming solution concomitant with cooling. Different scenarios can be envisaged for an increase of the Ca/Fe ratio, including retrograde solubility of many Ca minerals or mixing of a Na-rich, W-bearing hydrothermal fluid with a cool, Ca-rich ground water. In the Nezam Abad ore deposit, one of the commom types of alteration is characterized by the remobilization of Ca and it seems that Ca in scheelite is derived from plagioclase. However, other reasons for the absence of wolframite could be possible, considering that Fe is not scarce, being present as abundant arsenopyrite. Two other factors are believed to be important for suppressing wolframite formation: 1- Lower oxygen fugacity and prevailing Fe-sulfide phase (pyrrhotite-arsenopyrite) favor scheelite formation, while higher f_{O2} corresponds to wolframite (Foster et al. 1975). 2- According to Moore (1977), high Ca content of the ore-bearing solutions and lower acidity lead to scheelite formation, while higher acidity is required for wolframite to be formed. The first condition is clearly obvious in the Nezam Abad W ore deposit, while the second one needs more considerations. Detailed study of polished sections from altered quartzdiorite and vein materials showed that scheelite is mostly located at vein margins in altered quartzdiorite, in which deposition has been controlled by neutralization by wallrocks. In the Nezam Abad deposit, destruction of high amounts of plagioclase in the host rocks, i.e. quartzdiorite to tonalite could have increased the ratio of Ca/Fe of the ore-bearing solutions considerably, giving rise to formation of scheelite instead of wolframite.

Scheelite forms a solid solution series with powellite ($CaMoO_4$) (Hsu & Galli 1977). Pure scheelite occurs mostly in hydrothermal and pegmatite deposits. In this case, the amount of Mo reaches rarely more than 5.0 mol percent $CaMoO_4$ in scheelite Conversely, Mo-rich members of the solid-solution series are formed mainly in contact-metasomatic prospects (Hsu & Galli 1973). The fluorescent color of scheelite in ultraviolet light depends on its composition, in which pure scheelite and Mo-rich scheelite are blue and yellow, respectively.

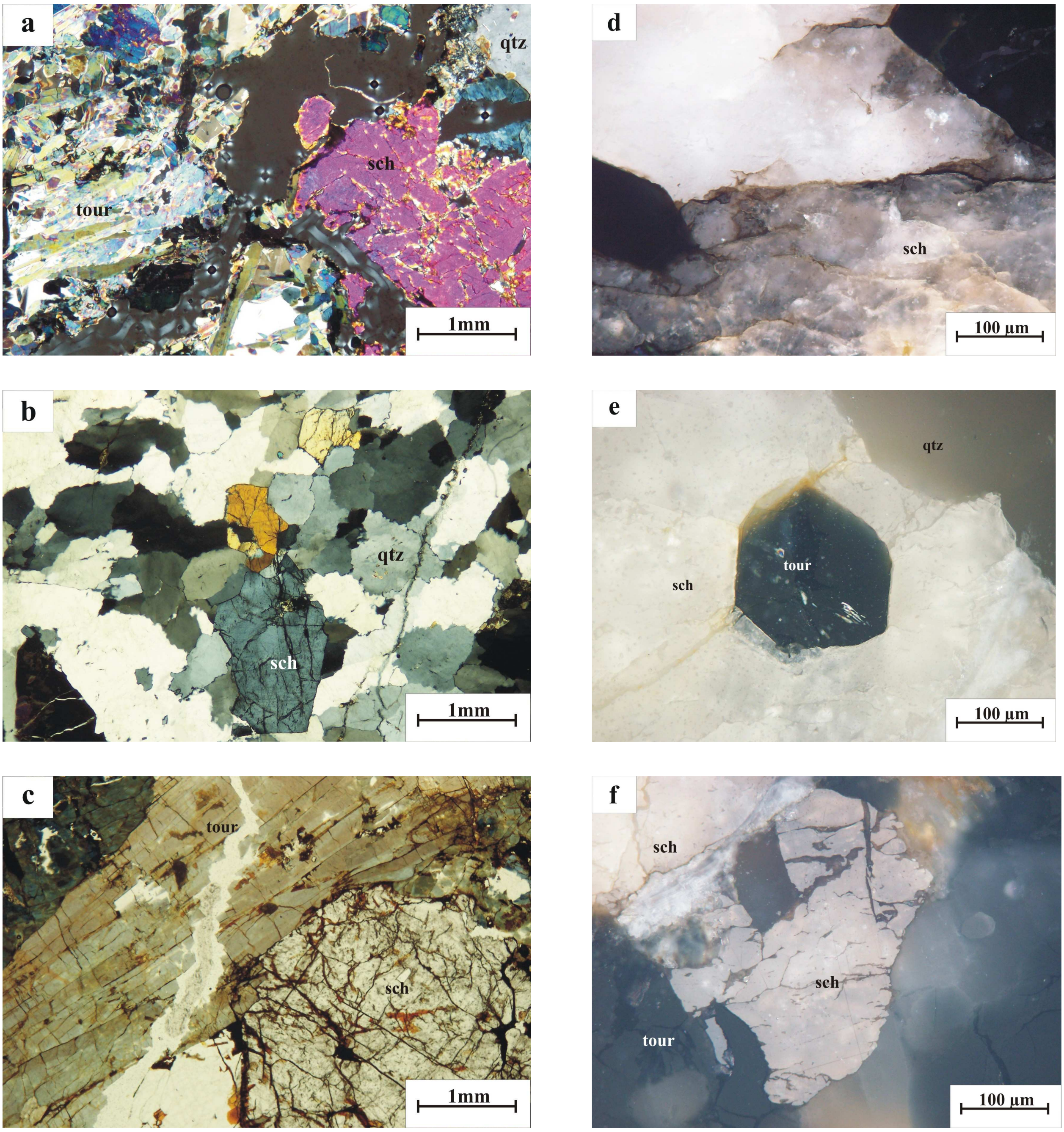

Fig. 3.18: a Association of scheelite with quartz and tourmaline, XPL. b Scheelite in quartz, PPL. c Scheelite in tourmaline, PPL. d Scheelite, PPL, oil immersion. e Scheelite with idiomorphic grain tourmaline inclusion, PPL, oil immersion. f Scheelite in tourmaline, PPL, oil immersion.

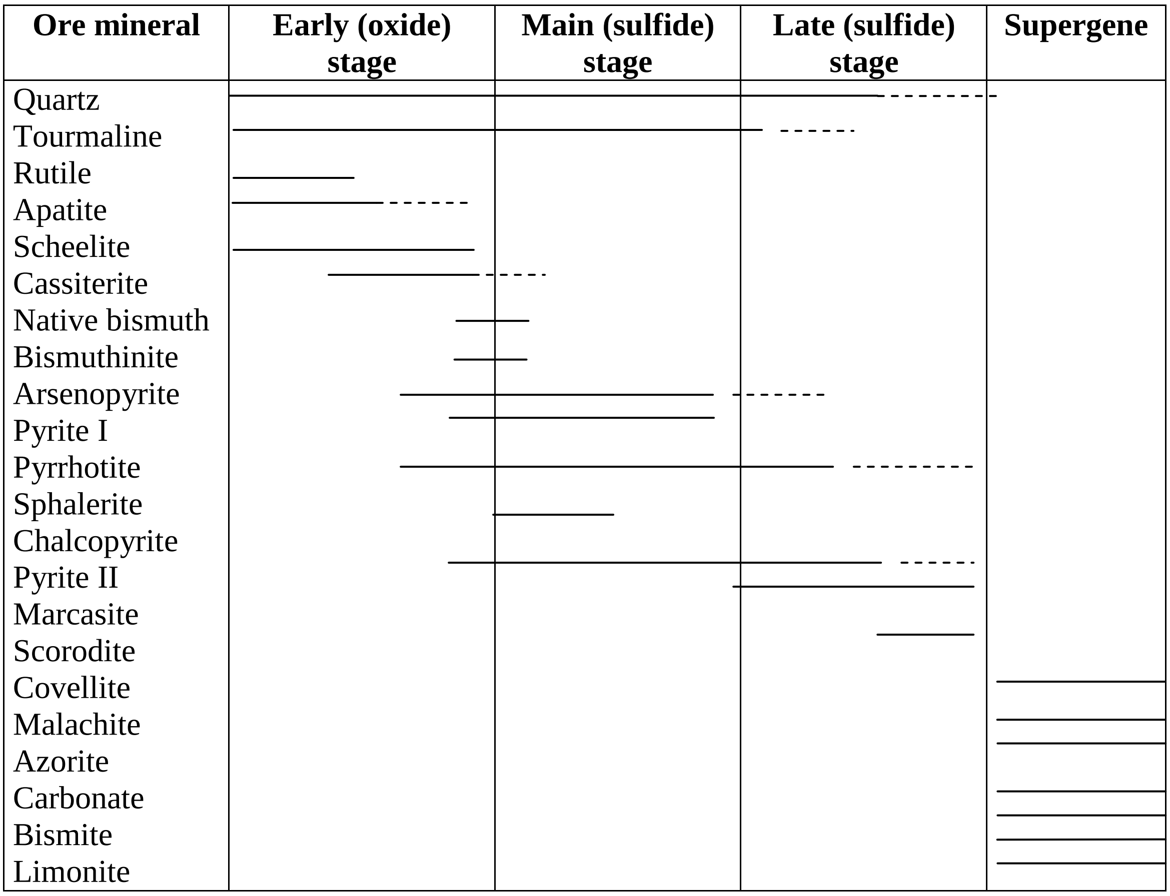

Fig. 3.19: Paragenetic sequence of mineralization in the Nezam Abad W ore deposit.

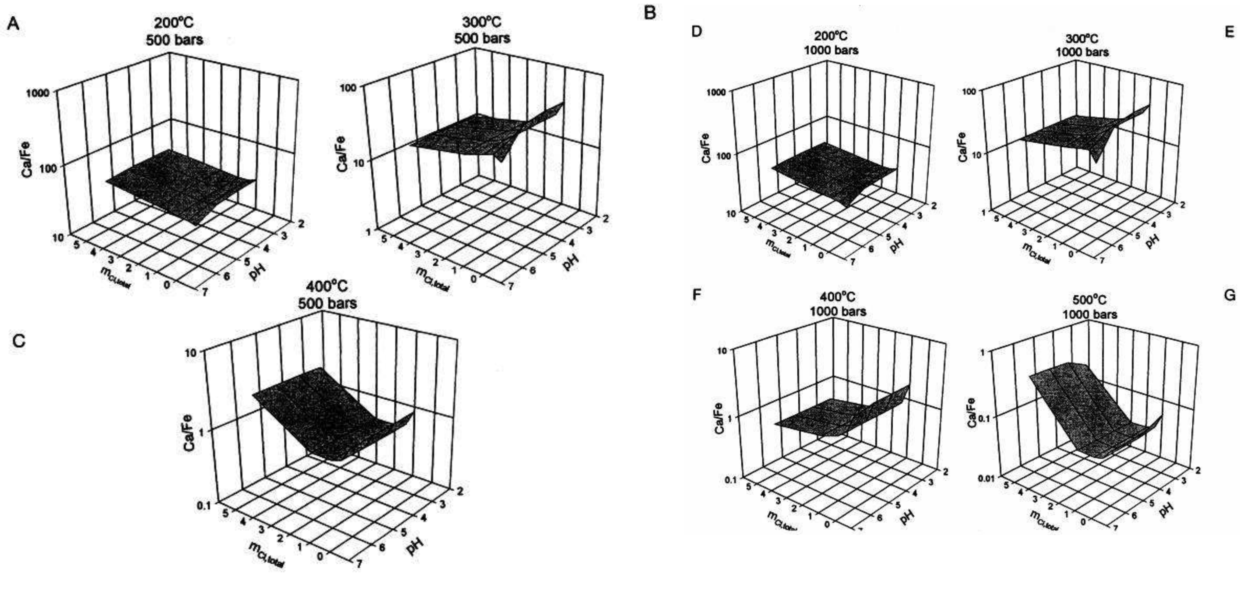

Fig. 3.20: A-G. Calculated molar Ca/Fe ratios in fluids in equilibrium with both ferberite and scheelite as a function of pH and chloride concentrations at selected temperatures and pressures (after Woods & Samson 2000). Scheelite is stable above the dark surface plane, wolframite below.

Electron microprobe analysis of different grains of scheelite in the Nezam Abad ore deposit, as well as the blue fluorescent color showed that Mo is either absent or its amount is below the detection limit, a fact which is supportd by the absence of molybdenite in the veins of the study area. Figure 3.21 illustrates the stability fields for the formation of scheelite, powellite, molybdenite and tungstenite in terms of f_{S2} and f_{O2}.

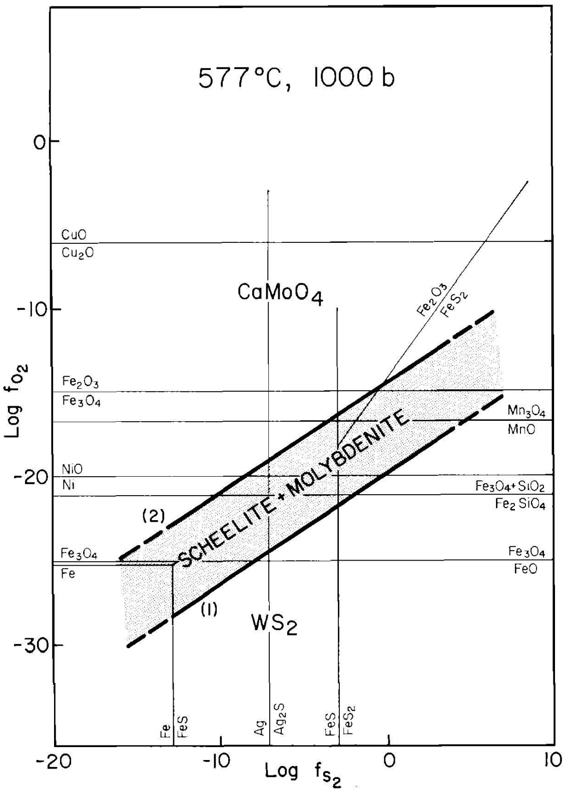

Fig. 3.21: Stability field of coexisting scheelite and molybdenite at 577°C and 1000 bars fluid pressure (after Hsu 1977).

The presence of powellite requires relatively high f_{O2} conditions like a magnetite/hematite assemblage. Molybdenite encloses a large stability field, overlapping the stability field of scheelite, and covers the most common geologic environments. Molybdenite may coexist with scheelite and at higher f_{O2} with powellite. Scheelite is stable over much of the stability field of pyrite.

3.4.2 **Tourmaline and the source of boron**

Tourmaline is an important gangue mineral in metallic and nonmetallic ore deposits. Of these, granitoid-related greisens, veins, skarns, replacements, breccia pipes, and porphyries are of particular importance.

Field evidence shows that the Nezam Abad W deposit is of granitoid-related vein type. Tourmaline formation in the Nezam Abad preceded and partly overlapped W mineralization. Tourmaline occurs very rarely in quartzdiorite and aplites and mostly as fine to coarse-grained crystals in hydrothermal veins. Tourmalinization is the major alteration type and defines the high-temperature center of hydrothermal activity. Boron reduces the solidus temperature of granitic melts and expands the liquidus field of quartz, decreases the viscosity of the melt and increases the solubility of Sn, W, and related incompatible elements in residual magmatic fluids, especially water (London & Manning 1995). This gives rise to important consequences on the development of magmatic-hydrothermal fluids and processes involved in the magmatic-hydrothermal transition.

Crystal chemistry of tourmaline

The general formula of tourmaline is $XY_3Z_6B_3Si_6(O,OH)_{30}(OH,F)$, where common site occupancies include X= Na, Ca, or vacant; Y= Fe^{2+}, Mg, Mn^{2+}, Fe^{3+}, Al, or Li (when coupled with Al); and Z= Al, Fe^{3+}, Mg (when coupled with Ca in X), or $1.33Ti^{4+}$ (London and Manning1995). The end-members of tourmaline types in terms of their X,Y and Z cations are shown in Table 3.2.

Exchange vectors are used to represent the composition of tourmaline in a two dimensional projection (Fig. 3.22). The main purpose is to clarify the chemical variability among the different groups of tourmaline and to apply electron microprobe results to decipher some specific ionic substitutions in tourmaline. In order to show the chemical variability, diagrams of Manning (1982) and Gallagher (1988) were used. In these diagrams, R1, R2 and R3 are similar to X, Y and Z cations of the tourmaline formula, respectively. Table 3.3 presents electron microprobe analyses of tourmaline, while Table 3.4 represents the same data based on atoms p.f.u. The most common chemical variability is in the atomic ratio of Fe/(Fe+Mg) which could be designated by the exchange vector $FeMg_{-1}$, relating the compositions of schorl and dravite. Common substitutions in the tourmaline group are uvite $\{Ca(Fe,Mg)(NaAl)_{-1}\}$, ferric $Fe^{3+}Al_{-1}$, deprotonation $Fe^{3+}O\,(Fe^{2+}OH)_{-1}$, exchange of F for OH, elbaite $LiAlR^{2+}_{-2}$ and $\{[R1]Al\}\{Na(Mg, Fe)\}_{-1}$ which generates an alkali-deficient composition (Fig 3.23). In this figure, R1= Na+Ca, R2= $(Fe_{total}+Mg+Mn^{2+})$, R3= (Al+1.33Ti) and $R2^{*}$= FeO+MgO+MnO+Al in R2. For most of the studied samples, the compositions of tourmaline plot along and between the proton and alkali-deficient end members (Fig. 3.22a). The quantity

Table. 3.2: Tourmaline group (after Deer et al. 1992).

Mineral	X (R1)	Y(R2)	Z(R3)
Elbaite	Na	Al, Li	Al
Olenite	Na	Al	Al
Dravite	Na	Mg	Al
Schorl	Na	Fe+2	Al
Tsilaisite	Na	Al, Mn	Al
Buergerite	Na	Fe+3	Al
Liddicoatite	Ca	Li, Mg	Al
Uvite	Ca	Mg	Al, Mg
Feruvite	Ca	Fe+2	Al, Fe+3, Mg

of Al, as atoms p.f.u. in R2 vs. Fe/(Fe+Mg) indicates the Al deficiency in R3 (value < 0) of quartzdioritic sample.The ratio of Fe/(Fe+Mg) decreases from quartzdioritic host to the hydrothermal vein, indicating more affinity to dravite and schorl members of dravite-schorl solid solution, respectively (Fig 3.22b). Except one sample, all tourmalines are located below the line Σ (Fe+Mg)=3 confirming Al substitution in R2. The lower amount of Al p.f.u of one sample (NZ-43) also indicates Al deficiency. All studied tourmalines show no elbaite component, as they lie above or along the line of $R2^{*}$= 3 atoms p.f.u (Fig. 3.22d). Despite the limited data of electron microprobe analysis on tourmalines, specifically in quartzdioritic host rocks, it can be seen that the composition of tourmalines in quartz-tourmaline veins partly overlaps with those in the igneous host, but with following differences:

a) larger variation of Fe/(Fe+Mg), with generally lower values than in the igneous host.

b) slightly lower F content.

Chemistry of the tourmaline samples

Microscopic study together with electron microprobe data demonstrated some optical and compositional differences between tourmaline in quartzdiorite and hydrothermal veins. It should be noted that pleochroic color does not always correspond to the chemical composition. In other words, optical zonation which is originated possibly from the variation of Fe^{2+}/Fe^{3+}, does not correlate always with considerable chemical contrast. Conversely, some optically unzoned grains can be zoned chemically. Nevertheless, it is possible to link the pleochroic color and zonation of tourmaline to its mode of formation, i.e. igneous or hydrothermal. Since the changes in pleochroic hue, intensity or zonation are not compatible clearly always with composition, backscattered electron images were applied to show compositional differences such as relative variations in Fe/(Fe+Mg) and test if optical zonation correlates with chemical contrast (Fig. 3.23).

Tourmaline in quartzdiorite: This is chemically unzoned and occurs sporadically as disseminated anhedral interstitial grains that display blue-green color (Fig. 3.25a, b). There is no sign of any reaction relationships among tourmaline and other AlFeMg minerals. The fluorine content of disseminated tourmaline in quartzdiorite is slightly higher than for analytical detection limit. The ratio of Fe/(Fe+Mg) changes between 0.69-0.78 which is higher than for tourmalines in hydrothermal veins. According to Benard et al. (1985), tourmaline, especially solid solution close to the schorl-dravite may be a stable liquidus phase of granitic magmas. In a closed magmatic system P, T and composition vary gradually, so crystalline phases such as tourmaline represent little or no chemical changes. This fact conforms to the tourmaline of the study area. Furthermore, it appears that tourmaline crystallized late in the quartzdiorite of the study area, because it mostly occurs as anhedral interstitial grains.

Tourmaline in hydrothermal veins: It occurs in quartz-tourmaline veins within the Nezam Abad intrusion. There are no tourmaline breccias within granitoid or metamorphosed host rocks or pervasive contact replacements of host rock. Quartz-tourmaline veins of both barren and mineralized types are quartz-rich fracture fillings with massive tourmaline borders and comparatively sharp contacts with the adjacent host quartzdiorite. A general characteristic of vein-associated tourmalines is very complex optical and chemical zonation, which is more obvious in backscattered images than in optical thin sections (Fig. 3.24). Zonation is mostly oscillatory, but sometimes shows systematic variation in chemical trends from core to rims of the crystals. To confirm any coincidence between optical and chemical zonation, different points of darker and brighter parts along three optically-zoned tourmaline grains were analyzed (Fig. 3.24 and Table 3.4). Si, Mn, Mg and Al show no major change and remain mostly constant, while Fe, Ca, and to a lesser extent Na increase in the brighter parts and decrease in the darker parts. Ti shows the opposite behavior.

Pleochroic color ranges from orange-brown, blue-gray to greenish, and there is no clear correlation between pleochroic color and composition. Figure 3.25 illustrates various aggregates tourmaline of in quartzdiorite and hydrothermal veins of some of the studied samples.

Origin of boron

The Nd-Sm isotope data of hydrothermal tourmaline and quartzdiorite (Table. 2.6 & Figure. 2.19) coincide and therefore suggest a cogenetic relationship. The source material for both quartzdiorite and tourmaline has a mean age of crustal residence of 1.2-1.7 Ga, i.e. is the lower crust. The $\delta^{11}B$ values of tourmaline in mineralized and barren hydrothermal veins from Nezam Abad show the range of -2.7 to -10.56 ‰ and -6.66 to -8.22 ‰, respectively (Ahmad Khalaji 2006). These ranges are in accordance with continental crust. The geochemical and petrographical data show that the fraction of the melt that attained saturation in tourmaline was very small. This is documented by very low amount of B_2O_3 in quartzdioritic rocks (20-30 ppm) (Ahmad Khalaji 2006) and absence of disseminated tourmalines without fine-scale chemical zonation. According to London and Manning (1995), disseminated tourmaline that lacks fine-scale chemical zonation is the most compelling evidence of igneous tourmaline.

Table. 3.3: Average electron microprobe analyses of tourmaline in quartzdiorite and quartz-tourmaline veins.

Sample	**NZ-5**	**NZ-8**	**NZ-14**	**NZ-30**	**NZ-41**	**NZ=43**	**RV-2**
	N=30	**N=15**	**N=10**	**N=10**	**N=10**	**N=8**	**N=6**
F	bdl	bdl	bdl	bdl	0.17	0.17	bdl
Na_2O	1.49	1.68	1.80	1.85	1.67	1.70	1.86
MgO	7.70	6.40	5.76	5.95	3.13	7.35	7.15
Al_2O_3	32.13	32.6	33.21	32.03	35.88	30.90	32.45
SiO_2	36.32	37.24	35.96	36.84	35.99	35.81	37.39
CaO	2.14	1.44	1.22	1.23	0.54	0.67	1.25
TiO_2	0.66	0.55	0.21	0.92	0.41	1.21	0.47
FeO	7.61	9.14	9.60	10	11.25	11.34	8.36
Cr_2O_3	0.02	0.03	0.01	0.02	0.01	0.01	0.02
MnO	0.05	0.05	0.06	0.05	0.09	0.08	0.04
B_2O_3	11.82	10.80	12.18	11.06	10.88	10.88	10.96
Total	100	100	100	100	100	100	100
FeO/FeO+MgO	**0.50**	**0.59**	**0.63**	**0.63**	**0.78**	**0.60**	**0.60**
Na_2O/Na_2O+CaO	**0.41**	**0.54**	**0.59**	**0.60**	**0.75**	**0.71**	**0.59**

N: Number of analyzed points in each sample. bdl: Below detection limit. Detection limit for F is 1000 ppm.

Samples (NZ-41 and NZ-43) are quartzdiorite. RV refers to Revesht tunnel in the Nezam Abad minign area. Boron values were calculated as difference to 100 %.

Table. 3.4: Average composition of tourmaline from Nezam Abad. Values are atoms p.f.u, normalized to 24.5 O atoms.

Sample	**NZ-5**	**NZ-8**	**NZ-14**	**NZ-30**	**NZ-36**	**NZ-41**	**NZ=43**	**RV-2**
	N=30	**N=15**	**N=10**	**N=10**	**N=7**	**N=10**	**N=8**	**N=6**
Na	0.461	0.551	0.568	0.561	0.547	0.502	0.534	0.574
Mg	1.862	1.631	1.41	1.439	1.407	0.755	1.790	1.703
Al	6.095	6.510	6.381	6.079	6.361	6.794	5.904	6.089
Si	5.853	5.564	5.874	5.943	5.586	5.794	5.813	5.964
Ca	0.367	0.262	0.205	0.203	0.205	0.092	0.115	0.213
Ti	0.079	0.132	0.025	0.111	0.025	0.049	0.147	0.562
Fe	1.015	1.285	1.304	1.335	1.300	1.506	1.534	1.111
Mn	0.002	0.004	0.00	0.002	0.001	0.001	0.001	0.002
Fe/Fe+Mg	0.352	0.440	0.48	0.481	0.480	0.666	0.461	0.394
Na/Na+Ca	0.553	0.677	0.734	0.734	0.727	0.845	0.821	0.729
R1	0.826	0.813	0.773	0.764	0.752	0.594	0.649	0.787
R2	2.879	2.920	2.716	2.776	2.707	2.261	3.325	1.687
R1+R2	3.707	3.733	3.489	3.540	3.459	2.855	3.974	2.474
R3	6.200	6.685	6.414	6.226	6.394	6.859	6.099	6.836
XAl	0.053	0.249	0.288	0.169	0.250	0.653	-0.080	0.80

R1= Na+Ca, R2= Fe+Mg+Mn, R3= Al+1.33 Ti, X Al= Al+1.33 Ti+Si-12= Al in R2, N= Number of analyzed points in each sample.

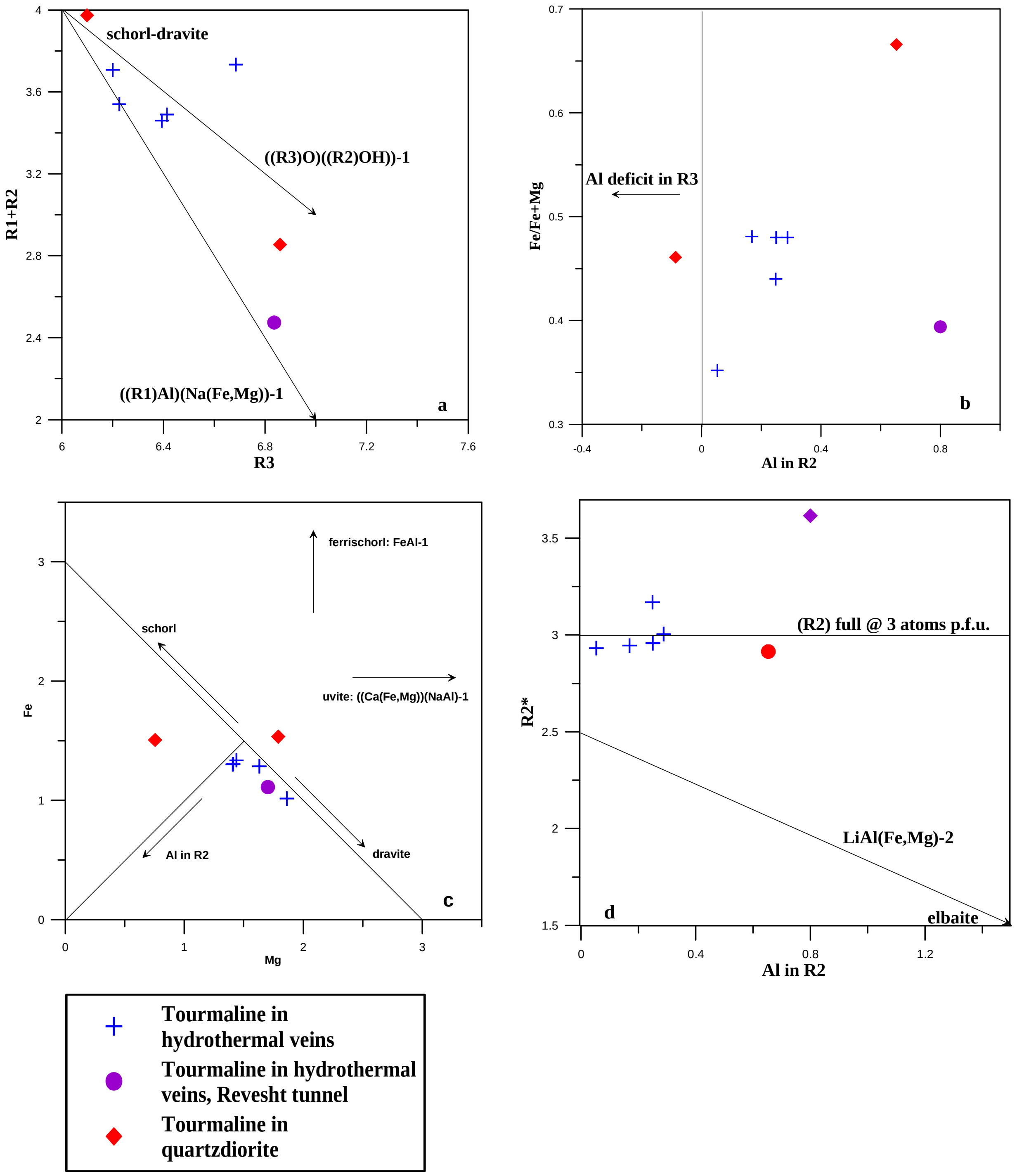

Fig. 3.22: Plots of average cation occupancies of tourmaline from the Nezam Abad mining area. a The sum of sites R1+R2 vs. R3. b Variation of Fe/(Fe+Mg) vs. Al in R2, in which the values of Al in R2 <0 indicate a deficit of Al in R3. c Fe/Mg ratio, schorl-dravite plot along the line Σ(Fe+Mg)=3; values of Σ(Fe+Mg) <3 correspond to Al substitution in R2; arrows show regions beyond Σ(Fe+Mg) =3 where dravite and ferrischorl compositions would plot. d Occupancy of R2* (FeO+MgO+MnO+Al in R2) vs. Al in R2 in atoms p.f.u. Elbaite lies at R2* = Al in R2 = 1.5; the Li content p.f.u = 3- R2*.

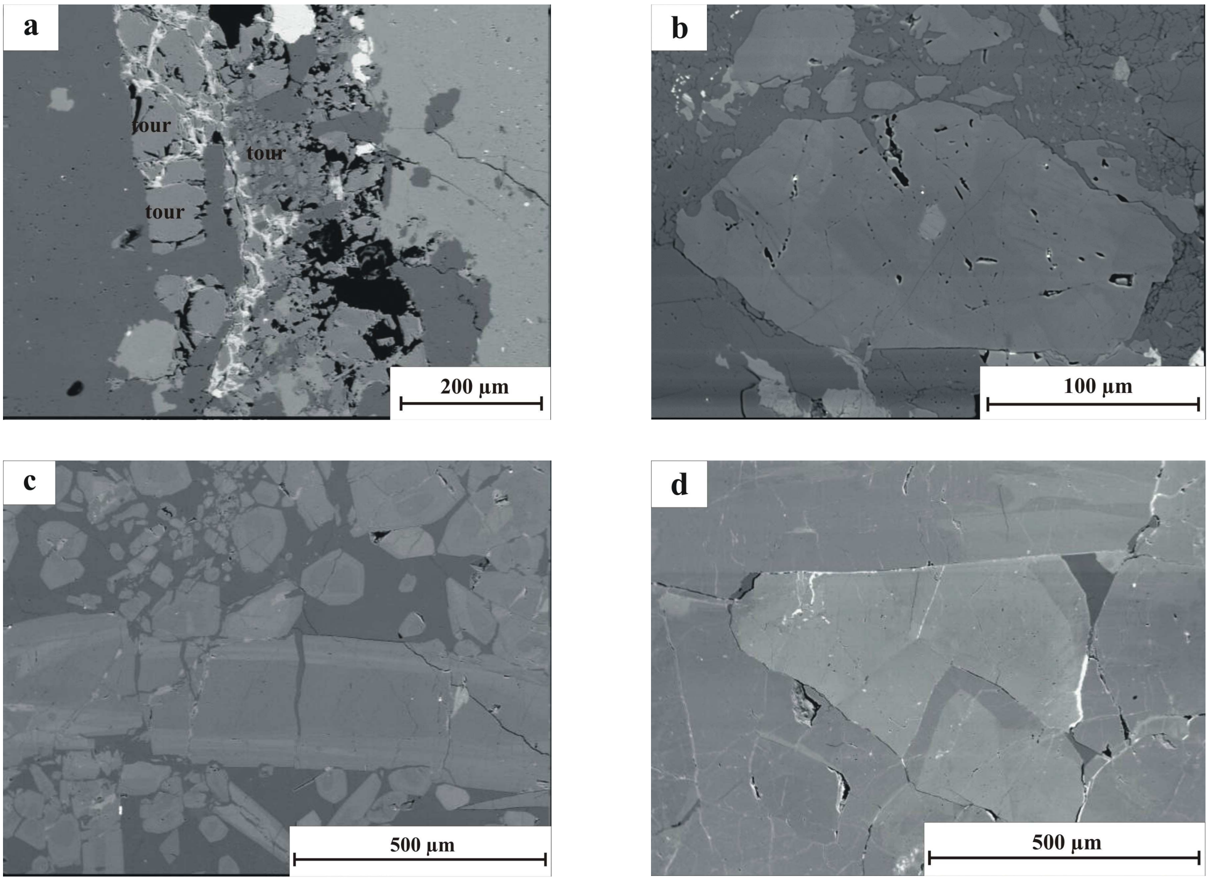

Fig. 3.23: BSE images of tourmaline samples from the Nezam Abad W ore deposit. In order to equally document chemical differences, all images have been taken at equivalent contrast and gray levels have not been changed as far as possible. Therefore, gray levels would reflect real chemical differences. a & b Unzoned tourmaline in aplite c & d Zoned tourmaline of hydrothermal vein.

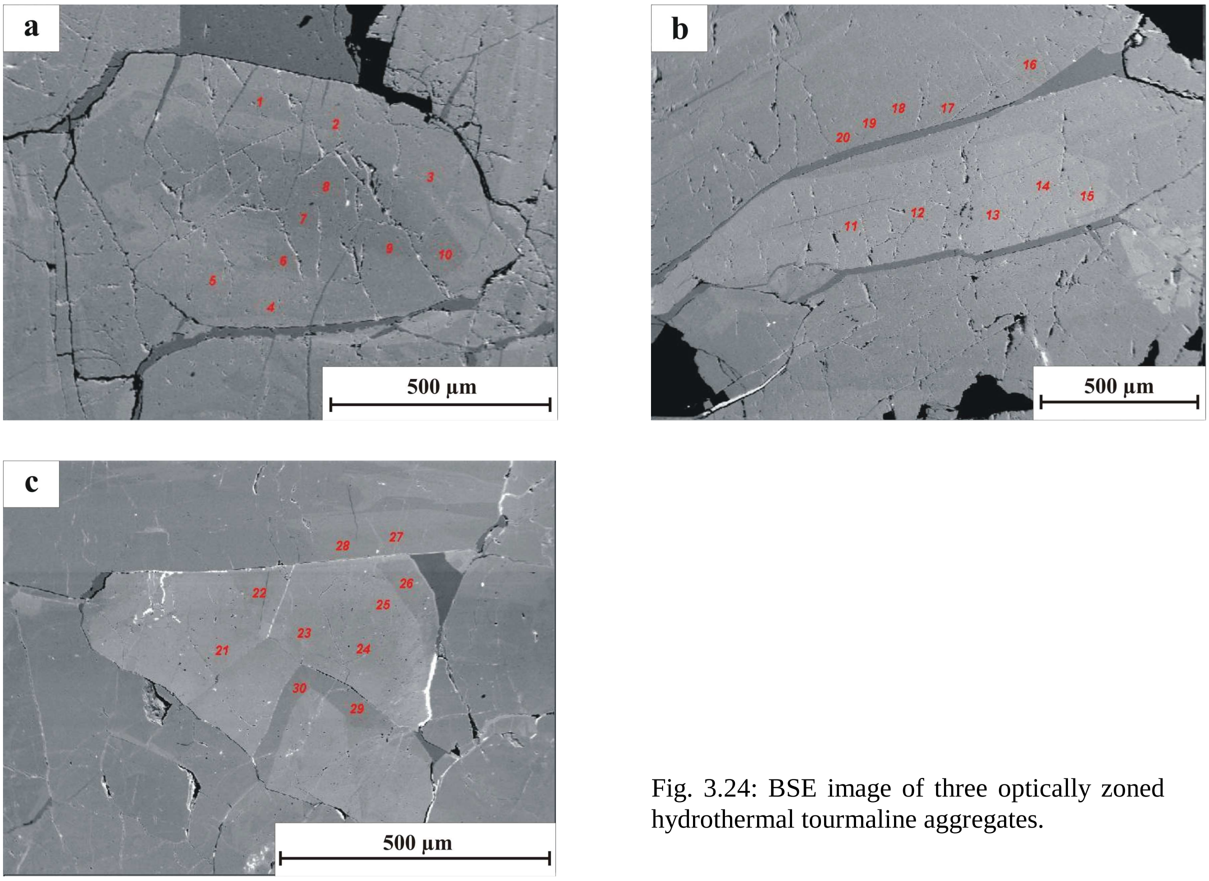

Fig. 3.24: BSE image of three optically zoned hydrothermal tourmaline aggregates.

Table. 3.5: Electron microprobe analysis of three zoned tourmaline grains of Figure 3.25.

	F	Na_2O	MgO	Al_2O_3	SiO_2	CaO	TiO_2	FeO	Cr_2O_3	MnO	Total	FeO/FeO+MgO
Sample/Point												
NZ25/1	bdl	1.63	7.73	32.45	36.10	1.85	0.65	7.13	0.01	0.06	87.61	0.48
NZ25/2	bdl	1.65	7.88	32.35	35.95	1.91	0.63	7.53	0.01	0.05	87.97	0.49
NZ25/3	bdl	1.67	7.69	32.72	35.93	1.79	0.60	7.34	0.02	0.04	87.89	0.49
NZ25/4	bdl	1.54	7.74	31.58	36.24	2.14	1.01	7.89	0.02	0.06	88.33	0.50
NZ25/5	bdl	1.56	7.63	31.60	35.99	2.13	1.06	8.16	0.02	0.04	88.23	0.52
NZ25/6	bdl	1.75	7.42	33.60	36.66	1.54	0.29	7.04	0.01	0.05	88.41	0.49
NZ25/7	bdl	1.68	7.11	34.28	36.93	1.05	0.04	6.50	0.01	0.04	87.69	0.48
NZ25/8	bdl	1.69	7.19	34.20	37.05	1.06	0.11	6.54	0.01	0.04	87.91	0.48
NZ25/9	bdl	1.61	6.97	34.24	36.87	1.05	0.11	6.64	0.03	0.04	87.62	0.48
NZ25/10	bdl	1.74	6.95	34.18	36.69	1.08	0.13	7.04	0.03	0.04	87.62	0.49
NZ25/11	bdl	1.16	7.73	31.15	35.96	2.92	0.78	7.99	0.02	0.05	87.88	0.50
NZ25/12	bdl	1.14	8.05	30.55	36.20	3.14	0.86	8.04	0.04	0.05	87.76	0.51
NZ25713	bdl	1.1	7.82	30.10	36.07	3.06	1.34	8.67	0.03	0.04	88.20	0.50
NZ25/14	bdl	1.15	7.85	30.35	35.68	2.89	1.52	8.68	0.03	0.06	88.24	0.53
NZ25/15	bdl	1.42	7.69	30.72	35.81	2.40	1.59	8.31	0.02	0.05	88.13	0.52
NZ25/19	bdl	1.59	7.42	32.76	36.42	1.87	0.37	7.67	0.01	0.04	88.23	0.52
NZ25/20	bdl	1.69	7.66	32.62	36.71	1.86	0.48	7.57	0.01	0.05	88.68	0.51
NZ25/21	bdl	1.16	8.15	30.64	36.22	3.03	0.90	8.09	0.05	0.04	88.42	0.50
NZ25/22	bdl	1.15	8.19	31.21	36.59	3.06	0.81	7.62	0.04	0.05	88.81	0.50
NZ25/23	bdl	1.26	7.76	30.99	35.98	2.74	0.75	8.24	0.03	0.05	87.85	0.48
NZ25/24	bdl	1.16	8.08	31.33	36.43	2.95	0.81	7.85	0.04	0.05	88.82	0.52
NZ25/25	bdl	1.18	8.09	31.02	36.36	3.01	0.78	8.05	0.03	0.04	88.68	0.49
NZ25/26	bdl	1.67	7.84	32.50	36.72	1.85	0.42	7.43	0.01	0.05	88.52	0.49
NZ25/27	bdl	1.48	7.71	31.75	36.19	2.20	0.88	7.73	0.03	0.05	88.10	0.50
NZ25/28	bdl	1.48	7.86	31.92	36.26	2.27	0.89	7.79	0.03	0.05	88.66	0.50
NZ25/29	bdl	1.62	8.04	31.93	36.13	2.01	0.48	7.26	0.03	0.04	87.53	0.47
NZ25/30	bdl	1.65	7.97	32.14	36.29	2.11	0.46	7.24	0.03	0.05	88.03	0.48
Average		**1.49**	**7.70**	**32.13**	**36.32**	**2.14**	**0.66**	**7.61**	**0.02**	**0.05**	**88.18**	**0.50**

3.4.3 Arsenopyrite

Arsenopyrite is an useful geochemical tool for geothermometry (Kretschmar & Scott 1976). Kretschmar (1976) provided comprehensive experimental data which enable arsenopyrite geothermometry (e.g. Fig. 3.26). Electron microprobe analysis was carried out on totally two arsenopyrite in two samples (Table 3.7 and 3.8). The association of arsenopyrite with pyrrhotite and löllingite is of particular importance in the studied samples. Referring to the obtained data and presented diagrams, a temperature in the range of 580-650^{o}C is deduced for the precipitation of early arsenopyrite in the Nezam Abad ore deposit. The range of temperature overlaps partly with the oxide stage of the mineral assemblage including W mineralization.

3.5 **Hydrothermal alteration**

Alteration in the study area is mineralogically not pronounced and confined mostly to the quartz-tourmaline veins and host rocks. Main alteration types are tourmalinization, propylitization (chloritization-silicification), sericitization and argillization (Figs. 3.27, 3.28)

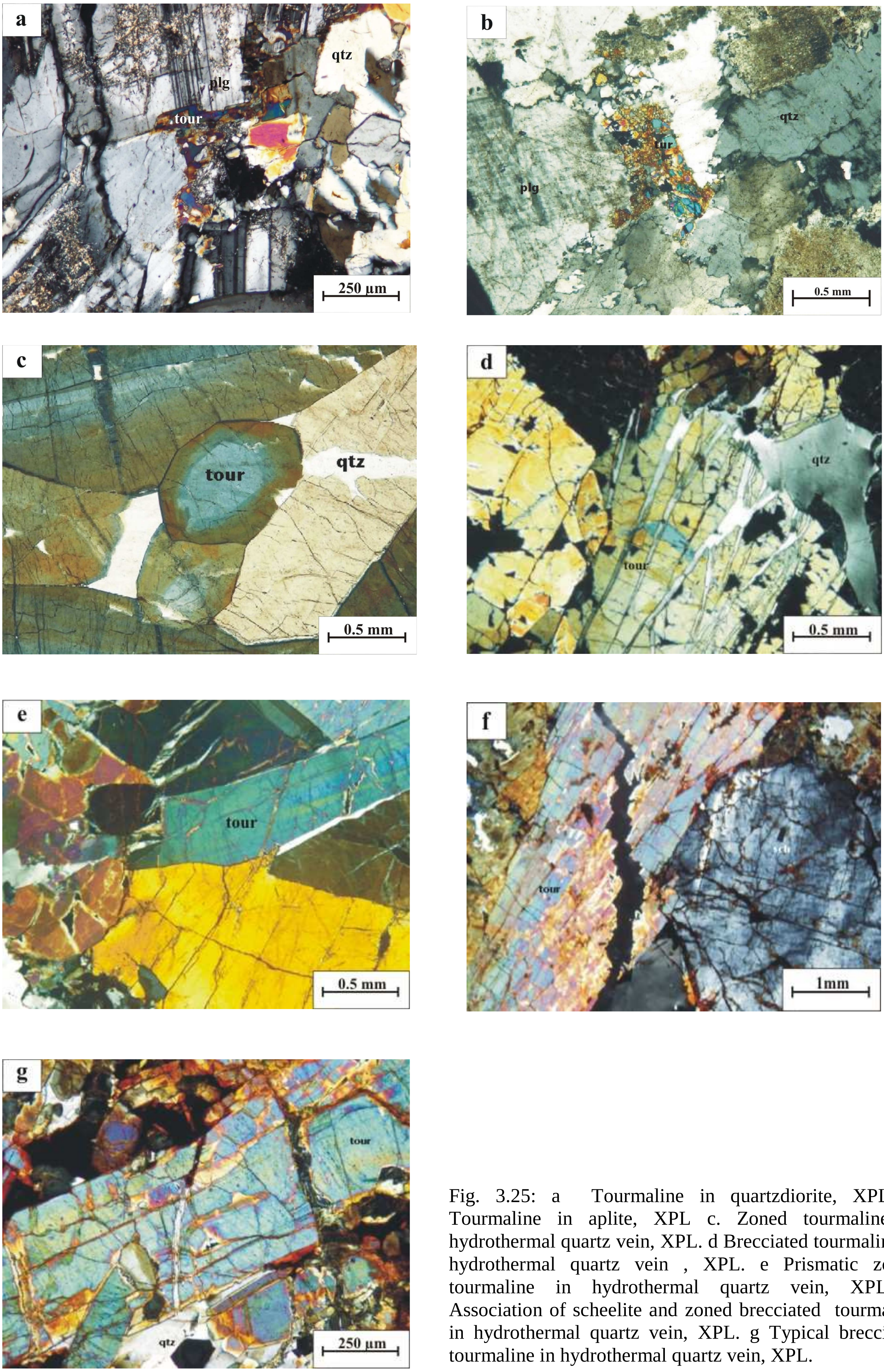

Fig. 3.25: a Tourmaline in quartzdiorite, XPL. b Tourmaline in aplite, XPL c. Zoned tourmaline in hydrothermal quartz vein, XPL. d Brecciated tourmaline in hydrothermal quartz vein , XPL. e Prismatic zoned tourmaline in hydrothermal quartz vein, XPL. f Association of scheelite and zoned brecciated tourmaline in hydrothermal quartz vein, XPL. g Typical brecciated tourmaline in hydrothermal quartz vein, XPL.

Table.3 .7: Electron microprobe analysis of arsenopyrite.

Sample	S	Fe	Te	As	Co	Ag	Au	Se	Sb	Bi	Total
NZ-36-2	wt%	wt%	ppm	wt%	wt%	ppm	ppm	ppm	ppm	ppm	wt%
1	17.0	31.8	< 360	51.0	< 85	110	< 50	<64	390	< 237	99.9
2	17.7	32.3	< 360	50.3	< 85	110	< 50	<64	260	< 237	100.3
3	17.2	32.0	< 360	50.5	< 85	110	< 50	<64	380	< 237	99.8
Mean	**17.3**	**32.0**	**< 360**	**50.6**		**110**			**343**		**100.0**
NZ-30											
1	17.9	32.0	< 360	49.8	< 85	100	< 50	<64	650	< 237	99.8
2	18.3	33.3	< 360	49.5	< 85	130	< 50	<64	380	< 237	101.2
3	18.6	33.4	< 360	49.3	< 85	100	< 50	<64	590	< 237	101.3
4	18.0	31.8	< 360	49.5	< 85	100	< 50	<64	860	< 237	99.4
5	18.3	32.9	< 360	49.2	< 85	130	< 50	<64	570	< 237	100.5
6	18.0	31.8	< 360	49.4	< 85	140	< 50	<64	1230	< 237	99.4
Mean	**18.2**	**32.5**		**49.5**		**117**			**713**		**100.3**

Table. 3.8: Electron microprobe analysis of arsenopyrite. Data are recalculated to 100%.

Sample	S	Fe	As	S	Fe	As	Total
NZ-36-2	wt%	wt%	wt%	at %	at%	at%	at%
1	17.0	31.8	51.0	29.9	31.9	38.2	100
2	17.7	32.3	50.3	30.8	32.0	37.2	100
3	17.2	32.0	50.5	30.2	32.1	37.8	100
Mean	**17.3**	**32.0**	**50.6**	**30.3**	**32.0**	**37.7**	**100**
NZ-30							
1	17.9	32.0	49.8	31.2	31.8	37.0	100
2	18.3	33.3	49.5	31.3	32.5	36.1	100
3	18.6	33.4	49.3	31.6	32.5	35.8	100
4	18.0	31.8	49.5	31.4	31.7	36.9	100
5	18.3	32.9	49.2	31.5	32.4	36.1	100
6	18.0	31.8	49.4	31.4	31.8	36.8	100
Mean	**18.2**	**32.5**	**49.5**	**31.4**	**32.1**	**36.5**	**100**

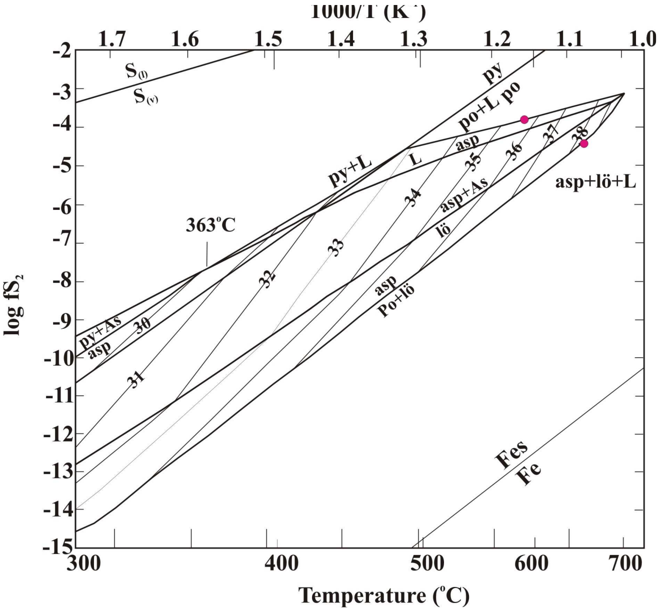

Fig. 3.26: Activity of S_2-temperature projection of buffered assemblages involving arsenopyrite in the Fe-As-S system, arsenopyrite stability field is shaded (after Kretschmar & Scott 1976). The studied arsenopyrites are cogenetic with löllingite and pyrrhotite.

Generally, the intensity of alteration increases towards the mineralized veins through alteration of plagioclase to saussurite, sericite, and clay minerals, alkali feldspar to sericite and clay minerals and biotite to chlorite. Furthermore, quartz and tourmaline increase remarkably, while in fresh quartzdiorite tourmaline is very rare and the amount of quartz is in the normal range.

Tourmalinization is the most pervasive alteration type in the Nezam Abad mining area. Tourmaline occurs very rare in fresh quartzdiorite, but is abundant in the altered quartzdiorite, aplite and near and inside hydrothermal veins. Tourmalinization preceded and overlapped with the main phase of mineralization and continued to late stage.

Sericitization is manifested by the assemblage of sericite, pyrite and quartz. It is more obvious in thin sections of both igneous host and vein materials as alteration product of plagioclase and alkali feldspar (Fig. 3.28).

Propylitization is typified ideally with the assemblage of carbonate-epidote-quartz-chlorite. In the study area, chlorite and quartz and rarly carbonates and epidote characterize this kind of alteration. Chloritization and carbonatization occur mostly in outer parts of the alteration halo and form dominant gangue minerals of the sulfidic stage of paragenetic sequence, while silicification has taken place in the inner parts (Fig. 3.28).

Argillization is evident by the development of clay minerals through alteration of plagioclase and alkali feldspar. It shows two different assemblages. The first one with dickite, metahalloysite, halloysite and kaolinite represents the less and the second one with dickite, propylite, and kaolinite reflects the more advanced argillization. XRD analysis by Shamanian (1994) showed that the second assemblage is associated with quartz and tourmaline in the Nezam Abad ore deposit. In the study area, all alteration types overlap and no typical hydrothermal zonation can be outlined.

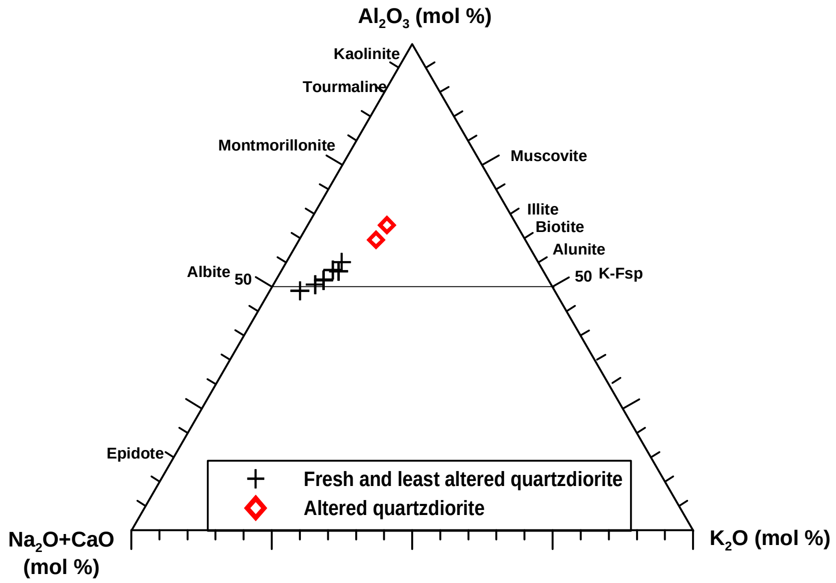

Fig. 3.27: Al_2O_3-(Na_2O+CaO)-K_2O triangular diagram showing the least-altered and altered intrusive rocks in the Nezam Abad ore deposit.

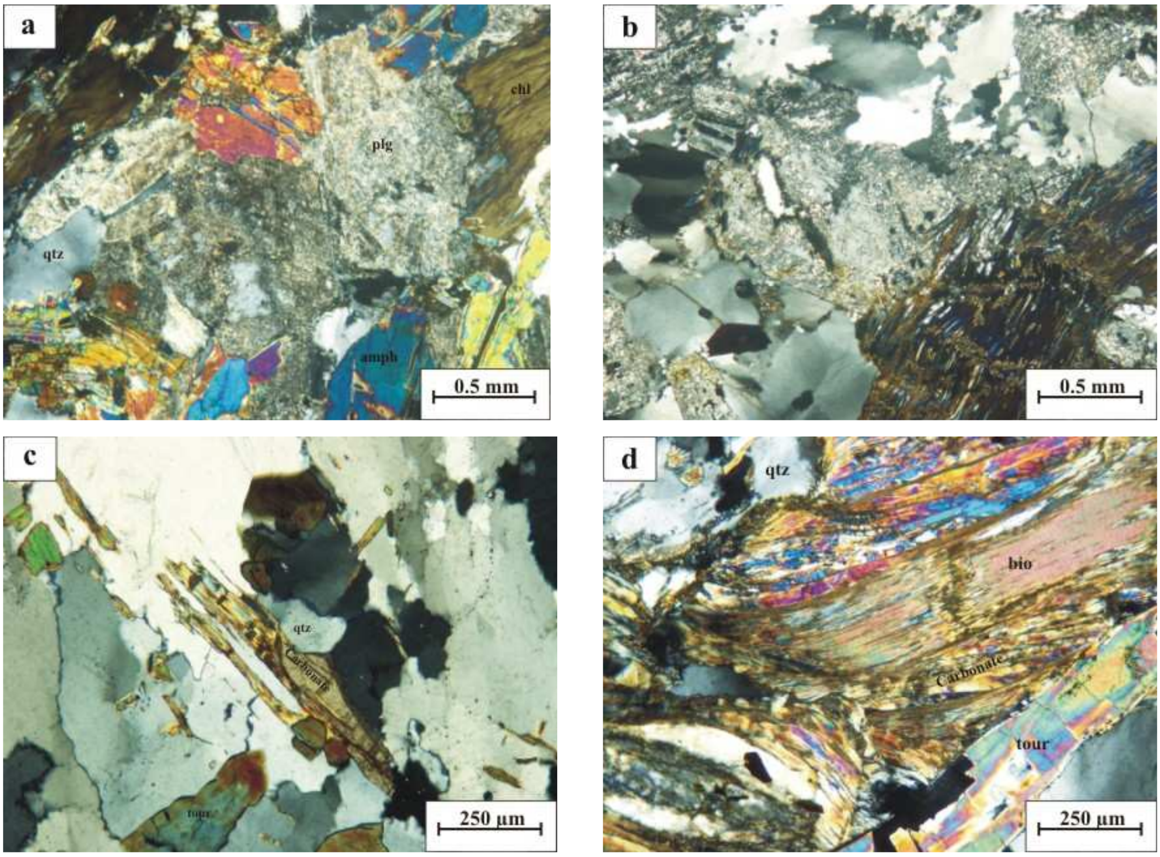

Fig. 3.28: a Alteration of biotite and plagioclase to chlorite and clay minerals, respectively, XPL. b Argillization and chloritization of alkali feldspar and biotite, respectively, XPL. c & d Tourmalinization, carbonatization and biotitization, XPL. e Chloritization, XPL.

3.6 **Geochemistry of the ore deposit**

Host rocks and ores have been assayed during several exploration projects, particularly by Geological Survey of Iran. In this study, 12 samples of fresh and less altered quartzdiorite and aplite were analyzed (Appendix 1). Farhadian et al. (1993) reported average values of trace elements in a total of 145 altered host rock samples of the Nezam Abad mining area (Table 3.9). These data show strong enrichment of As and Bi and slight enrichment of Cu, Ag, and W comparing to upper and bulk continental crust. The quartzdioritic unit of the Nezam Abad complex is a less evolved metaluminous phase with no clear relation to the mineralization. On the contrary, the W-Sn-(Au) mineralization in the Nezam Abad ore deposit is associated with aplite and quartz-tourmaline veins which may represents a highly fractionated magma (Figs.2.7 to 2.10). Extensive sampling has been carried out by Geological Survey of Iran from tunnels, trenches and boreholes. In this research, 19 samples from ore-bearing quartz-tourmaline veins of the accessible parts of the tunnels were collected and analyzed (Table 3.10).

Nezafati (2006), reported amount of invisible Au up to 580 ppm in arsenopyrite, 460 ppm in covellite, 800 ppm in pyrrhotite, 1360 ppm in schneiderhönite, and 340 ppm in bismuth minerals. Farhadian (1993) reported also contents of up to 3.37 % W, 0.87 % Sn, 2.9 % As, 0.3 ppm Au, 22 ppm Ag, 548 ppm Bi and 4.72 % Cu for mineralized quartz-tourmaline veins.

Table. 3.9: Mean value of trace elements in 145 samples of the Nezam Abad quartzdiorite (after Farhadian 1993).

Cu	Zn	As	Pb	Ag	Sn	W	Au	Hg	Bi
ppm	ppm	ppm	ppm	ppm	ppm	ppm	ppm	ppm	ppm
118	65	64.00	12.98	0.09	3	5	1	0.03	1.31

3.7 **Oxygen isotope data**

In order to constrain the source of fluids, the $\delta^{18}O$ values of 5 quartz samples of both mineralized and barren hydrothermal quartz-tourmaline veins were determined (Table. 3.11). These values show the range of 11.9-13.8 ‰ (X= 13.1±0.7 %), excluding seawater and meteroric water as the sources of hydrothermal fluids. On the contrary, the high $\delta^{18}O$ signature corresponds to metamorphic or magmatic rocks.

Table 3.10: Trace element data of 19 ore samples of the Nezam Abad mining area.
All samples belong to the mineralized quartz-tourmaline veins.

	Au ppb INAA	Ag ppm ICP	As ppm INAA	Cu ppm ICP	Mo ppm ICP	Pb ppm ICP	Sb ppm INAA	Sn % INAA	W ppm INAA	Zn ppm ICP
Sample										
NZ-1	79	12	9810	>10000	2	17	<0.1	<0.01	2720	361
NZ-2	126	23	4130	>10000	<1	31	<0.1	<0.01	980	233
NZ-3	<2	27	2880	>10000	1	15	<0.1	<0.01	74	54
NZ-4	153	7	12800	9540	3	8	<0.1	<0.01	413	82
NZ-5	<2	3	1570	6560	2	15	<0.1	<0.01	446	135
NZ-6	<2	2	227	695	1	14	0.50	<0.01	89	111
NZ-7	150	10	11300	>10000	2	28	<0.1	<0.01	1350	194
NZ-8	428	5	653	>10000	3	35	6	<0.01	95	136
NZ-9	51	6	405	>10000	1	23	<0.1	<0.01	<1	275
NZ-11	<2	1	1560	862	<1	<3	12.8	<0.01	1180	152
NZ-12	<2	<0.3	56	115	<1	<3	<0.1	<0.01	454	52
NZ-13	<2	<0.3	29	105	2	<3	0.4	<0.01	234	47
NZ-15	<2	<0.3	108	9610	3	10	2	<0.01	10	185
NZ-29	54	<0.3	140	1260	<1	<3	<0.1	<0.01	60	115
NZ-31	<2	<0.3	77	45	<1	<3	<0.1	<0.01	3	36
NZ-33	80	15	1100	>10000	2	50	7.2	<0.01	381	343
NZ-38	100	11	3500	8740	1	14	<0.1	<0.01	1720	68
NZ-39	<2	1	186	4460	2	5	1.6	<0.01	3120	79
NZ-40	<2	3	493	4200	2	4	<0.1	<0.01	8370	84

Table 3.11: $\delta^{18}O$ values of quartz samples, Nezam Abad ore deposit.

Sample	$\delta^{18}O$ (‰)	Remark
NZ-12	13.6	Mineralized quartz-tourmaline vein
NZ-13	13.3	Mineralized quartz-tourmaline vein
NZ-35	13.1	Barren quartz-tourmaline vein
NZ-36	13.8	Mineralized quartz-tourmaline vein
RV-6	11.9	Barren quartz-tourmaline vein, Revesht tunnel

Nezafati (2006) reported the value of $\delta^{34}S$ in arsenopyrite (4 ‰) and arsenopyrite-pyrite (1.2 ‰), (avg. +2.6‰, two samples) indicating a relative narrow range near zero. The Nezam Abad ore deposit is an vein type W-Sn-Au mineralization, hosted by the ilmenite-series, metaluminous, felsic, calc-alkaline and I-type quartzdioritic units of the Nezam Abad complex. The $\delta^{34}S$ values in the range -3 to 1‰ indicate magmatic sulfur (Field and Gustafson 1976, Shelton and Rye 1982, Hoefs 2004). The sulphur in hydrothermal system of Nezam Abad is derived from igneous sources, either from silicate melts or leaching of igneous rocks.

Chapter 4

4. Astaneh Au prospect

4.1 Introduction

The gold deposits and occurrences of Iran are shown in Fig. 4.1. Most of the recognized gold ore deposits/prospects in Iran are rather small in size and a few of them have been studied and described so far. A majority of the gold deposits/prospects are epithermal and located within the Tertiary Urumieh-Dokhtar, Alborz, and East Iranian magmatic belts (Fig. 4.1). These include for example the Zarreh Shuran Au-As ore deposit in the Azarbaidjan province, hosted by the Miocene sedimentary rocks with 2.5 million metric tons (Mt) at 10 g/t of gold (Mehrabi et al. 1999), the Agh Darreh Au prospect hosted by the Oligo-Miocene carbonate rocks (Momen Zadeh et al. 1995, Nekouvaght Tak, 1997) with 50 t Au at grades of 3-4 g/t gold and the volcanic rock-hosted Gandy and Abolhasani prospects in the Alborz magmatic arc, Semnan province (Shamanian et al. 2004).

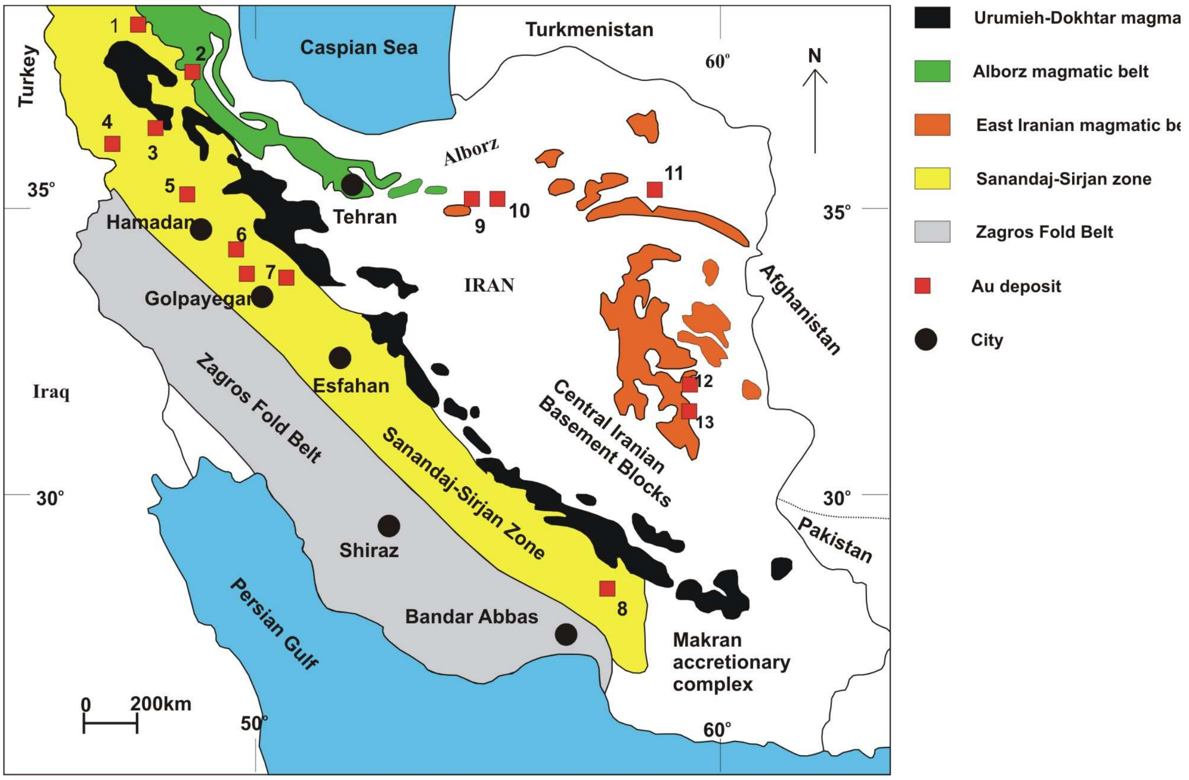

Fig. 4.1: Main tectonic units (after Stöcklin 1968, Alavi et al. 1997) and location of gold deposits/prospects in Iran (modified from Moritz et al. 2006).

1- Kharvana 2- Mianeh 3- Zarshuran-Agh Darreh 4- Kervian 5- Dashkasan-Baharlu 6- Ahangaran 7- Astaneh 8- Zartorosht 9- Gandy 10- Kuh-e-Zar 11- Chelpow 12- Qal'eh Zari 13- Shalir 14- Muteh

In the Sanandaj-Sirjan zone, the gold ore deposits/prospects have been distributed mostly in the northern parts. Typical examples are Muteh gold mine hosted predominantly by schist and gneiss and subsidiary amphibolite and quartzite (Moritz et al. 2006) with a total tonnage of 1.79 Mt at a grade of 2.85 g/t at Chah Khaton open pit and of 1.76 Mt at a grade of 2.57 g/t at Senjedeh open pit (Moritz et al. 2006), the Sari Gunay epithermal gold deposit in the Kordestan province, hosted by Tertiary mildly alkaline latitic to trachytic volcanic complex (Richards et al. 2006) with 14 Mt at a gold grade of 1.9 g/t, Kervian Au deposit, hosted by acidic and basic mylonitized metavolcanic rocks (Heidari et al. 2006) with a reported reserve of 17t till 2003 at a grade of 3 g/t gold and ore deposits/prospects of the Astaneh-Nezam Abad area. In the southern part of the Sanandaj-Sirjan zone, the typical known occurrence is Zartorosht, hosted by Paleozoic metamorphic rocks with a reserve of about 36675 t for ore bodies with more than 1 ppm gold, and 45748 t at a grade of 400-1000 ppb gold (Moghaddam, 1993).

The Astaneh Au prospect is located 3 km west-southwest of the town of Astaneh (33°50´-33°52´ N, 49°17´-49°20´ W). Mineralization occurs in the northern part of the Astaneh intrusion and is hosted mostly by the Shirmazd Mountain. Au has been known for the local people for centuries and extracted by panning of alluvial deposits in the surrounding rivers. The old exploration activities can also be traced in the hard rocks, i.e. Shirmazd Mountain as some tunnels and open pits. Recent exploration activities have been done by private and governmental institutions, specifically Geological Survey of Iran during the last 40 years.

4.2 **Geology of the prospect**

Geology of the prospect includes the Astaneh intrusive body, hornfels and microgranitic rocks of the Shirmazd Mountain (Fig. 4.2).

- **Astaneh intrusion**: The Astaneh intrusion is mainly granodioritic in composition, but in the prospect area biotite granite dominates and local variations such as andalusite and tourmaline granites can be seen, as well.

Abundant barren aplite dikes and quartz veins cut the intrusion. Xenoliths of variable composition are common, particularly near the eastern margin (Fig. 4.3). A Rb-Sr age determination by Masoudi (1997) gave 98.9 ± 1.0 Ma for the Astaneh intrusion.

At the flank of the Ghorogh Dar Mountain, a small part of the Astaneh intrusion is highly altered, producing a low relief hill called, Tappeh Khieleh (Fig. 4.4). In hand specimen and at microscopic scale, most of the minerals have been altered to sericite, clay minerals, chlorite and Fe compounds (Figs. 4.5, 4.6).

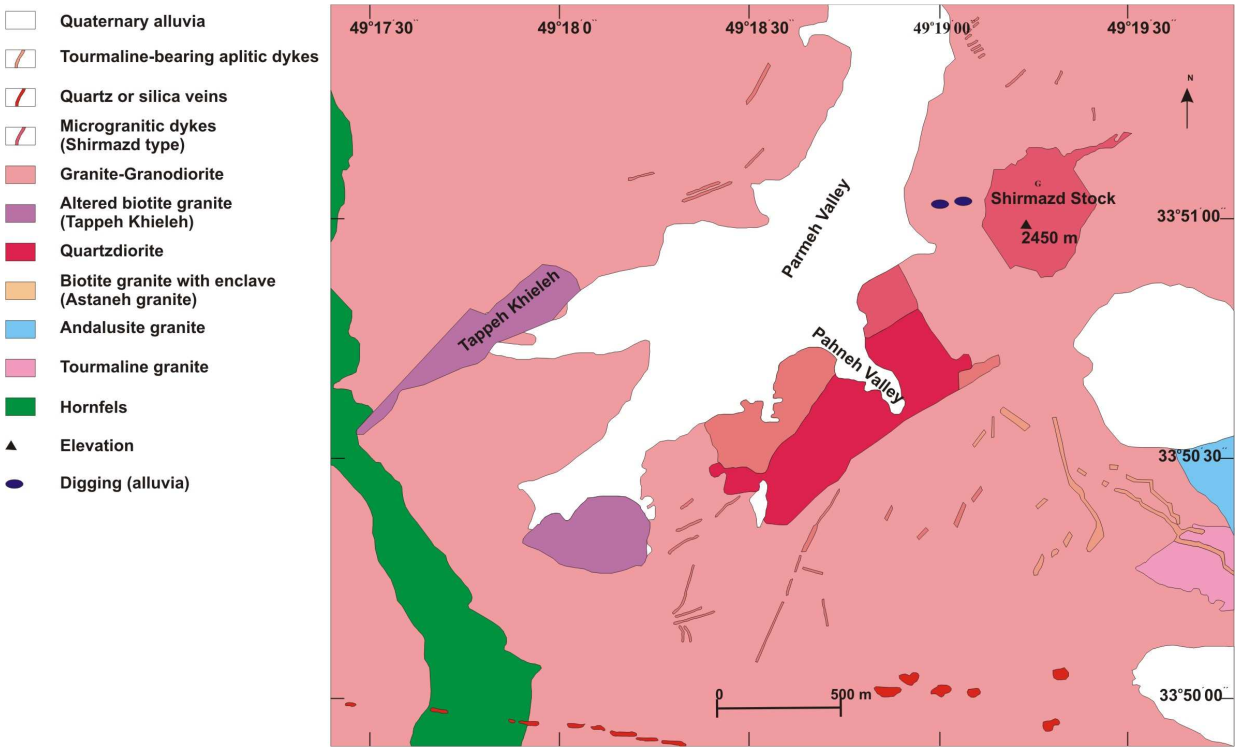

Fig. 4.2: Geological map of the Astaneh Au prospect (modified from Ojaghi et al. 2001).

- **Tourmaline granite**: Tourmaline granite is a common unit of the Astaneh intrusion and is exposed about 1200 m southeast of the Shirmazd Mountain. Tourmaline occurs as disseminated acicular crystals with diameters up to 10 cm in size.

- **Andalusite granite**: In the southeastern part of the Shirmazd Mountain, the Astaneh intrusion is characterized by localy high amounts of andalusite.

- **Shirmazd Mountain**: The dome-like Shirmazd Mountain is mostly made up of micrograngite and intrudes the Astaneh intrusion (Figs. 4.7, 4.8). The petrographical and geochemical characteristics of these rocks were discussed in the chapter two. The texture of the rocks is mostly microgranular, and subordinate porphyry. The main minerals are quartz, feldspar, plagioclase and minor biotite. These rocks are the host of the Au mineralization and have been considered as the source of placer Au in the surrounding rivers. Abundant silica and aplitic veins cut the micrognanitic rocks of the Shirmazd Mountain. Rb-Sr and Sm-Nd isotope analysis of the micrograntic rocks of the Shirmazd Mountain reveal a distinctly different origin compared to the main Astaneh biotite granite and the Nezam Abad quartzdiorite intrusions (Fig. 2.21). Isotope age determination by Rb-Sr method on bulk rock has yielded an isochron of 35.1±0.9 Ma for the Au-bearing microgranites of the Shirmazd Mountain (Nezafati et al. 2005).

4.3 **Alteration**

Alteration zones in the prospect area are are confined mainly to the Shirmazd Mountain with sericitization, chloritization, silicification and carbonatization. Argillization can be determined only at microscopic scale.

- Sericitization: This is the most common and pervasive alteration in the study area, resulting from decomposition of plagioclase and alkali feldspar (Fig. 4.9a).
- Chloritization: Alteration of biotite and to a lesser extent amphibole to chlorite is also very common after sericitization, particularly in microgranites of the Shirmazd Mountain.(Fig. 4.9b). Chlorite occurs along the mineralized quartz veins, as well.
- Silicification: Silisification is manifested by quartz vein, veinlets and together with sericitization show good correlation with mineralization (Fig. 4.9c).
- Carbonatization: Calcite occurs very rarely together with chlorite (Fig. 4.9d).

Figure 4.10 shows the effect of alteration on the microgranite of the Shirmazd Mountain in comparison to the Astaneh intrusion. The trend of alteration toward sericitization in the microgranitic host rocks of the Shirmazd Mountain is conspicuous.

4.4 **Mineralization**

Mineralization occurs in veins/veinlets and as dissemination. NW-SE trending veins include quartz, quartz-sulfide and sulfide (arsenopyrite) and are evident mainly in the north and northwestern part of the Shirmazd Mountain (Fig. 4.11). Veins are up to 50 cm wide and 2-30 m long.

4.5 **Ore mineralogy**

- Sulfides:

1- **Chalcopyrite:** Chalcopyrite is very common and occurs as dissemination in the host rocks and as vein mineral together with quartz. It has been mostly oxidized to goethite, occurring as small brownish rims in hand specimen (Figs. 4.11 b,d). At microscopic scale, chalcopyrite is associated with pyrite, sphalerite, bornite and arsenopyrite. Covellite is a weathering product of chalcopyrite (Fig. 4.12). Of particular interest, is the presence of skeletal sphalerite inclusions (Fig. 4.12a). According to Ramdohr (1969) sphalerite stars in chalcopyrite usually indicates exsolution or high-temperature unmixing processes. Hutchison and Scott (1980) suggested that this unmixing occurs at a temperature of about 400^{o}C.

Fig. 4.3: Microquartzdioritic xenoliths in the Astaneh intrusion.

Fig. 4.4: Astaneh intrusion with Ghorogh Dar hornfels.

Fig. 4.5: Strongly altered biotite granite of the Tappeh Khieleh.

Fig. 4.6: Sericitization, chloritization and argillization of the Astaneh biotite granite in the Tappeh Khieleh, XPL.

Fig. 4.7: Shirmazd Mountain, host of Au mineralization.

Fig. 4.8: Hand specimen of the Au-bearing microgranite, Shirmazd Mountain.

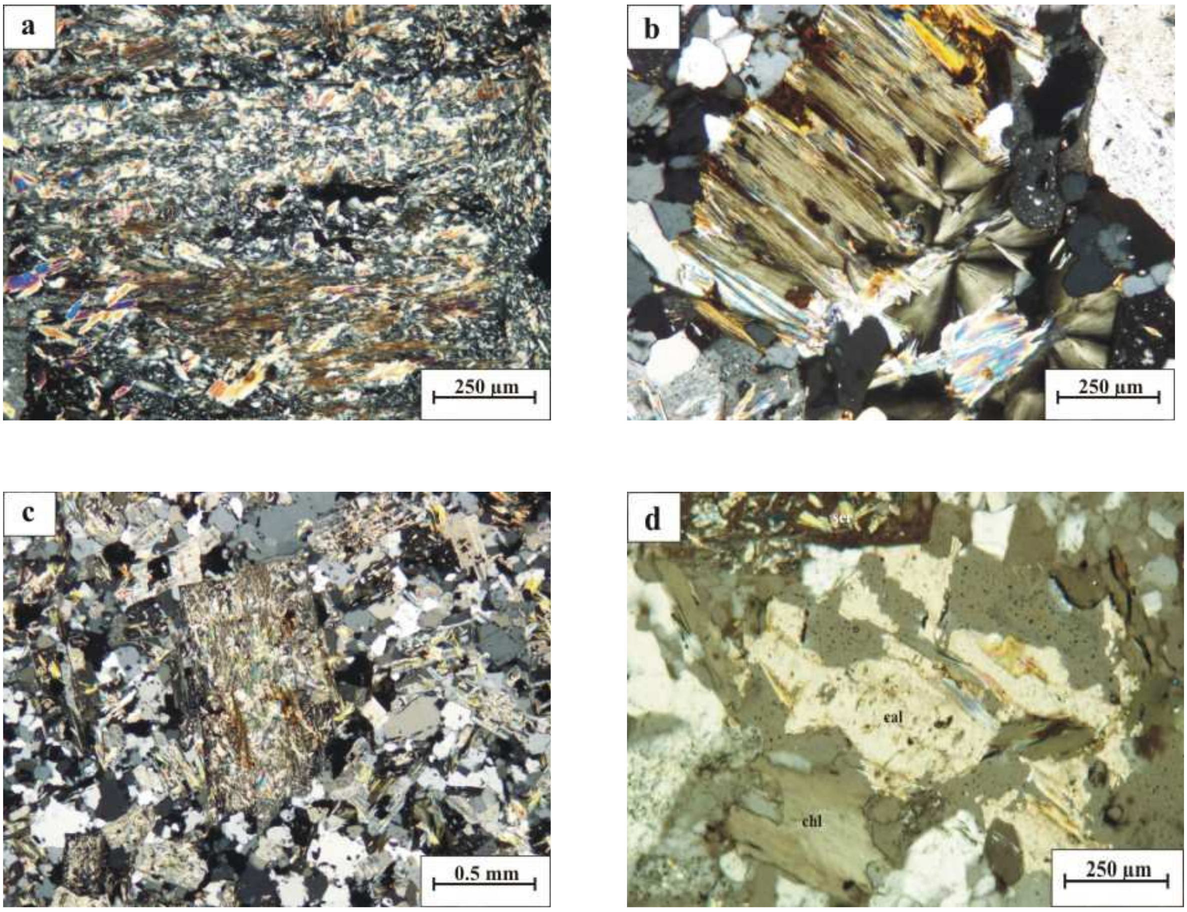

Fig. 4.9: Various types of alteration in micrograntes of the Shirmazd Mountain. a Sericitization, XPL. b Chloritization, XPL. c Silicification & sericitization, XPL. d Carbonatization & chloritization, XPL.

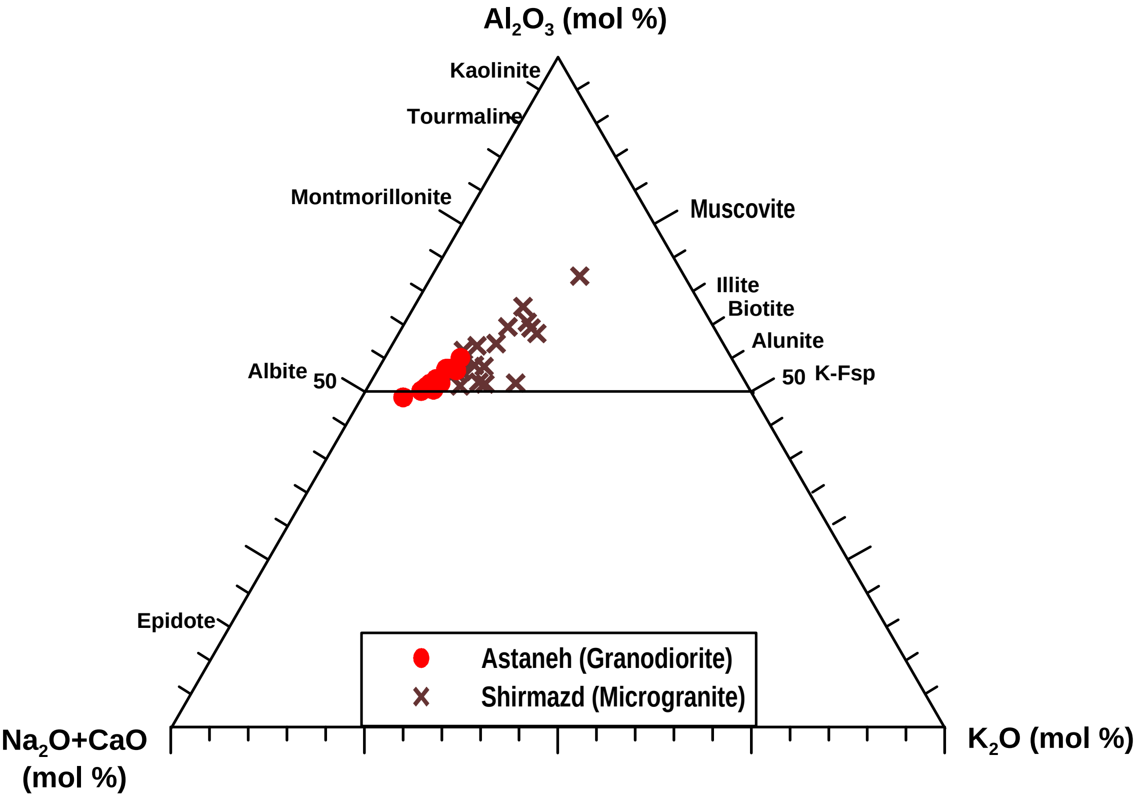

Fig. 4.10: Al_2O_3-(Na_2O+CaO)-K_2O triangular diagram showing the least-altered and altered rocks of the Astaneh Au prospect.

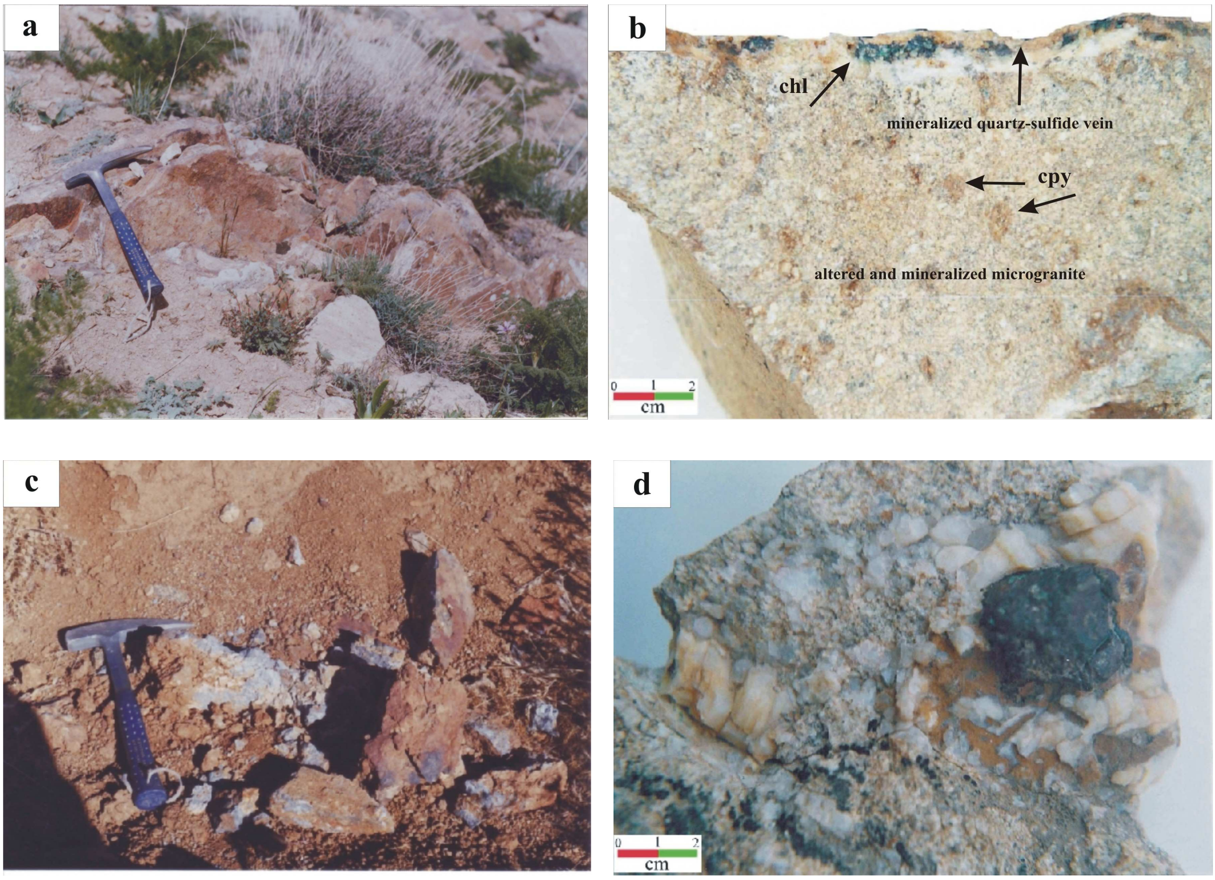

Fig. 4.11: Different types of mineralization in the Astaneh prospect. a Silica vein. b Quartz-sulfide vein. c Sulfide vein (arsenopyrite). d Open space-filling mineralization, chalcopyrite is coated by geothite.

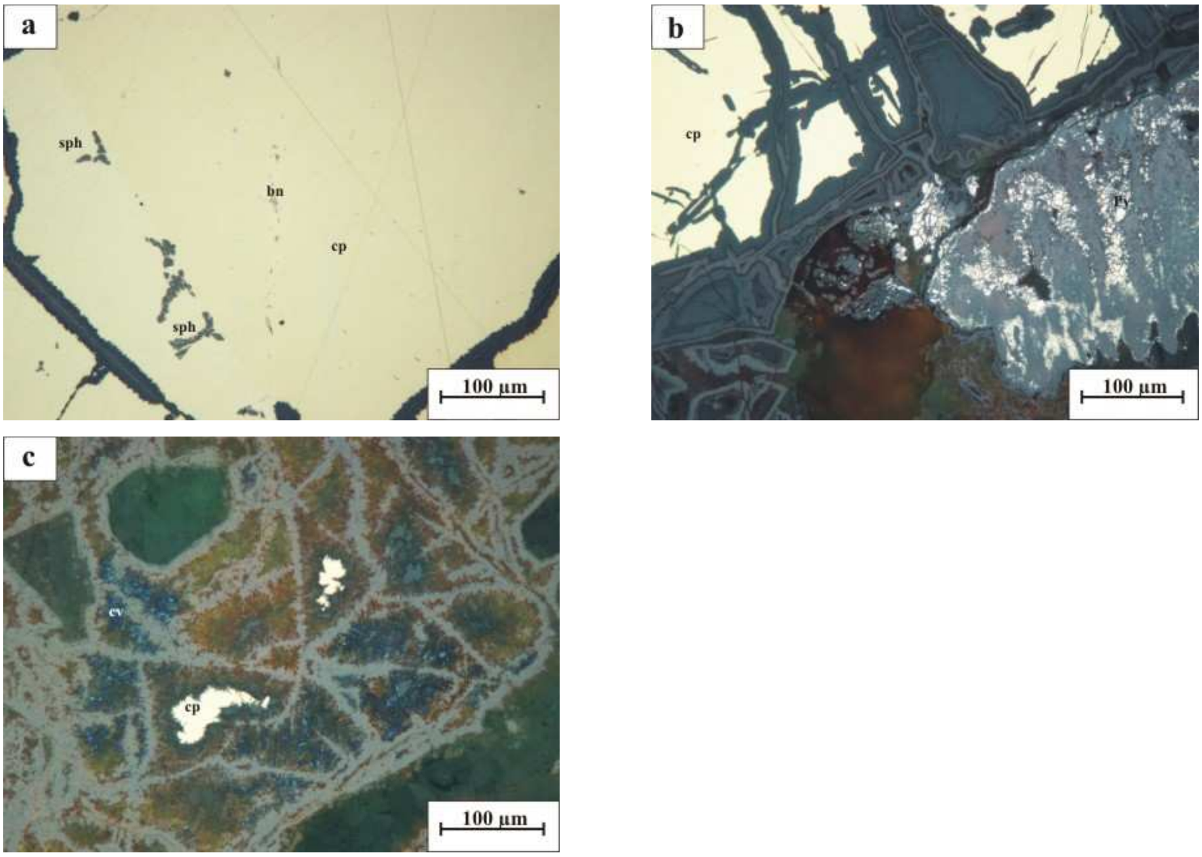

Fig. 4.12: a Chalcopyrite with star-like sphalerite and bornite inside, oil immersion, PPL. b Chalcopyrite with fragmented pyrite, oil immersion, PPL. c Alteration of chalcopyrite to covellite, oil immersion, PPL.

Marignac (1989) believes that sphalerite stars result from local supersaturation in sphalerite at growing fronts of chalcopyrite, including the epitaxic nucleation of skeletal sphalerite which is subsequently trapped in the growing chalcopyrite host.

2- **Pyrite**: Pyrite is ubiquitous in this prospect. It it associated with chalcopyrite. The euhedral to subhedral pyrite grains show mostly cataclastic texture. Pyrite can be seen in quartz-sulfide vein and dissemination in the host rock. Alteration of pyrite to Fe-oxides is common (Fig. 4.13).

3- **Arsenopyrite**: Arsenopyrite is common as well. It occurs mostly as massive monomineral veins (Fig. 4.11c). Due to early formation, cataclastic texture is vivid. It is partly associated with chalcopyrite (Fig. 4.14). Replacement of arsenopyrite by scorodite can be seen.

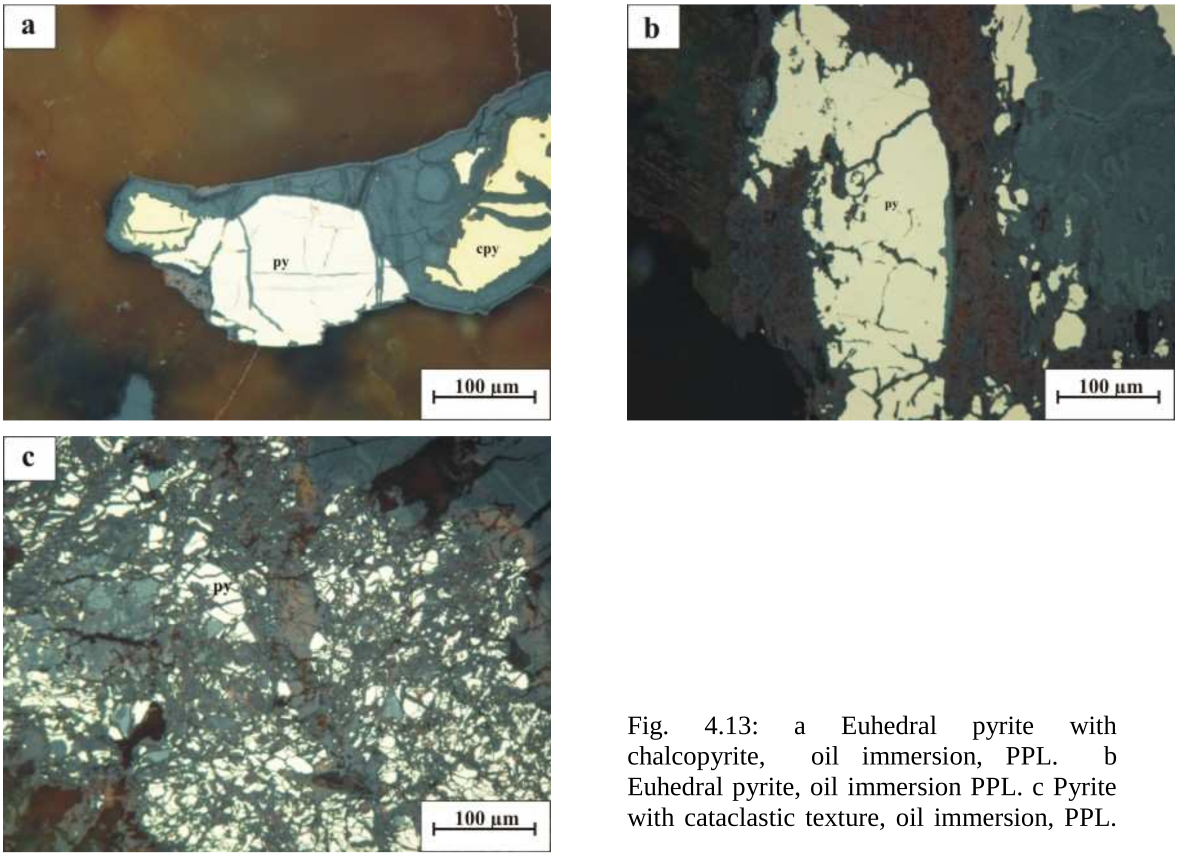

Fig. 4.13: a Euhedral pyrite with chalcopyrite, oil immersion, PPL. b Euhedral pyrite, oil immersion PPL. c Pyrite with cataclastic texture, oil immersion, PPL.

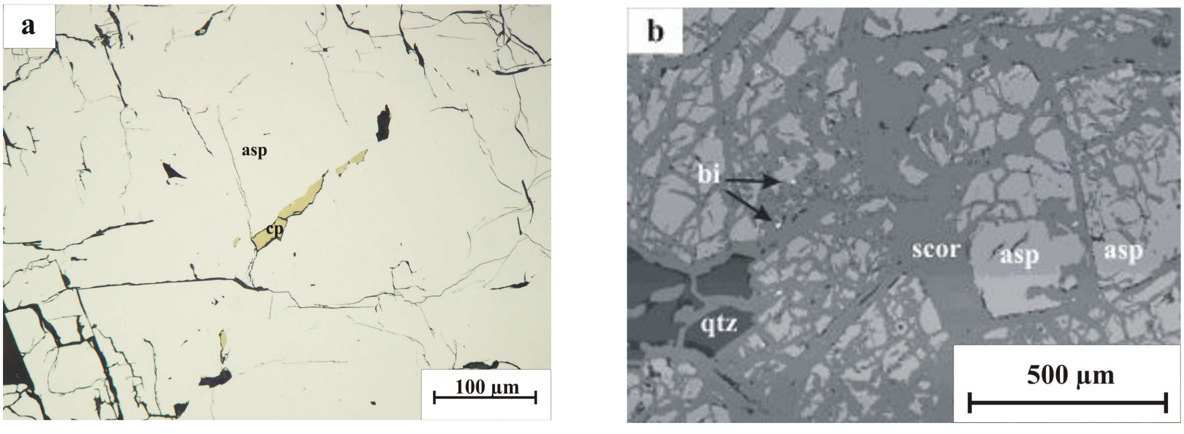

Fig. 4.14: a Arsenopyrite with chalcopyrite on fractures, oil immersion, PPL. b BSE image of arsenopyrite, illustrating inclusions of native bi.

Electron microprobe analysis of arsenopyrite (Table 4.1) shows presence of Ag, Sb and Se up to 130 ppm and 1560 ppm in, respectively.

Table. 4.1: Electron microprobe analysis of arsenopyrite, Astaneh Au prospect.

Sample	**S**	**Fe**	**Te**	**As**	**Co**	**Ag**	**Au**	**Se**	**Sb**	**Bi**	**Total**
AS-35	wt%	wt%	ppm	wt%	ppm	ppm	ppm	ppm	ppm	wt%	wt%
1	20.00	34.69	< 350	48.43	< 40	110	< 48	120	1090	< 240	103.25
2	19.56	34.49	< 350	49.08	< 40	113	< 48	130	400	< 240	103.20
3	20.09	34.55	< 350	48.43	< 40	113	< 48	90	360	< 240	103.14
4	19.74	34.54	< 350	48.36	< 40	110	< 48	110	240	< 240	102.70
5	19.66	34.91	< 350	48.63	< 40	110	< 48	100	310	< 240	103.26
6	19.82	34.59	< 350	48.62	< 40	110	< 48	100	170	< 240	103.08
7	20.39	34.78	< 350	47.73	< 40	130	< 48	70	1560	< 240	103.06
Mean	19.89	**34.65**		**48.47**		**114**		**102.9**	**590**		**103.10**

4- **Pyrrhotite**: Pyrrhotite occurs very rarely as open-space filling in subhedral to anhedral grains (Fig. 4.15).

5- **Sphalerite**: It occurs as star-like crystals inside chalcopyrite (Fig. 4.12a) and massive individual grains in quartz-sulfide veins (Fig. 4.16).

6- **Bornite:** Bornite occurs very rarely and only in chalcopyrite (Fig. 4.12a).

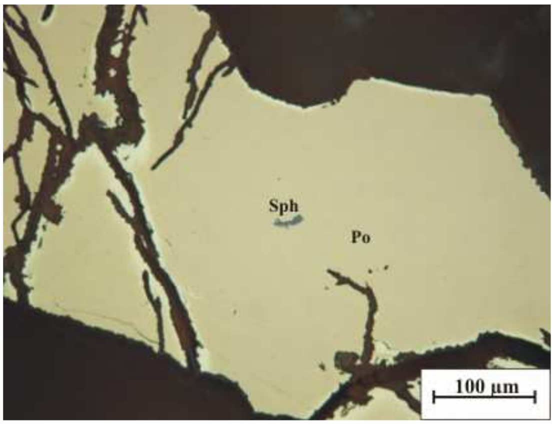

Fig. 4.15: Pyrrhotite, oil immersion, PPL.

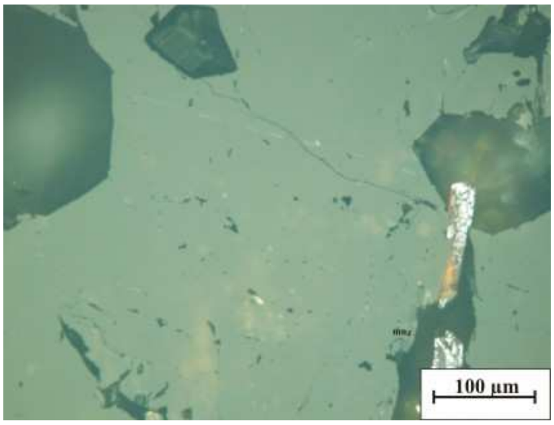

Fig. 4.16: Sphalerite, oil immersion, PPL.

- **Oxides**:

1- **Ilmenite and rutile**: These are very common, occurring mostly as needle and skeleton-like grains in quartz-sulfide veins and host rocks (Fig. 4.17a). Replacement of ilmenite to rutile has been observed (Fig. 4.17b).

2- **Covellite**: Covellite occurs as supergene ore mineral after chalcopyrite (Fig. 4.12c).

- **Phosphates:**

Monazite: Monazite was detected for the first time in the mineralized micrographic rocks of the Shirmazd Mountain (Fig. 4.18). Electron microprobe analysis revealed its type as cerium

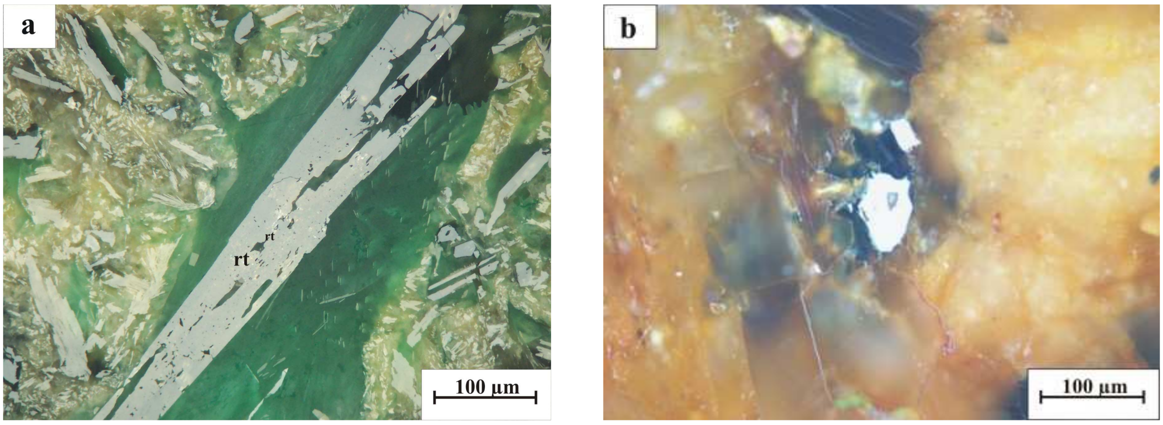

Fig. 4.17: a Needle-like rutile, oil immersion, PPL. b Ilmenite, oil immersion, PPL.

monazite (Table 4.2). Hydrthermal monazite can be distinguished from igneous monazite by its ThO_2 content which is 3-5 wt% in igneous monazite (Schandl & Gorton 2004).

The studied monazite is likely of hydrothermal origin. The low Th concentration in hydrothermal monazite is due to the low solubility of Th^{4+} (a high field strength element) compared to the $LREE^{3+}$ during hydrothermal activity, in hydrothermal fluids (Schandl & Gorton 2004).

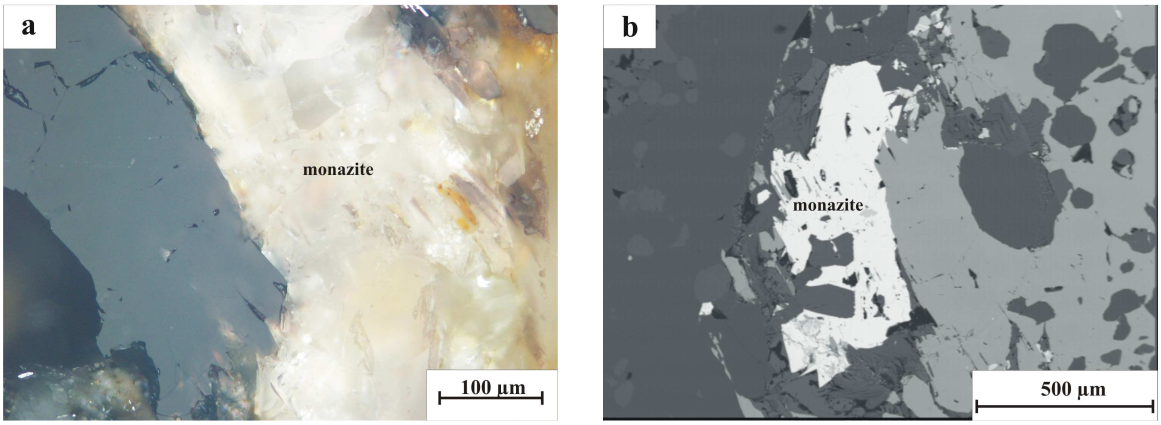

Fig. 4.18: a Monazite in microgranite, oil immersion, XPL. b BSE image of monazite.

Table. 4.2: Electron microprobe analysis of monazite.

Sample AS-1	**Pb** wt%	**Th** wt%	**U** wt%	**P** wt%	**Ce** wt%	**La** wt%	**Nd** wt%	**Pr** wt%	**O** wt%	**Total**
1	0.08	0.17	bdl	13	30	15	6	7	26	97.25
2	0.00	0.55	bdl	13	30	15	6	7	26	97.55
3	0.07	0.05	bdl	13	30	15	6	7	26	97.12
4	0.06	0.25	bdl	13	30	15	6	7	26	97.31
Mean	**0.053**	**0.255**		**13**	**30**	**15**	**6**	**7**	**26**	**97.31**

bdl: below detection limit. Detection limit for U is 100ppm.

- **Native elements**:

- **Au**: Au occurs as free visible grains in alluvial deposits. At microscopic scale, free Au grains are detected next to malachite, chlorite and sericitized plagioclase (Fig. 4.19). Based on semiquantitative electron microprobe analysis, the amount of Ag in Au grains exceeds 15 %.

- **Secondary minerals**: Covellite, malachite, azurite, Fe-oxides, tenorite and scorodite are weathering products of the sulfides in the studied samples.

4.6 **Paragenetic sequence**

The paragenetic sequence in the Astaneh prospect can be divided into the early, main and weathering stages (Fig. 4.20).

Early stage: This stage is indicated by minerals comprising monazite, rutile, ilmenite and quartz with no direct relation to Au mineralization.

Main stage: Continuation of quartz formation along with more sericitization and precipitation of the main sulfides such as chalcopyrite, sphalerite, arsenopyrite, pyrrhotite and pyrite.

Weathering stage: Secondary minerals like Fe-oxides, covellite, scorodite as well as supergene gold represent this stage.

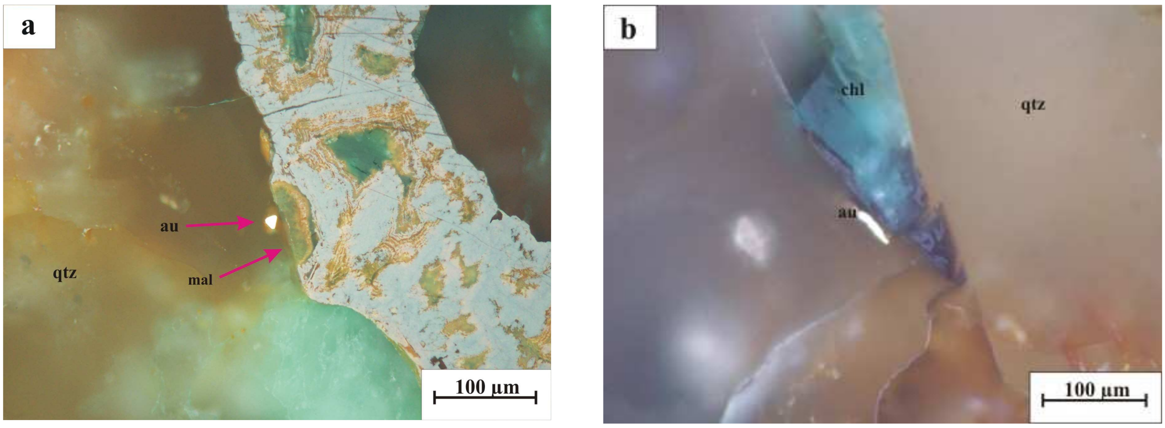

Fig. 4.19: a & b. Free gold grain in the microgranite of the Shirmazd Mountain, PPL.

4.7 **Geochemistry**

Several samples from the mineralized rocks and veins of the Shirmazd Mountain were analyzed for major and trace elements (Appendixes 1, 2).

Overall, the Astaneh Au prospect has a low amount of sulfides and Au is the only possible economic element. Amount of gold reaches up to 7.2 ppm in arsenic veins and remains lower than 2 ppm in quartz and quartz-sulfide veins and less than 0.5 ppm in microgranite of the Shirmazd Mountain (Appendix 3).

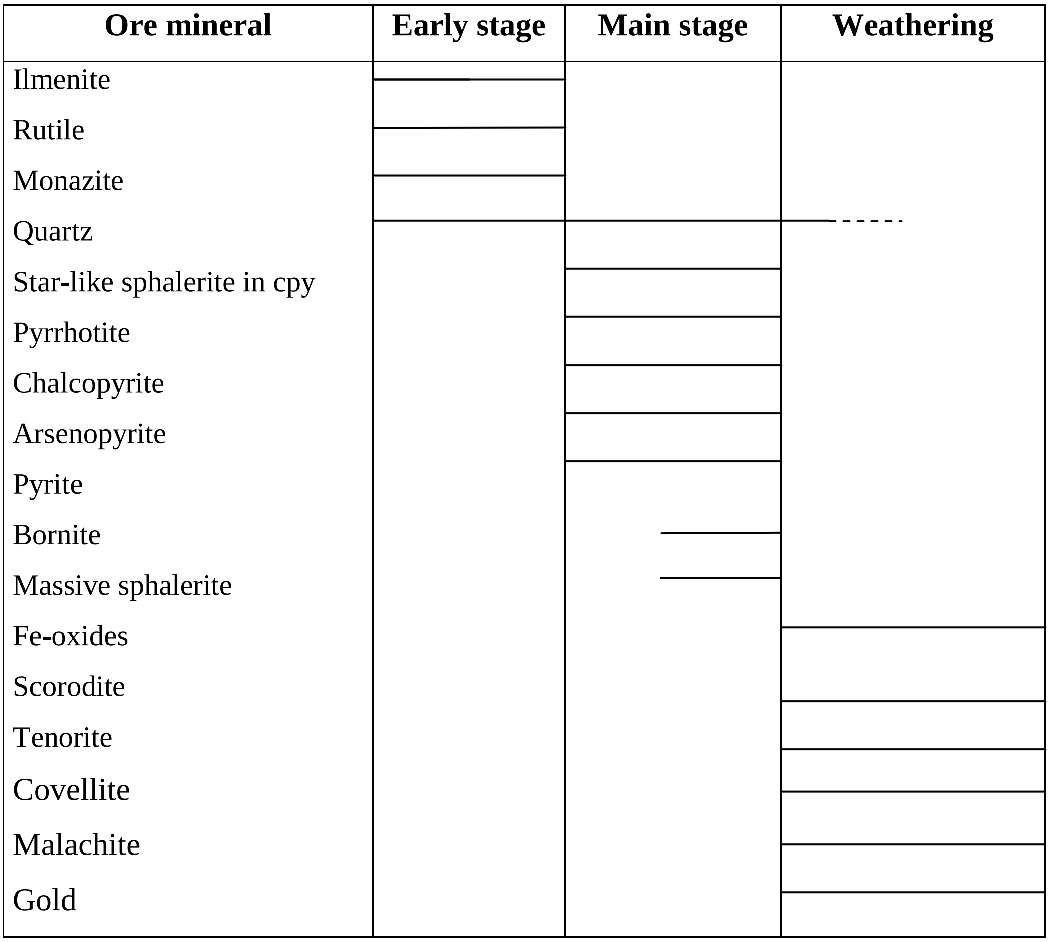

Fig. 4.20: Paragenetic sequence of the Astaneh Au prospect.

The average amount of Au in alluvial deposits exceeds 0.12 ppm and the size of Au grains reaches up to 1000 microns with an average of about 320 micron (Kowsari 2004). According to Samin Resources (2002), Au with up to 9 ppm in the primary ore shows good correlation with arsenopyrite. Samin Resources (2002) have also estimated 36 t of gold for the Shirmazd Mountain with an average grade of 0.4 ppm. As and Cu show partly high anomalies as well (Appendix 4). Electron microprobe analysis identified native Bi inclusions and confirmed presence of Sb, Se and Ag, as well (Table. 4.1).

4.8 **Isotope data**

4.8.1 **Sulfur**

In order to constrain the source of S in sulfides, two samples of arsenopyrite and chalcopyrite of the main stage mineralization were analyzed (Table 4.3). The $\delta^{34}S$ values of both minerals show a rather narrow range near zero. The Astaneh Au mineralization is associated with ilmenite-series, metaluminous, felsic, calc-alkaline and I-type microgranite of the Shirmazd Mountain. It has been documented that the $\delta^{34}S$ values of -3 to 1‰ indicate magmatic sulfur (Field and Gustafson 1976, Shelton and Rye 1982, Hoefs 2004). The sulphur in hydrothermal system is probably derived from igneous sources either from silicate melts or leaching of igneous rocks.

Table. 4.3: The δ^{34}S values of ore minerals, Astaneh Au prospect

Sample	Ore mineral	δ^{34}S ‰	Remark
AS-35	Arsenopyrite	-0.7	Massive arsenopyrite vein with up to 7 ppm Au
AS-82	Chalcopyrite	0.4	Disseminated chalcopyrite in altered micrograniite

4.8.2 Oxygen

Three quartz samples of mineralized quartz-sulfide veins of the Shirmazd Mountain were analyzed for their δ^{18}O composition (Table 4.4). The data show narrow range from 11.5 to 13.3 ‰ (mean= 12.3±0.9 ‰; 1σ). These data are within range of the data for Nezam Abad and exclude a meteoric or seawater fluid. Conversly, a magmatic or magmatic-metamorphic origin can be considered for hydrothermal fluids in Astaneh.

Table. 4.4: δ^{18}O results of quartz samples, Astaneh Au prospect.

Sample	δ_{18}O (‰)	Remark
AS-26	11.5	Quartz-sulfide vein, Shirmazd Mountain
AS-62	13.3	Quartz-sulfide vein, Shirmazd Mountain
AS-72	12.2	Quartz-sulfide vein, Shirmazd Mountain

Chapter 5

5. Deh Hossein Sn-Au-Cu prospect

5.1 **Introduction**

The Deh Hossein prospect is located, 13 km south of the town of Astaneh and north-northeast of the village of Deh Hossein (33° 45´-33° 47´ N, 49° 17´-49° 20´ E) (Fig 2.1).

The Deh Hossein ancient mining district has been recently explored and is the first known tin prospect in west-central Iran. Ancient mining activities are indicated by diggings and waste dumps together with stone mauls, mills and pottery shards. The old workings are up to 200 by 50 by 15 meters and up to 15 m deep as numerous big ellipsoidal waste dumps, in two rows along the mineralized structures (Fig 5.1). Due to overburden and soil cover, only the waste dumps and weakly mineralized selvages of the mineralized veins are accessible.

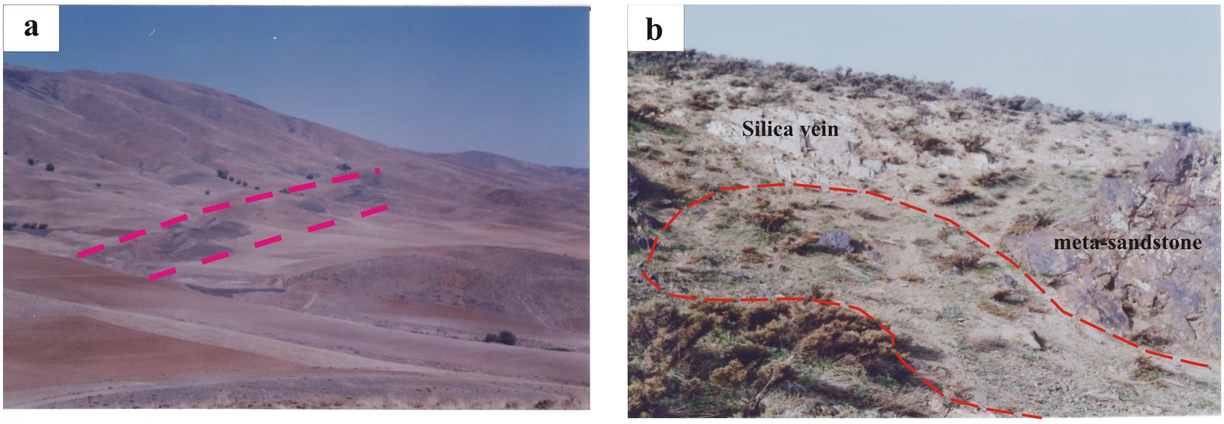

Fig. 5.1: a View of the Deh Hossein area showing the mineralized structures. b Mineralized silica vein next to the depression created by ancient workings.

5.2 **Geology of the prospect**

The country rocks comprise phyllite, spotted slate and schist of Jurassic age with metavolcanic and meta-sandstone interbeddings. These rocks have undergone low-grade greenschist metamorphism and are intruded by the Astaneh intrusion in the northeastern part of the prospect (Fig. 5.2). The spotted slate has a fine lamination with NW-SE trend and contains mostly quartz, micaceous minerals and accessory minerals such as zircon, monazite, apatite, and pyrite. Schist and phyllite show schistosity with NW-SE trend and are light gray to dark green in color. Hornfels and small patches of tourmaline granite of the Astaneh intrusion are exposed in the northeastern part of the prospect. Meta-sandstone with partly

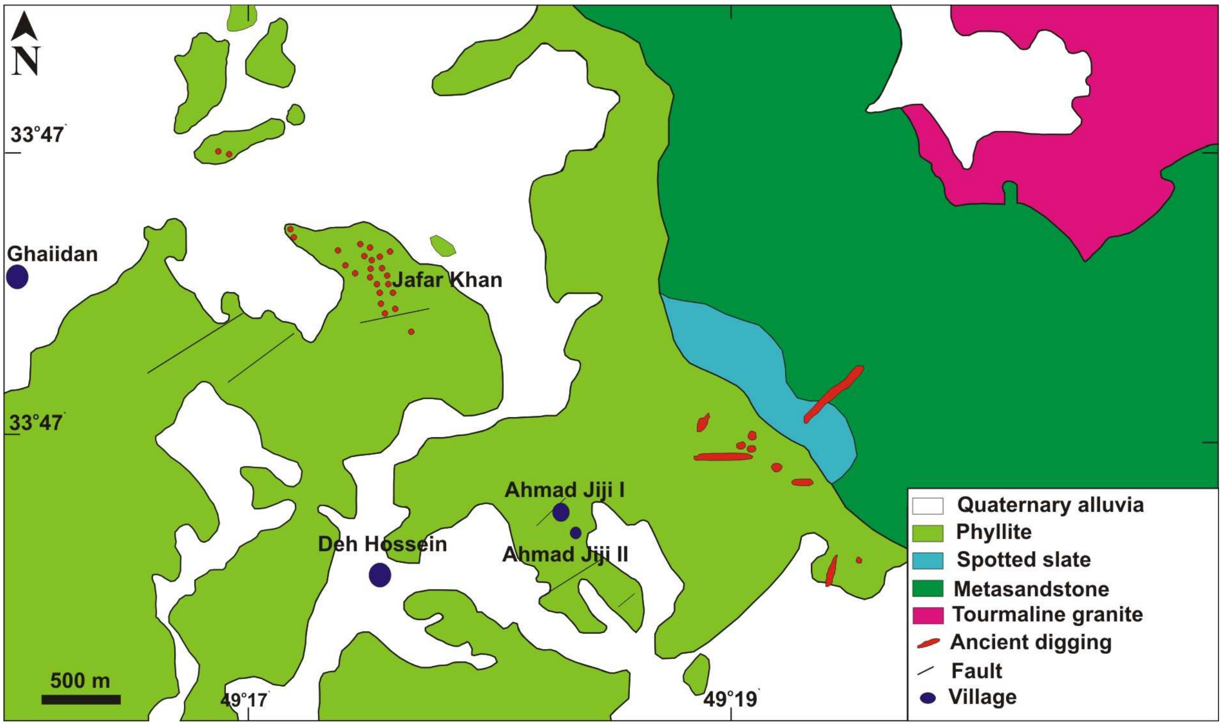

Fig. 5.2 Geology of the Deh Hossein prospect (modified from Ojaghi et al. 2001).

laminated texture is mostly made up of quartz and micaceous minerals in addition to accessory minerals including zircon, apatite, monazite and pyrite (Fig. 5.3).

5.3 **Alteration**

Alteration is not extensive and confined mostly to veins and veinlets. Alteration types in the meta-sedimentary rocks include sericitization, silicification, chloritization and to a lesser extent tourmalinization and monazitization. The first three types occur in igneous rocks of the study area as well, while the last one is confined mainly to the meta-sedimentary rocks and shows P metasomatism(Fig. 5.4).

- Sericitization: This is the dominant alteration type in the prospect and indicated by the conversion of fine-grained micaceous minerals to fine grained white mica, i.e. sericite.
- Silicification: Intensity of silicification is quite different from fully replacement of the original rocks by massive cryptocrystalline quartz to veins and veinlets of quartz and finally open space filling automorph crystals.
- Chloritization: Chlorite surrounds mostly quartz grains in meta-sandstone.
- Tourmalinization: This type is characterized by scattered patches and veinlets of tourmaline in the meta-sedimentary rocks and together with quartz in mineralized quartz-sulfide veins.
- Monazitization: It occurs sparsely in altered meta-sedimentary rocks and vein selvages.

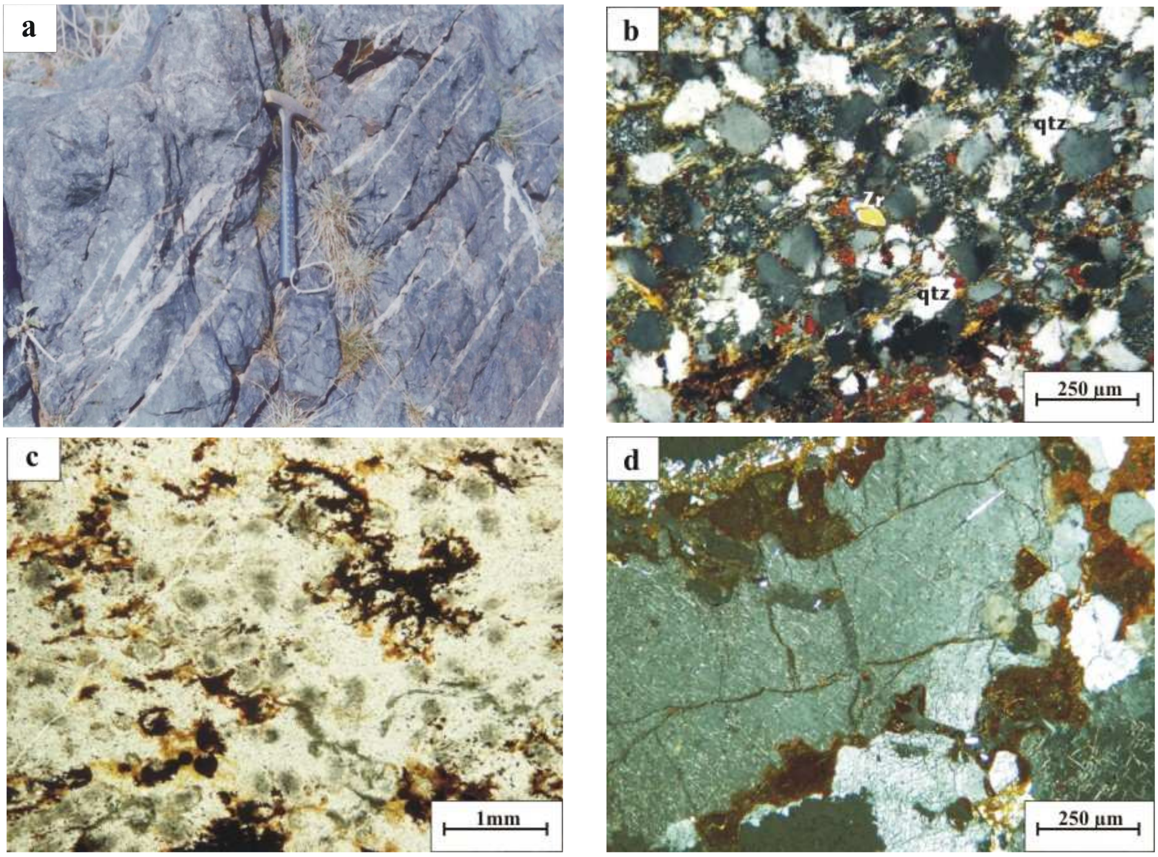

Fig. 5.3: a Meta-sandstone with sheeted quartz veins. b Photomicrograph of the same rock. Recrystallized quartz grains in fine-grain-ed quartz and chlorite. Zircon grain with yellow color in the center of the photo is vivid, XPL.c Spotted slate, PPL. d Big crystal of cordierite in meta-pelite, XPL.

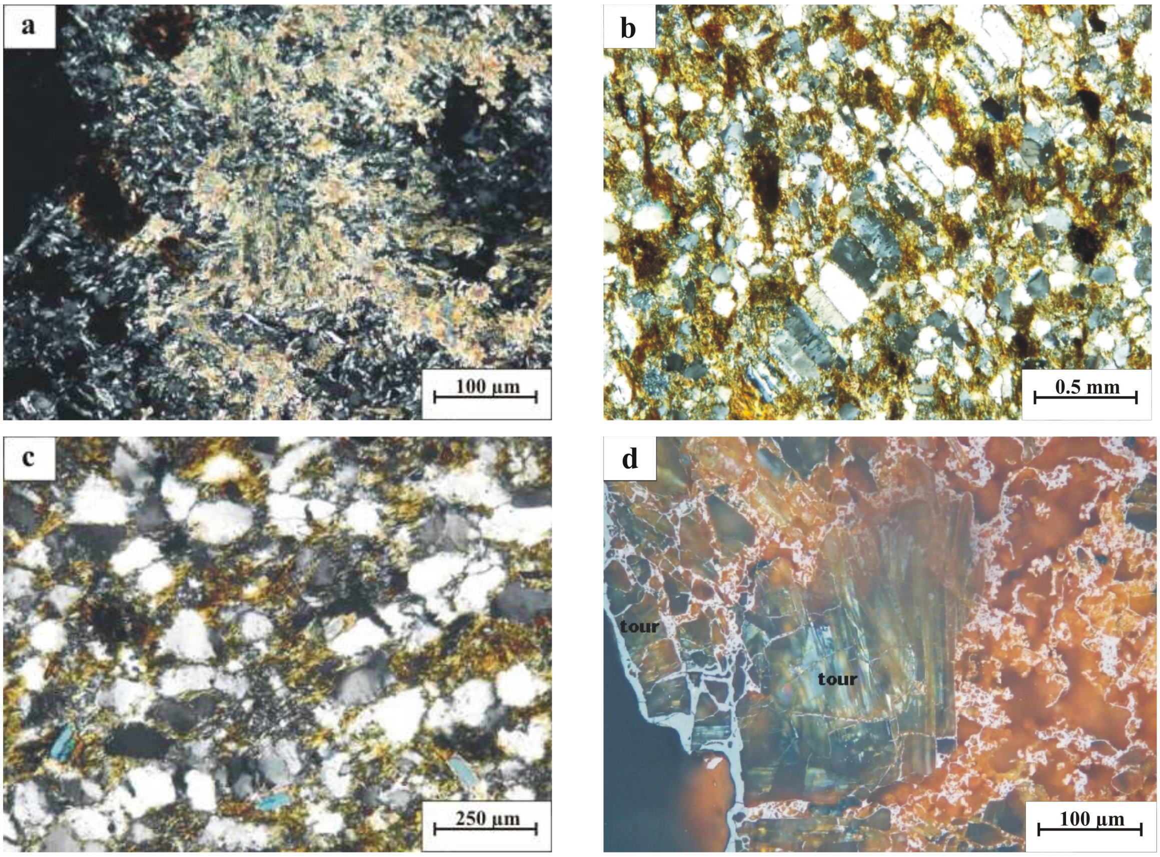

Fig. 5.4: Different kinds of alteration in meta-sedimentary host rocks of the Deh Hossein prospect. a Phyllite with high sericitization, XPL. b Silicification in slate, XPL. c Chloritization surrounds recrystallized quartz grains in meta-sandstone. Opaque and micaceous minerals are distributed, XPL. d Tourmalinization, oil immersion, PPL.

5.4 **Mineralization**

Mineralization is characterized by quartz-sulfide veins and their gossans in Jurassic meta-sedimentary rocks (Fig. 5.5). The mineralized veins with partly sheeted structure trend mostly NW-SE, corresponding to the main faults of the area. The veins are commonly subvertical with up to 1.5m width and 500m length. Furthermore, mineralization occurs as impregnations and disseminations. Quartz veins are the main host of mineralization cutting mostly meta-sedimentary rocks. Nevertheless, mineralization can be traced to the contact of tourmaline granite as small veins and veinlets.

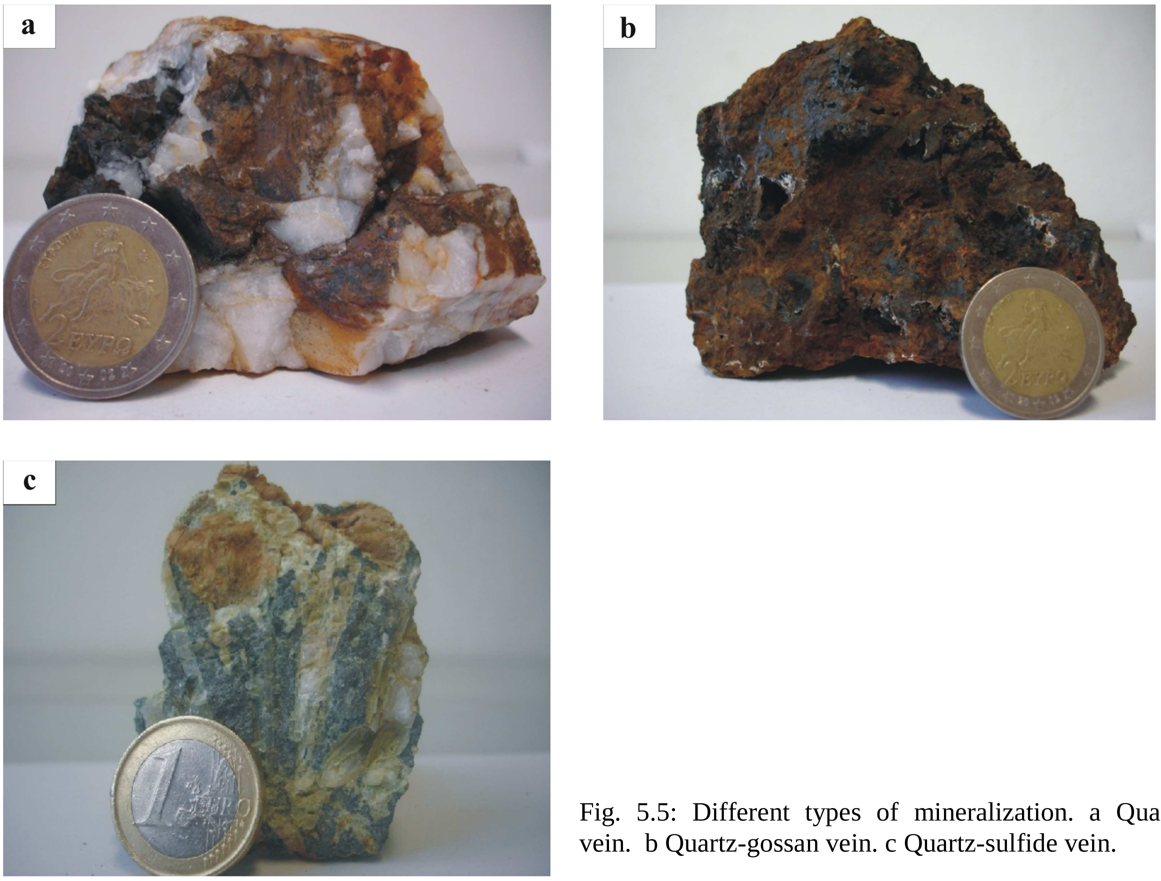

Fig. 5.5: Different types of mineralization. a Quartz vein. b Quartz-gossan vein. c Quartz-sulfide vein.

5.5 **Ore mineralogy**

<u>Sulfides:</u>

1- **Arsenopyrite:** Euhedral to subhedral grains of arsenopyrite are very common and occur in quartz-sulfide and quartz-gossan veins and veinlets. Alteration of arsenopyrite has led to the formation of Fe-oxides and scorodite. Inclusions of bismuthinite and Pb-Bi-Te-S phases were detected by electron microprobe study in arsenopyrite (Fig. 5.6). The amount of Ag and Se exceeds 140 ppm and 210 ppm, respectively (Table. 5.1).

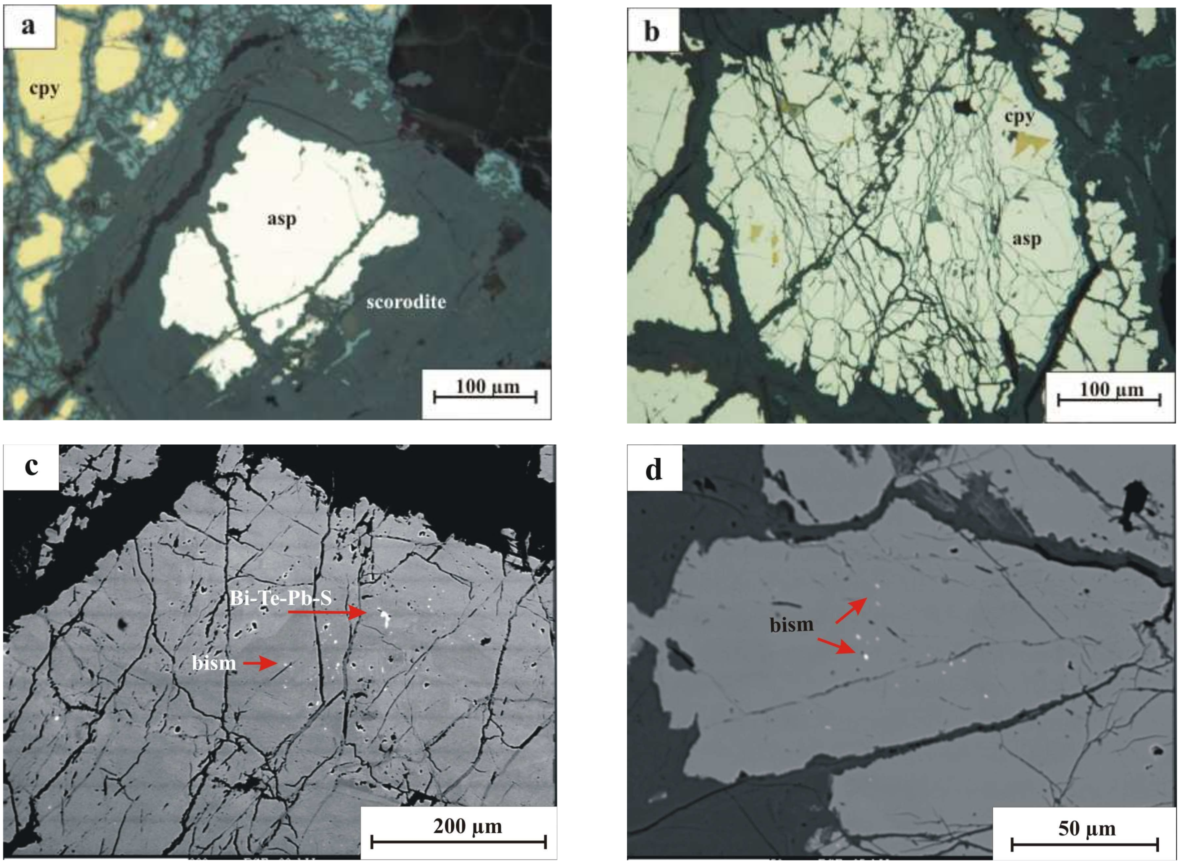

Fig. 5.6: a Arsenopyrite replaced by scorodite, oil immersion, PPL. b Brecciated arsenopyrite with inclusions of Bi and chalcopyrite, oil immersion, PPL. C & d BSE image of arsenopyrite showing inclusions of bismuthinite and Bi-Te-Pb-S phases.

Table. 5.1: Electron microprobe analysis of arsenopyrite.

Sample	**S**	**Fe**	**Te**	**As**	**Co**	**Ag**	**Au**	**Se**	**Sb**	**Bi**	**Total**
DH-13	wt%	wt%	ppm	wt%	ppm	ppm	ppm	ppm	ppm	ppm	wt%
1	17.71	33.4	< 340	51.14	< 88	140	< 50	210	< 55	< 240	102.27
2	18.13	33.3	< 340	50.48	< 88	100	<50	170	< 55	< 240	101.97
3	17.65	33.3	< 340	51.03	< 88	120	<50	140	< 55	< 240	102.02
4	17.93	33.6	< 340	50.79	< 88	90	<50	150	< 55	< 240	102.30
Mean	17.85	33		50.86		113		168			102.14

2- **Pyrite**: Pyrite is very widespread and occurs as separate aggregates, single grains and crystals in chalcopyrite and bornite and rarely in veinlets, cutting other minerals (Fig. 5.7).

3- **Chalcopyrite**: Chalcopyrite is ubiquitous, occurring as euhedral to subhedral grains, as well as small veinlets (Fig. 5.8). It is associated with pyrite, marcasite, pyrrhotite, sphalerite and galena. Replacement of chalcopyrite by blue sulfides, namely fine-grained mixtures of chalcocite and digenite (Figs 5.9a, 5.12) is a typical supergene alteration (De Waal 1980).

4- **Marcasite**: It occurs as single euhedral to anhedral grains and is associated mostly with chalcopyrite (Fig 5.9).

5- **Pyrrhotite**: Pyrrhotite occurs lesser than chalcopyrite and arsenopyrite, mainly as euhedral to subhedral grains and contains partly chalcopyrite (Fig. 5.10).

6- **Galena**: Subhedral to euhedral grains of galena occur mostly in quartz and gossan veins and are associated mainly with chalcopyrite and rarely as inclusion in pyrite, arsenopyrite and sphalerite. Replacement of galena by cerussite is very common (Fig. 5.11).

7- **Sphalerite**: Sphalerite occurs rarely in quartz and gossan veins and contains mostly inclusions of chalcopyrite and rarely galena (Fig. 5.12). Presence of chalcopyrite inclusions in sphalerite is a texture commonly seen in hydrothermal sulfide ores and has been named chalcopyrite disease by Barton (1970, 1978). Traditionally, the texture has been described as

8- **Boulangerite**: Boulangerite (Pb_5SbS_{11}) was identified as single elongated crystals in quartz vein (Fig. 5.13).

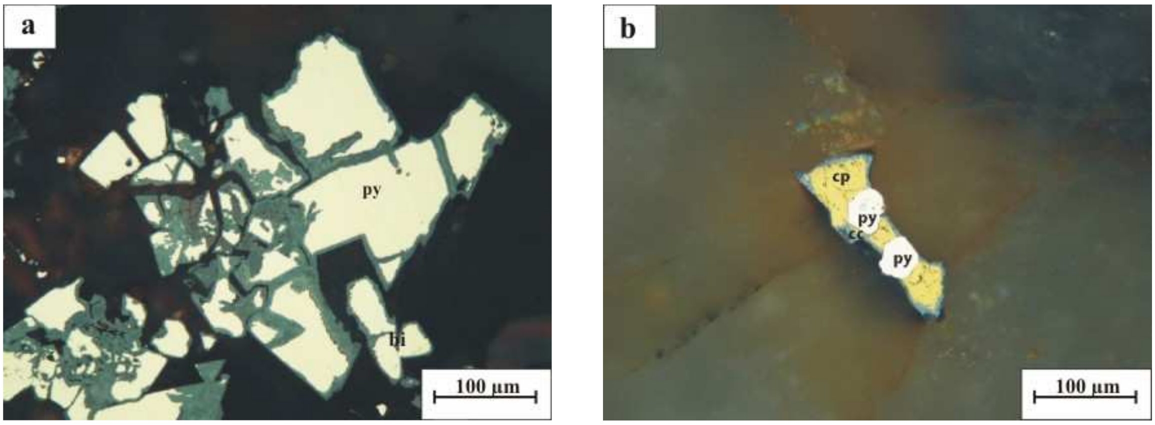

Fig. 5.7: a Pyrite, oil immersion, PPL. b Pyrite grains in chalcopyrite. Electron microprobe analysis revealed presence of galena inclusions in pyrite, oil immersion, PPL.

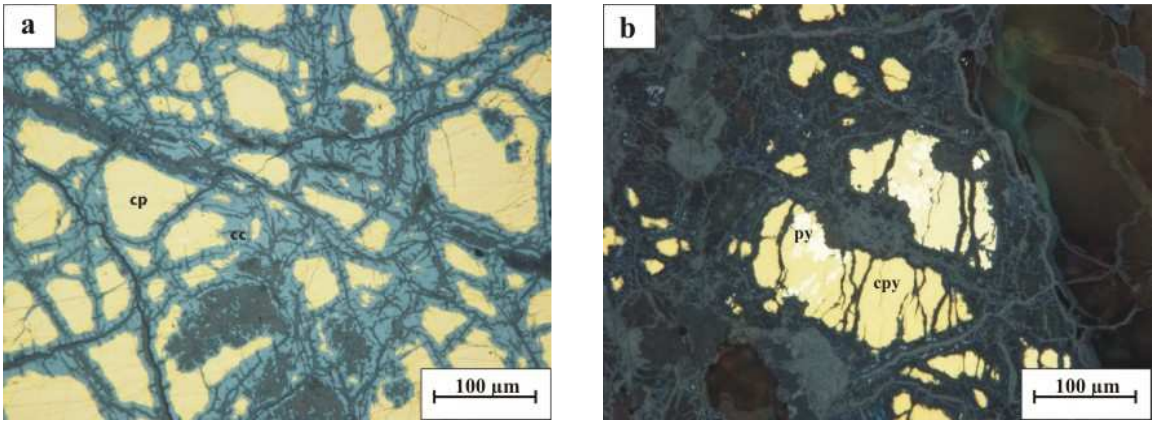

Fig. 5.8: a Chalcopyrite replaced by covellite, oil immersion, PPL. b Chalcopyrite with pyrite inclusion, oil immersion, PPL.

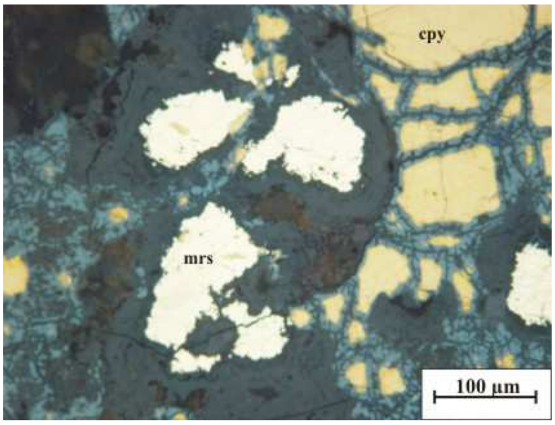

Fig. 5.9: Association of marcasite and chalcopyrite, oil immersion, PPL.

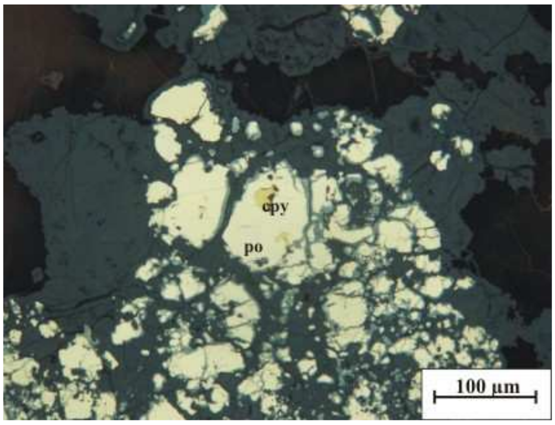

Fig. 5.10: Pyrrhotite with inclusion of chalcopyrire, oil immersion, PPL.

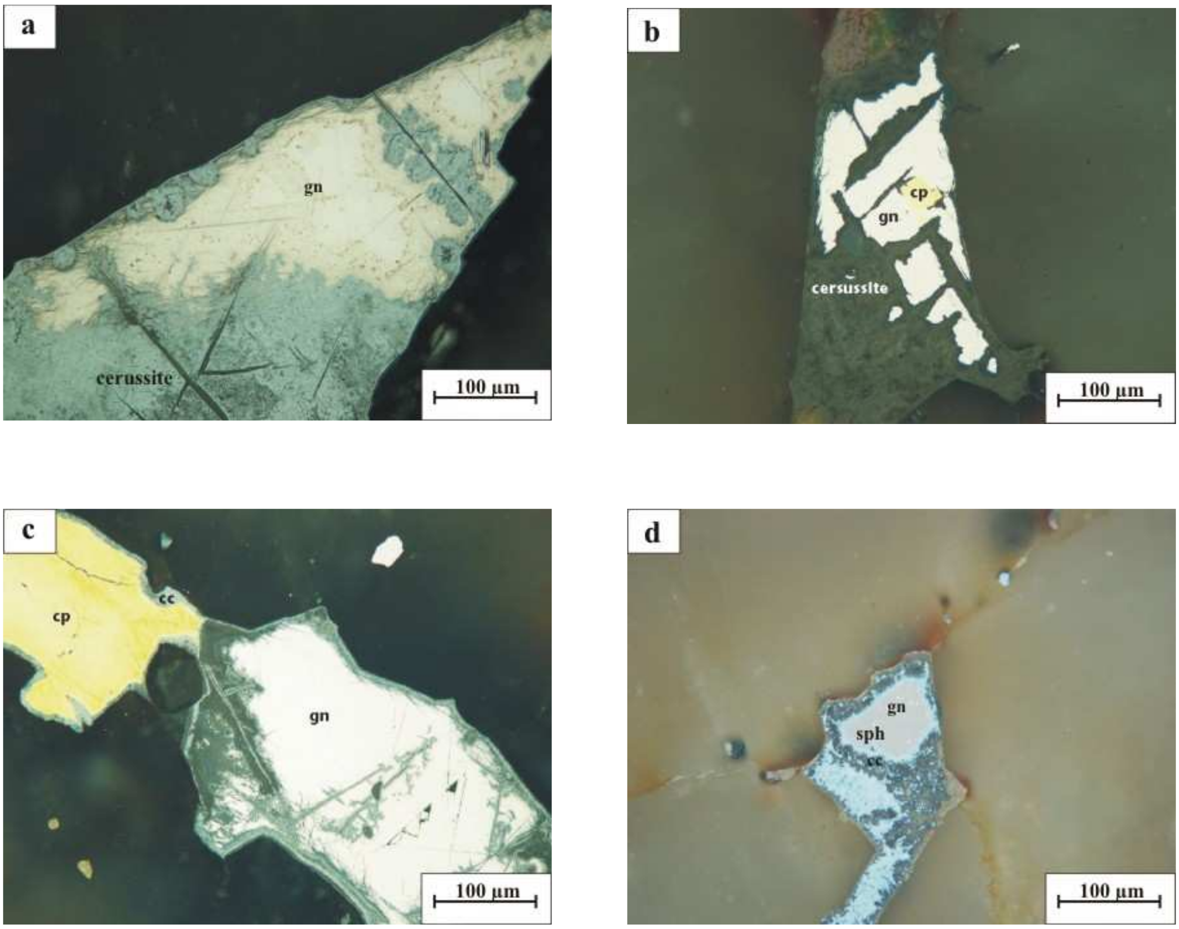

Fig. 5.11: a Galena replaced by needle-like cerussite in quartz vein, oil immersion, PPL. Replacement of galena by cerussite with chalcopyrite inside, oil immersion, PPL. c Association of galena and chalcopyrite. Chalcopyrite is replaced by covellite, oil immersion, PPL. d Inclusions of galena in shpalerite. Sphalerite is replaced by covellite, oil immersion, PPL.

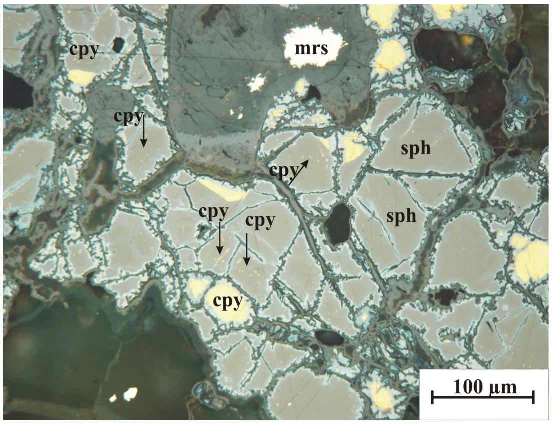

Fig. 5.12: Sphalerite with inclusions of chalcopyrite, oil immersion, PPL.

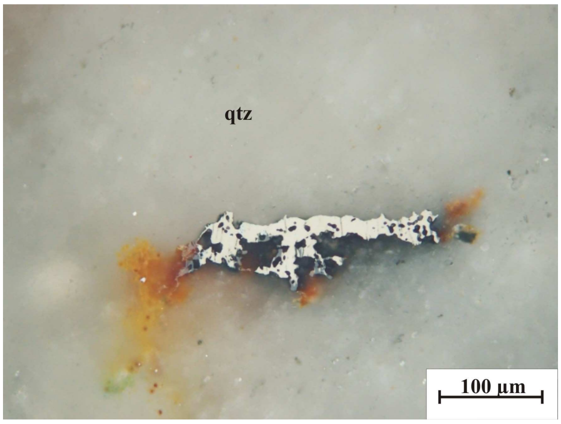

Fig. 5.13: Boulangerite in quartz, oil immersion, PPL.

an exsolution of chalcopyrite from sphalerite. However, Barton (1970, 1978) has presented convincing evidence that chalcopyrite disease is a replacement texture produced by Cu in aqueous solution reacting with FeS in sphalerite during late stages of ore formation. Also, Kojima and Sugaki (1985) through extensive experimental studies on the Fe-Cu-Zn-S system showed that the maximum solubility of CuS in sphalerite is 2.4 mol percent at temperatures from 500 to 300°C. They believe that this copper content seems to be insufficient for exsolution of an appreciable amount of chalcopyrite blebs (chalcopyrite disease) and such a texture can be interpreted better by replacement.

Oxides:

1- **Cassiterite:** Cassiterite is very common, occurring chiefly in quartz-sulfide veins (Fig. 5.14) and to a lesser extent in the meta-sedimenraty rocks. It is associated mainly with Cu sulfides and shows no zonation.

2- **Rutile:** Sparse grains of rutile can bee seen in quartz veins and granitic rocks of the area (Fig. 5.15). Its formation predates the sulfide stage and shows no relation with the main stage of mineralization.

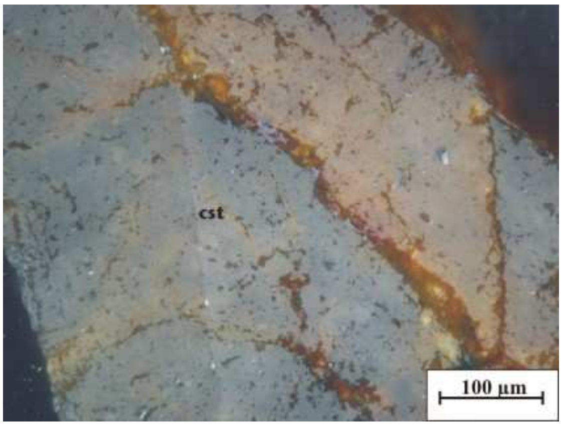

Fig. 5.14: Cassiterite in quartz-sulfide vein, oil immersion, PPL.

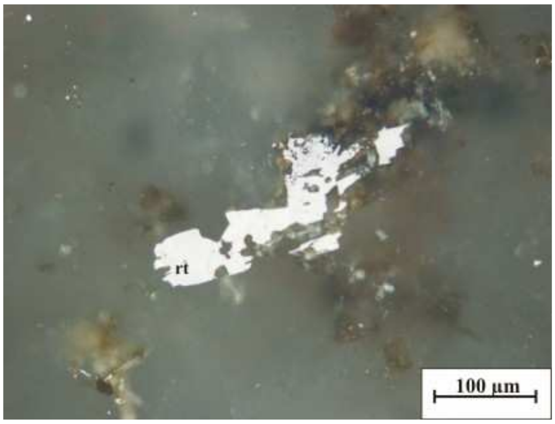

Fig. 5.15: Rutile in quartz vein, oil immersion, PPL.

Native elements:

1- **Au:** Despite high amounts of Au in the veins (partly 15 ppm), only one gold grain close to Fe-oxides in the quartz-sulfide vein was detected during electron microprobe and detailed ore microscopy studies of different samples (Fig. 5.16). The chemical evident for high Au concentrations and the mineralogical evidence for very rare occurrence of microscopical gold indicate the invisible nature of gold in the Deh Hossein prospect.

2- **Bismuth:** It occurs as inclusions of bismuthinite and Bi-Te-Pb S phase in massive arsenopyrite (Fig. 5.6c). Nezafati (2006) reported a variety of bismuth minerals such as sztrokayite (Bi_3TeS_2), Roosevelite ($BiAsO_4$) and Sulphotsumonite (Bi_3TeS) in arsenopyrite.

Phosphates:

1-**Monazite**

It occurs as dispersed fine-grained crystals in meta-sandstone (Fig. 5.17). Electron microprobe analysis revealed a very low amount of Th and that the dominant type is cerium monazite (Table 5.2).

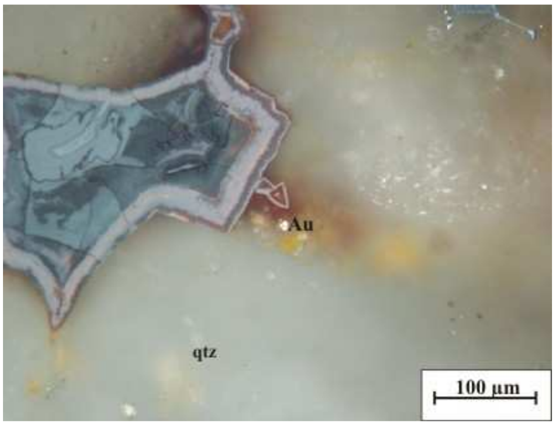

Fig. 5.16: Au grain in quartz-sulfide vein, oil immersion, PPL.

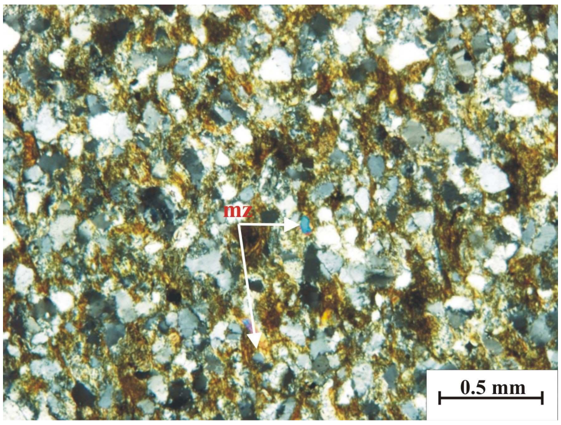

Fig. 5.17: Monazite in meta-sandstone.

Table. 5.2: Electron microprobe analyses of monazite, Deh Hossein prospect. Values in wt%.

Sample	P_2O_5	SiO_2	CaO	Ce_2O_3	Pr_2O_3	Nd_2O_3	ThO_2	La_2O_3	SmO	PbO	U_2O_3	Total
DH-6	32.04	0.81	0.57	32.79	2.19	14.65	bdl	13.26	2.48	bdl	bdl	98.78

Bdl: below detection limit. Detection limits for Th, Pb and U are 4000, 1000 and 1000 ppm, respectively.

The low ThO_2 content (<1 wt%) indicate that monazite is of hydrothermal origin (Schandl & Gorton 2004).

5.6 **Paragenetic sequence**: The great variety of ore samples, i.e meta-sedimentary rocks, quartz-sulfide veins, quartz-gossan veins and together with removal of the rich parts of the mineralized veins by the ancient miners, make a reliable outline of the paragenetic sequence difficult. Nevertheless, based on ore microscopy and electron microprobe studies, the following paragenetic sequence can be envisaged (Fig. 5.18). The early stage involves formation of oxide minerals at higher temperatures. Middle stage is characterized by more f_{S2} of the ore-bearing solutions, and formation of the high temperature oxidic minerals such as, cassiterite, and native Bi. Arsenopyrite and pyrite start to form in this stage. Late or sulfidic stage represents input of high sulfur in ore-bearing solutions and formation of many sulfides like arsenopyrite, chalcopyrite, pyrrhotite, marcasite, and then galena and sphalerite. Formation of quartz and partly tourmaline continued to this stage. A variety of oxidic minerals and gold characterize supergene process.

5.7 **Sphalerite composition**

Detailed ore microscopy together with electron microprobe study revealed chemical heterogeneity in sphalerite, evidenced by different values of mol % Fes and Cus. These values coupled with sulfide association indicate two distintc types, comprising Cu-poor and Cu-rich sphalerites (Fig. 5.19). The first Cu-poor group is characterized respectively by Fes and Cus conents of 7.06 to 8.15 mol % (mean 7.50), and 0.09 to 1.57 mol % (mean 0.68) (Appendix. 4). The sulfide association is typified by galena, pyrite and chalcopyrite. There is no primary pyrrhotite and chalcopyrite grains are mostly fresh with no replacement by blue sulfides, i.e. mixture of bornite, chalcocite, digenite and covellite. Additionally, chalcopyrite inclusions (chalcopyrite disease) occur very rarely in sphalerite. Conversely, the second group or Cu-rich sphalerite is marked by lower Fes (0.44 to 2.59 mol %, mean 1.17) and higher Cus (1.47 to 3.62 mol %, mean 2.20), (Appendix 5). Sphalerite is in equilibrium with marcasite, chalcopyrite grains are mostly replaced by blue sulfides and chalcopyrite inclusions (chalcopyrite disease) in sphalerite is very common (Figs. 5.8a & 5.12). The chemical heterogenity can be displayed conveniently on log a_{S2} (or log f_{S2})-1000/T, K diagrams (Scott 1983) (Fig. 5.20) where pressure is not an improtrant variable. The FeS content decreases gradually with increasing a_{S2}, across the pyrrhotite field until at the pyrrhotite-pyrite buffer the sphalerite contains 20.6 mol % FeS below 600^{o}C or slightly less FeS at higher temperatures. Within the pyrite/marcasite field which contains most of the analyzed sphalerites, the decrease in FeS content of sphalerite with increasing f_{S2} is much greater resulting in a close spacing of isopleths to even higher values. As noted before, high

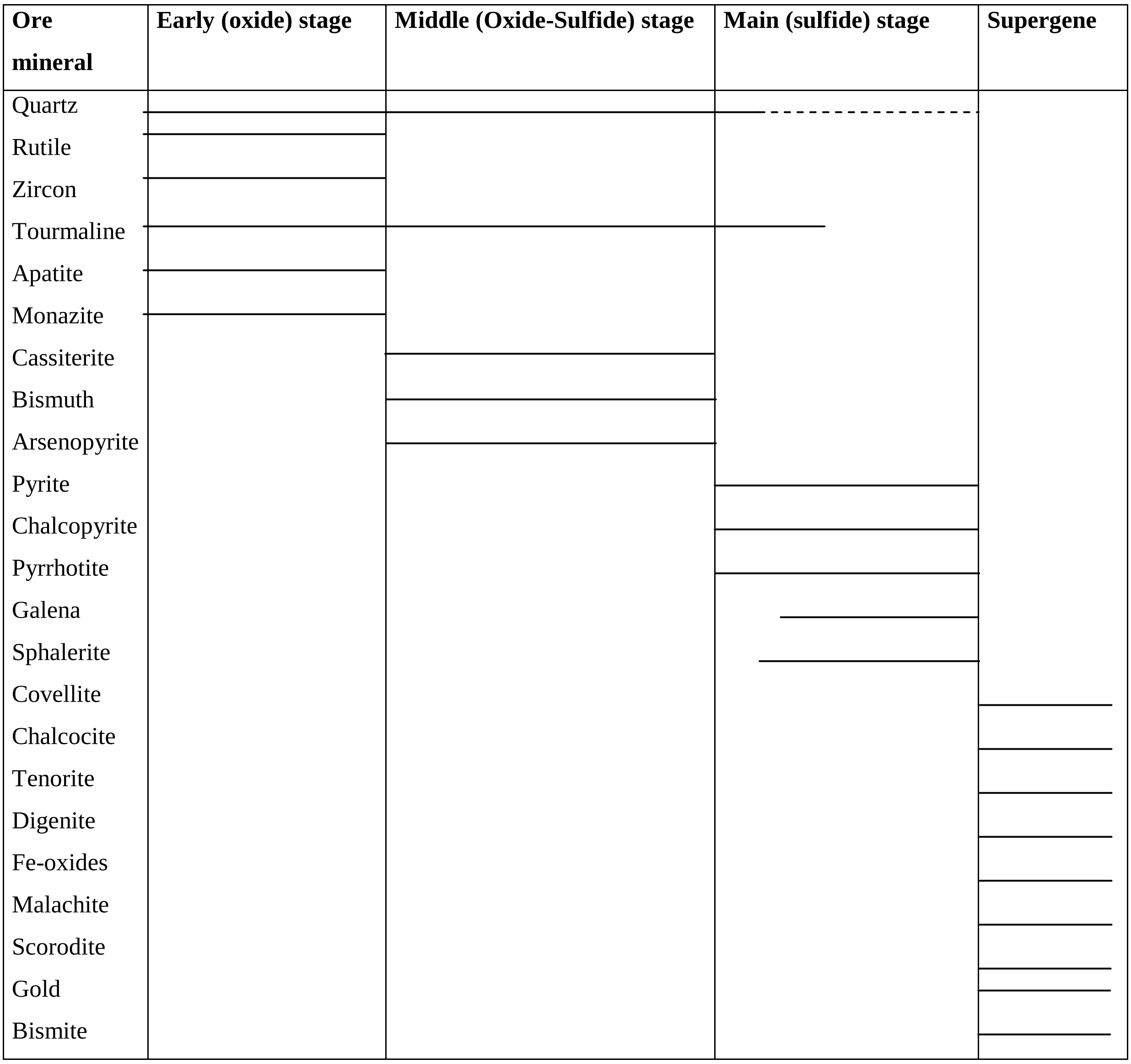

Fig. 5.18: Paragenetic sequence of the Deh Hossein prospect.

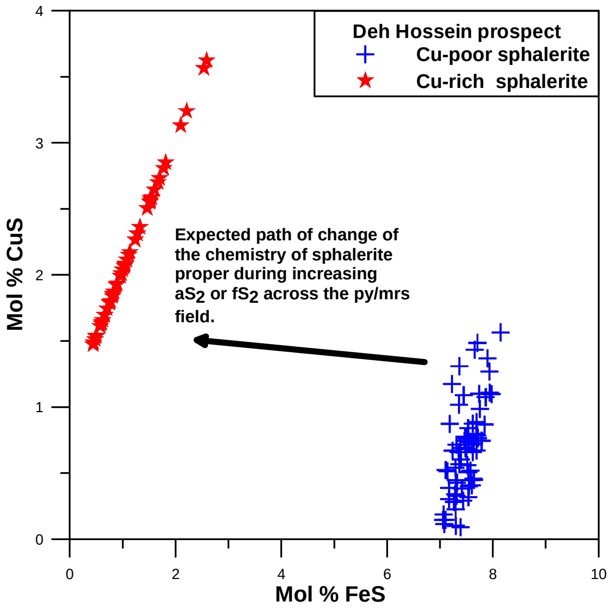

Fig. 5.19: Fe vs Cu in sphalerite, illustrating the change of composition from Cu-poor to Cu-rich.

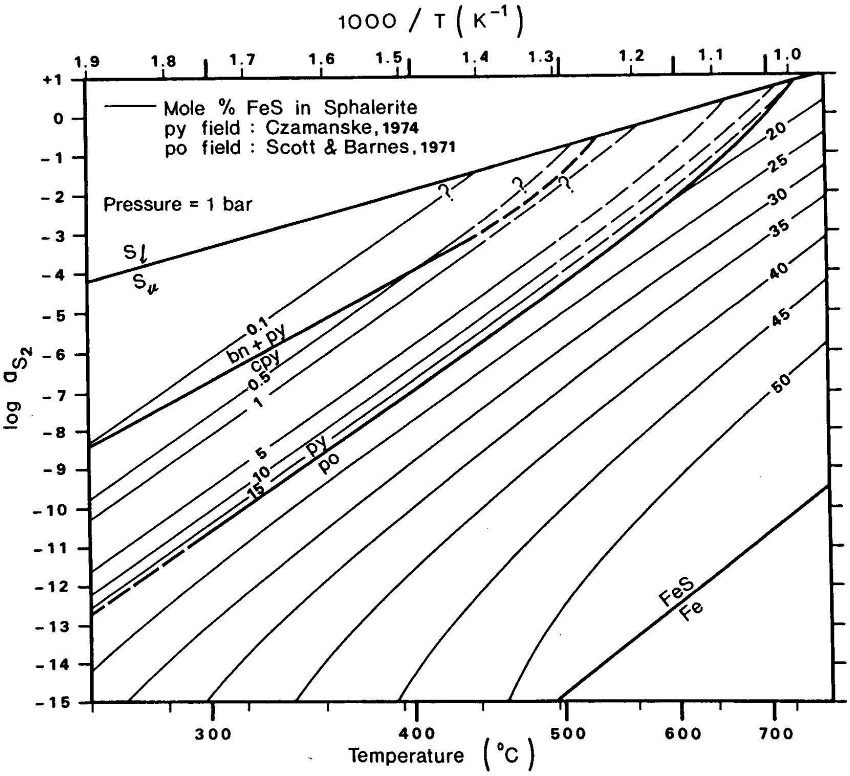

Fig. 5.20: Phase relationships for the Fe-Zn-S system at 1 bar (after Scott 1983). Isopleths are mol % FeS in sphalerite coexisting with pyrrhotite or pyrite/marcasite. The analyzed sphalerites are located mostly in the field of py/mrs stability, shifitng toward bn+py/cpy boundray, repersented by Cu-rich sphalerites and blue sulfide.

chalcopyrite inclusions (chalcopyrite disease) in sphalerite is believed to be result of replacement produced by Cu in aqueous solutions reacting with FeS in sphalerite (Barton 1970, 1978, Kalogeropoulos 1982). This argue is borne out by the experimental data of Hutchison and Scott (1981) who have shown that at high a_{S2}, the solubility of CuS in sphalerite is very low, less than 1 mol % below 600°C. The studied sphalerites have been formed at temperatures lower than 600°C, where the equilibrium solubility of Cu in sphalerite must be in the range of tens or hundreds of ppm, which is against the explanation by exsolution.

5.8 **Geochemistry**

25 samples from meta-sandstone, quartz-sulfide veins and gossan were analyzed for trace elements (Appendix 5). Except one sample (DH-34) that shows impregnation of sulfides, the Au content in meta-sandstone is below the detection limit. Gossan and quartz-sulfide veins have up to 1.36 ppm Au. Au shows good correlation with As and Ag and to a lesser extent with Sb and Bi (Fig. 5.21). Lesser amount of Au in meta-sandstone in with respect to quartz-sulfide veins arises possibly from leaching by hydrothermal solutions and precipitation in the

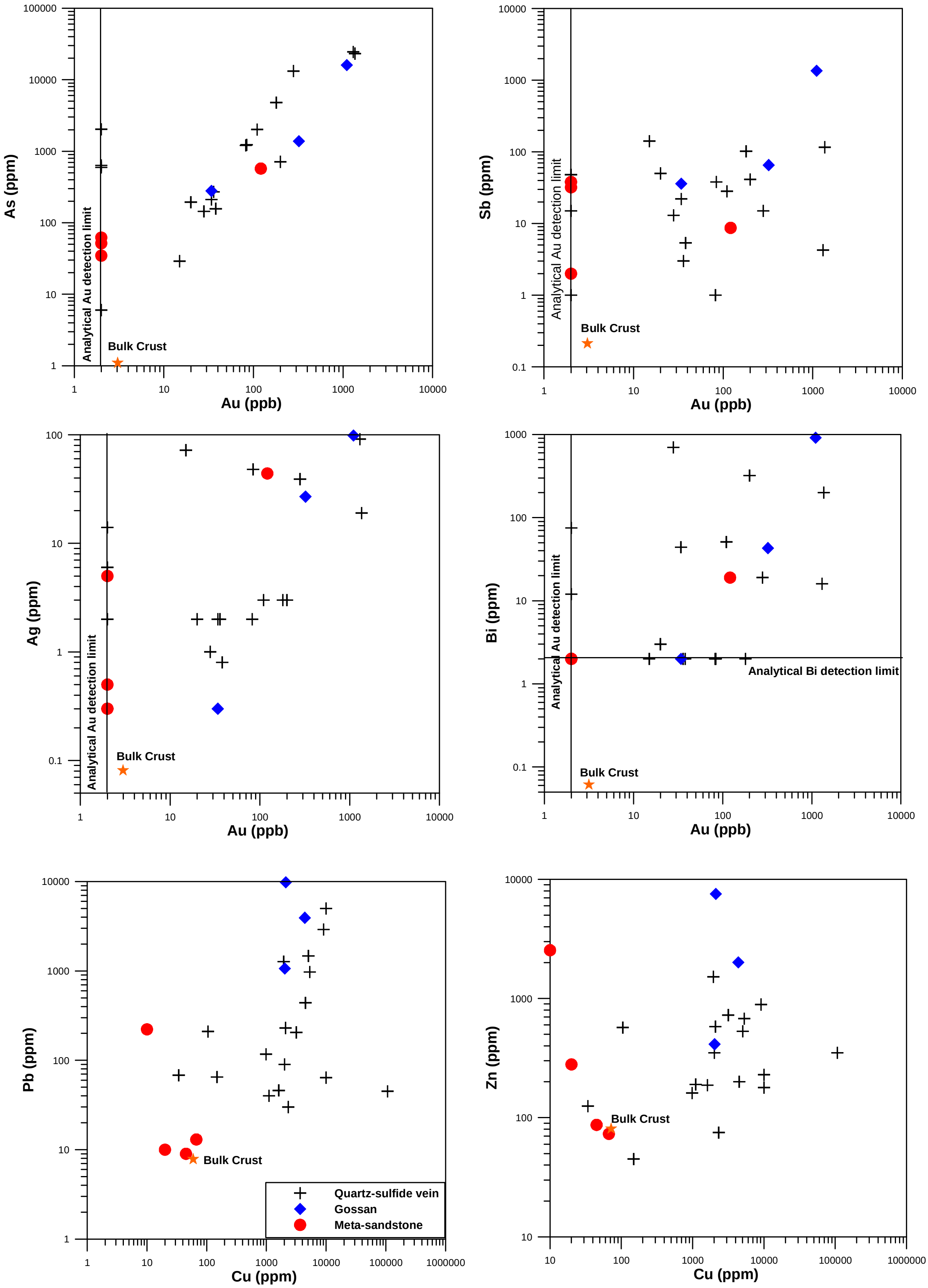

Fig. 5.21: Variation diagrams of trace elements of the ores, Deh Hossein prospect.

veins. Sn, Cu, and As contents also show the same trend as Au and increase up to 4.7 %, 10 %, and 2.3 % in quartz-sulfide veins, respectively. Lower amounts of Cu in gossan comparing to quartz-sulfide veins are likely from leaching of the Cu sulfides during weathering. Bi, Pb and Zn are strongly enriched. Cu shows good correlation with Zn and Pb, particularly in quartz-sulfide veins and to a lesser extent gossan (Fig. 5.20). New exploration data show grades of Au and Sn up to 13 ppm and 6 %, respectively (Geological Survely of Iran 2006). Reconnaissance electron microprobe study on arsenopyrite revealed presence of Sb, Ag and Se higher than detection limit (Table. 5.1). Nezafati (2006), reported values of gold in a variety of phases, particularly bismuth minerals (up to 4000 ppm), arsenopyrite (up to1900 ppm) and kobellite (up to 1000 ppm) which indicate Au-As-Bi metal association.

5.9 **Oxygen Isotope data**

5 quartz samples from the Deh Hossein prospect were analyzed. The $\delta^{18}O$ values range from 15.5 to 19.4 ‰ (Table 5.3). These values show likewise, magmatic hydrothermal fluids with stronger isotopic exchange with metamorphic country rocks. Unlike to the Nezam Abad and Astaneh, the mineralized hydrothermal quartz and quartz-sulfide veins are hosted here entirely by meta-sedimentary rocks which appear to control the oxygen isotope composition of the fluids.

Table 5.3: $\delta^{18}O$ values of quartz samples, Deh Hossein prospect.

Sample	**$\delta^{18}O$ (‰)**	**Host rock**	**Ore mineral(s)**
DH-7	19.4	Metasandstone	gn, py, cpy, asp, sph, mrs
DH-11	18.8	Metasandstone	py, cpy, asp, mal
DH-13	18.1	Phyllite	py, cpy, asp,
DH-18	15.5	Phyllite	gn, py, cpy, asp, sph, mrs
DH-23	18.6	Metasandstone	gn, py, cpy, asp, sph, mrs
Mean	18.1±1.5σ		

Sulfur isotope analysis of sulfides by Nezafati (2006) shows the value of $\delta^{34}S$ (five samples, ave. -2.36 ‰) between 5.5 ‰ in galena and 0 ‰ in arsenopyrite. These values indicate a rather narrow range near zero and suggest like Nezam Abad and Astaneh an igenous sulfur origin, for the Deh Hossein prospect.

Chapter 6

6. Conclusion and proposed genetic model

Magmatism in the study area is characterized by four subduction-related I-type, calc-alkaline granitic to quartzdioritc intrusions of ilmenite-series. These intrusions were emplaced in the Mid-Jurassic (Nezam Abad granodiorite), Late Cretaceous (Astaneh granodiorite) and Eocene (Nezam Abad quartzdiorite and Shirmazd microgranite) along the active Andian-like margin, i.e. Sanandaj-Sirjan zone, whose calc-alkaline magmatic activity progressively shifted northward. Contrary to the quartzdioritic units of the Nezam Abad complex and the Shirmazd microgranite with metaluminous nature, the Astaneh granodiorite and the Gousheh granite are peraluminous. The emplacement of these intrusions is attributed to the northeastward subduction underneath Central Iran and closure of the Neo-Tethys along the Sanandaj-Sirjan zone from Triassic to Miocene. Rb-Sr and Sm-Nd isotope data suggest a lower crustal Meso-Proterozoic protolith for the Astaneh and the Nezam Abad intrusions (T_{DM} around 1.5 Ga), while the microgranite rocks of the Shirmazd Mountain represent more input of mantle-derived materials (ε_{Nd} 1.7 to 2.0) with corresponding young depleted-mantle model ages around 500-800 Ma.

Mineralization in the Nezam Abad and Astaneh ore deposits is hosted solely by intrusions, while in the Deh Hossein occur in quartz-sulfide veins, cutting the low-grade metamorphic country rocks. In Astaneh, mineralization is hosted by the altered microgranitic rocks with microgranular to partly porphyritic texture and occurs in quartz-sulfide and sulfide vein/veinlets as well as subordinate disseminations. Alteration is not pervasive and confined to the microgranitic rocks with sericitization, chloritization, silisification and rare carbonatization. Ore mineralogy is typified by gold and dominant pyrite-chalcopyrite-arsenopyrite assemblage. Gold occurs both as free visible grains in alluvial deposits and host rock, as well as invisible phase in arsenopyrite. Arsenopyrite includes inclusions of native bismuth and show elevated values of Se, Sb and Ag.

In Nezam Abad, mineralization is hosted by the moderately evolved quartzdioritic units of the Nezam Abad complex and occurs in quartz-tourmaline and aplite dikes. Ore minerals include invisible gold, scheelite, cassiterite and a variety of sulfides, particularly arsenopyrite-chalcopyrite-pyrite-pyrrhotite assemblage. Replacement of pyrrhotite by marcasite is very common, indicating transition from an early high-temperature stage of pyrrhotite±pyrite toward a late stage of pyrrhotite alteration to pyrite/marcasite. Scheelite-only mineralization in Nezam Abad is attributed to the high Ca/Fe ratio of ore-bearing solutions, resulting from remobilization of Ca during plagioclase destruction. Furthermore, it shows lower oxygen fugacity and prevailing Fe-sulfide phase, i.e. pyrrhotite-arsenopyrite. Arsenopyrite includes inclusions of bismuthinite, native bismuth, löllingite and Te-Bi-Pb-S phases. Rb-Sr and Sm-Nd isotope data of hydrothermal tourmaline show the same compositional field with quartzdiorite, i.e. origin from crustal sources. Moreover, boron isotope analysis of hydrothermal tourmaline confirms the source from continental crust (Ahmad Khalaji 2006). Arsenopyrite and other phases like schneiderhöhnite, pyrrhotite and Bi-minerals host elevated amounts of invisible gold (Nezafati 2006). Arsenopyrite thermometry shows temperature formation in the range of 580^{o}C-650^{o}C. Pervasive alteration is tourmalinization with subordinate chloritization and sericitization.

Mineralization in Deh Hossein, occurs as quartz sulfide veins and their gossans, hosted by the Jurassic meta-sedimenatry country rocks. Ore minerals consist of gold, cassiterite, dominant arsenopyrite-chalcopyrite-pyrite assemblage with subordinate marcasite and pyrrhotite. Galena and sphalerite are locally high. Arsenopyrite encompasses bismuthinite and native bismuth. Gold occurs as free visible grain in quartz as well as invisible phase in aresnopyrite, Bi-Te minerals, chalcopyrite, krupkaite and kobellite (Nezafati 2006). Gold, tin and copper show high anomaly. Alteration is dominated by sericitization, chloritization, silisification and subordinate tourmalinization and monazitization.

Oxygen isotope data of hydrothermal quartz in the studied ore deposits are in accordance with magmatic to magmatic-metamorphic origins for hydrothermal fluids. Higher value of δ^{18}O (‰) in Deh Hossein is due to more interaction of hydrothermal fluids with metamorphic country rocks and demonstrates lower water/rock ratio and more depth of formation than two other ore deposits. The δ^{34}S (‰) values of different sulfides in the ore deposits show a rather narrow range near zero, confirming igneous origin.

The studied ore deposits exhibit similarities in 1- alteration type (sericitization-chloritization-silicification), 2- metal association (Au-As-Bi±Sb±Te±W), 3- occurrence of gold (invisible phase in arsenopyrite and visible grain in quartz), 4- stable isotope ratios (magmatic and magmatic-metamorphic fluids with no or less meteoric interaction), 5- associated granites (moderately reduced, metaluminous, I-type and calc-alkaline intrusions of ilmenite-series), 6- a reduced ore mineral assemblage (arsenopyrite-pyrrhotite-chalcopyrite-pyrite), 7- very low amount of base metals, 8- absence of magnetite, 9- areally restricted, commonly weak hydrothermal alteration, and 10- tectonic setting (continental arc). These features indicate more affinity of the studied ore deposits to the intrusion-related gold deposits. This class of ore deposits was defined by many geologists, e.g. Sillitoe (1991), McCoy et al. (1997), Thompson et al. (1999) and Lange et al. (2001) from Interior Alaska and

Yukun Territory in United States, Korri Kollo in Bolivia, Tintina gold belt in Australia and some other parts of the world. The intrusion-related gold, tungsten and tin deposits, are associated with more felsic (granodiorite-granite) intrusions, which in the case of tungsten and tin, are best described as reduced I-type magmas (Thompson et al. 1999). On the contrary, porphyry copper-gold and gold-only systems are typically associated with highly oxidized intermediate (diorite-monzonite) I-type intrusions (Sillitoe 1993). The available isotopic and geochemical data from the studied intrusions indicate the presence of significant crustal components, although micrograniticgold-bearing rocks of the Shirmazd Mountain, show more input of mantle-derived materials. The third important discriminating factor of the studied ore deposits with porphyry system is characteristic metal signature consisting of bismuth, tungsten, arsenic, tin, tellurium and antimony and general deficiency in base metals as proposed by McCoy et al. (1997), Thompson et al. (1999), Lang et al. (2001). This different metal assemblage with porphyry system can be illustrated schematically with reference to degree of fractionation and oxidation state of metal-bearing magmas (Fig. 6.1). This diagram illustrates the possible distinctive composition state, where gold may be concentrated with lithophile elements, particularly tungsten.

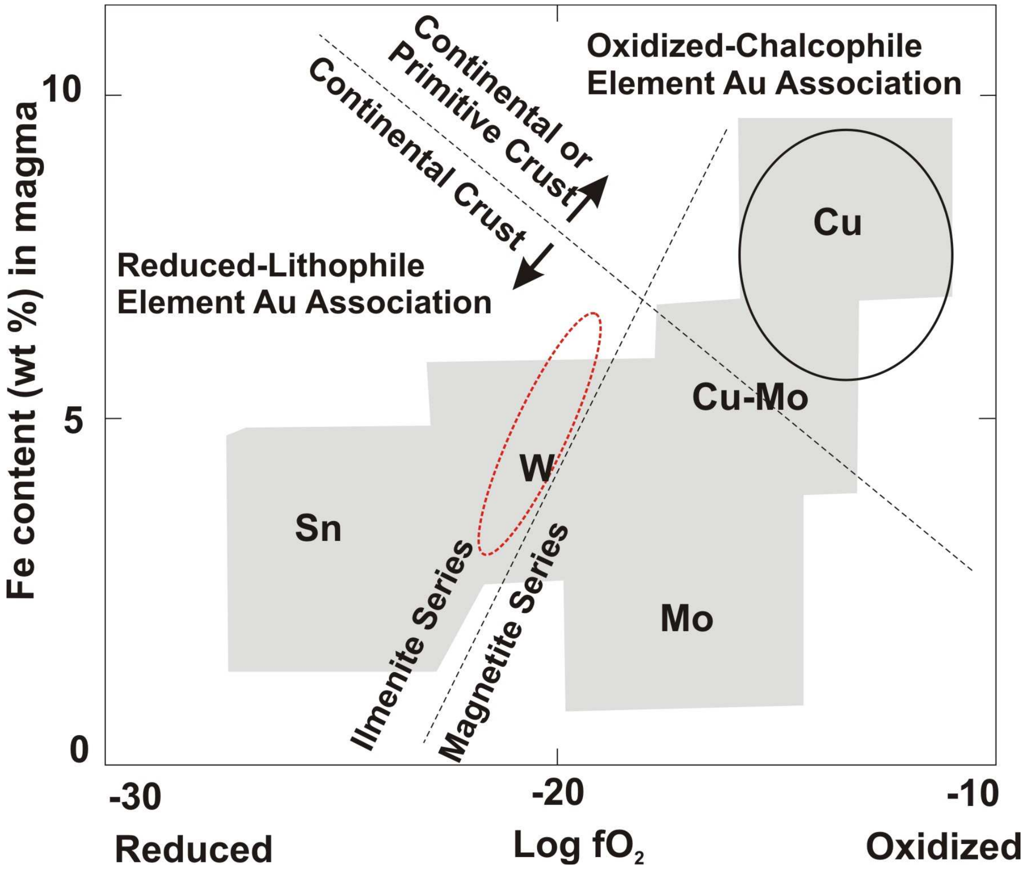

Fig. 6.1: A schematic representation of the relationship between degree of fractionation and oxidation state for magmas associated with different dominant metal assemblage. The probable position of the studied ore deposits have been shown by red elipsoid, comparing to the more typical copper-gold (chalcophile) systems (modified from Thompson et al. 1999).

Association of bismuth-tungsten-arsenic in the intrusion-related gold deposits, worldwide suggests a common set of genetic processes. Despite the role of continental crust in magmas from intrusions of the study area, the role of the crust as a distinct source of metals, particularly for gold is not clear. In the study area, gold, tungsten and tin are associated with more fractionated phases, i.e microgranite, aplite dikes and quartz-tourmaline veins. Sulfur and oxygen isotope data support magmatic and magmatic-metamorphic origin for the hydrothermal fluids in the studied ore deposits. Gold can be concentrated during fractionation of felsic magma and removed by crystallization of sulfides (Thompson et al. 1999). Invisible gold in a variety of sulfides, particulary arsenopyrite as well as bismuth minerals, is very common in the study area, suggesting a possible origin of gold with other elements form the mantle.

Metamorphogenic fluids were not during mineralization, as magmatic-hydrothermal activity (Eocene magmatism) did not overlap Jurassic regional metamorphism in time. Detailed studies of Agard et al. (2005) have shown that maximum temperature formation of Hamadan phyllite, which are country rocks of the study area did not exceed more than 450^{o}C. It is unlikely that low-grade metamorphism could have sustained contineous, regional fluid circulation for 90 m.y. or more. Nevertheless, interaction of hydrothermal solutions with metamorphic country rocks is evident from O and B isotope data, suggesting probable partial leaching of ore elements by hydrothermal fluids.

Contemporaneous extensional and compressional tectonics prior and after Eocene have been stated by Alavi (1994), Mohajjel et al. (2003) and Agard et al. (2005) during Tertiary and along the Sanandaj-Sirjan zone. Tillman et al. (1981), has expressed a period of Tertiary crustal extension along the Sanandaj-Sirjan zone and linked pre-Miocene extensional tectonics to contineous underthrusting, as well. Therefore, dehydration of such underthrusted rocks might have been a source of ore-forming fluids. This mechanism has been used by Moritz et al. (2006), to explain gold formation at Muteh mine in the Sanandaj-Sirjan zone. Moritz et al. (2006) believe that the early to middle Eocene gold ore formation at Muteh is a result of protracted geologic evolution of the Sanandaj-Sirjan tectonic zone and that gold mineralization was related to normal faulting due to Eocene crustal extension during the final stages of exhumation of a metamorphic rock complex.

The late Eocene gabbroic intrusions and dikes (40 to 38 Ma) next to and in ophiolite complex in the Sanandaj-Sirjan zone (outside the Shazand quadrangle) as well as calc-alkaline magmatism in the neighbouring Urumieh-Dokhtar magmatic arc have been attributed to the slab detachment during Eocene by Agard et al (2005) and Ghasemi and Talbot (2006). In the study area, there is no gabbroic intrusion and ophiolite complex, and evidence supporting typical extensional regime and exhumation of a metamorphic complex are missing. Therefore, slab detachment mechanism should be considered cautiously to explain formation and emplacement of the Eocene I-type, ilmenite-series intrusions of the study area and more investigations are required to prove the presence of exhumation of a metamorphic complex.

As noted before, the ore deposits-associated intrusions in the study area are moderately reduced continental I-type subduction intrusions of ilmenite-series granites, ranging from granite to quartzdiorite. These compositions could not be derived from a meta-sedimentary source alone (McCoy et al. 1997). A more plausible model is that these plutons were formed by partial melting of mantle, induced by the presence of water released from dehydration of subducted oceanic crust. This phenomenon occurs at a depth of 80 to 100 km (Hedenquist and Lowenstern 1994). The presence of water causes melting in the mantle basement above the subducting slab, resulting in magma formation and ascension. Presence of carbonaceous materials at higher crustal layers could have played a role in creating gold-favorable magma. These materials are present in the study area, evidenced by scattered occurrences of graphite in the low-grade metamorphic country rocks, particularly around the Nezam Abad complex. Such a materials would most likely affect the oxidation state during melt ascent, leading to generation of an ilmenite-series magma. Subsequent fractionation of this melt, would release gold into the plutonic hydrothermal systems (Fig. 6.2).

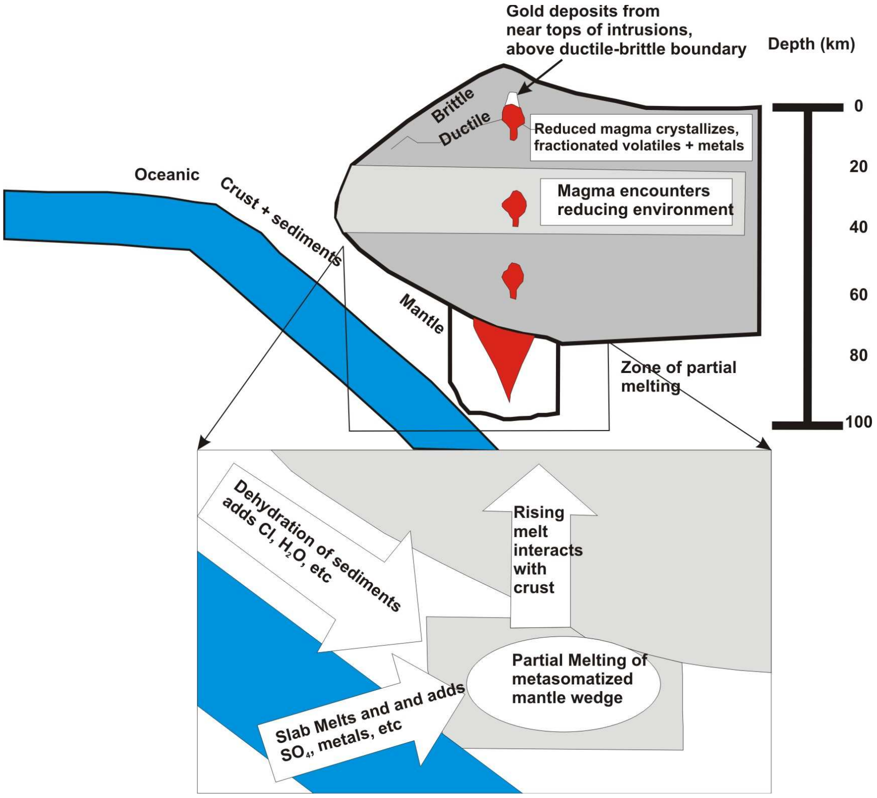

Fig. 6.2: Derivation of volatile- and metal-rich, I-type, ilmenite series plutons in a subduction setting (after Hedenquist and Lowenstern 1994).

References

Agard, P., Omrani. J., Jolivet, L., Mouthereau, F. 2005. Convergence history across Zagros (Iran): Constrains from collisional and earlier deformation. International Journal of Earth Sciences, 94: 401-419.

Ahmad Khalaji, A. 2006. Petrology of the Granitoid Complex of Borujerd, Ph.D thesis (in Persian). University of Tehran, 190 p.

Alavi, M. 1994. Tectonics of the Zagros orogenic belt of Iran: new data and interpretations. Tectonophysics, 229: 211-238.

Alavi, M., Mahdavi, M. A. 1994. Stratigraphy and structures of the Nahavand region in western Iran and their implications for the Zagros tectonics. Geological Magazine, 131: 43-47.

Baharifar, A., Moinevaziri, H., Bellon, H., Piqué, A. 2004. The crystalline complexes of Hamadan (Sanandaj-Sirjan zone, western Iran): Metasedimentary Mesozoic sequences affected by Late Cretaceous tectono-metamorphic and plutonic events. Comptes rendus Geosciences, 336: 1443-1452.

Barabanov, V. F. 1971. Geochemistry of tungsten. International Geology Review, 13: 332-344.

Barnes, H. L. 1997. Geochemistry of hydrothermal ore deposits, third edition, John Wiley & Sons, Inc.

Barton, P. B. Jr. 1970. Sulfide petrology. Mineralogical Society of America, 3: 187-198.

Barton, P. B. Jr. 1978. Some ore textures involving sphalerite from the Furutobe mine, Akita Prefecture, Japan. Mining Geology, 28: 293-300.

Bateman, P. C. 1982. Scheelite-bearing skarns of the East-Central Sierra Nevada, California, U.S.A, in: Gallagher, V. 1989. Geological and isotope studies of microtonalite-hosted W-Sn mineralization in SE Ireland. Mineralium Deposita, 24: 19-28.

Bellon, H., Braud, J. 1975. Données nouvelles du domaine métamorphique du Zagros (Zone du Sanandaj-Sirjan) au inveau de Kermanshah-Hamadan (Iran), Nature, âge et interprétation des Séries métamorphiques et des intrusions évolution structural. Fac, Sci, d’Orsay, Paris, 14p.

Benard, F., Moutou, P., Pichavant, M. 1985. Phase relations of tourmaline leucogranites and the significance of tourmaline in silisic magmas. Journal of Geology, 93: 271-291.

Berberian, M., King, G. C. P. 1981. Towards a palaeogeography and tectonic evolution of Iran. Canadian Journal of Earth Sciences, 18: 210-265.

Berberian, F., Berberian, M. 1981. Tectono-plutonic episodes in Iran, in: Gupta, H. K. and Delany, F. M. Zagros, Hindu Kush, Himalaya, Geodynamic Evolution. American Geophysical Union, Geodynamic Series, 3: 5-32.

Berberian, F., Muir, I. D., Pankhurst, R. J., Berberian, M. 1982. Late Cretaceous and Early Miocene Andean-type plutonic activity in northern Makran and Central Iran. Journal of the Geological Society of London, 139: 605-614.

Blevin, P. 2004. Metallogeny of Granitic Rocks. The Ishihara Symposium: Granites and Associated Metallogenesis, Geoscience Australia, 1-4.

Blevin, P. L., Chappel, W. 1995. Chemistry, origin, and evolution of mineralized granites in the Lachlan Fold Belt, Australia: The Metallogeny of I- and S- Type Granites. Economic Geology, 90: 1604-1619.

Burt, D. M. 1989. Vector representation of tourmaline compositions. American Mineralogist, 74: 826-839.

Burt, D. M. 1981. Acidity-salinity diagrams-application to greisen and porphyry deposits. Economic Geology, 76: 832-843.

Chappell, B. W., White, A. J. R. 1974. Two contrasting granite types. Pacific Geology, 8: 173-174.

Chiaradia, M. 2003. The evolution of tungsten sources in crustal mineralization from Archean to Tertiary inferred from lead isotopes. Economic Geology, 98: 1039-1045.

Clarke, M. C. G. 1983. Current Chinese thinking on the South China tungsten province. Trans. Inst. Min. Metall, 92: 10-15.

Darvishzadeh, A. 1991. Geology of Iran (in Persian), Danesh-e-Emrouz press, Tehran.

Davoudzadeh, M., Lensch, G., Weber-Diefenbach, K. 1986. Contribution to the paleogeography, stratigraphy and tectonics of the Infracambrian and Lower Paleozoic of Iran. Neues Jahrbuch für Geologie und Paläontologie-Abhandlungen, 172: 245-269.

Davoudzadeh, M., Weber-Diefenbach, K. 1987. Contribution to the paleogerography, stratigraphy and tectonics of the Upper Paleozoic of Iran. Neues Jahrbuch für Geologie und Paläontologie-Abhandlungen, 175: 121-146.

Deer, W. D., Howie, R. A. and Zussman, J. 1992. An introduction to the rock forming minerals. 2nd edition, Pearson Education Limited.

De Waal, S. A., Johnson, J. A.1981. Chemical heterogeneity in a base metal sulfide deposit. Economic Geology, 76: 694-705.

Farhadian, M. B. 1992. Geochemical and mineralogical investigation on Nezam Abad tungsten deposit, Arak, Iran, M.Sc thesis (in Persian), Tehran University, Iran.

Farhadian, M. B. 1999. List of analysis results of Tungsten exploration program at Nezam Abad, Internal report (in Persian), Geological Survey of Iran, Tehran.

Farzindoust, M. 2003. Isotopic study and geochemical data of southwest Astaneh, Arak. Unpublished M.Sc thesis, Tarbiat Modarres University, Tehran, Iran.

Field, C. W., Gustafson, L. B. 1967. Sulfur isotopes in the porphyry copper deposit at El Salvador, Chile. Economic Geology, 71: 1533-1548.

Foster, R. P. 1977. Solubility of scheelite in hydrothermal chloride solutions. Chemical Geology, 20: 27-43.

Förster, H. 1974. Magmentypen und Erzlagerstätten im Iran. Geologische Rundschau, 63: 276-292.

Förster, H. 1978. Mesozoic-Cenozoic metallogenesis in Iran. Journal of the Geological Society of London, 172: 245-269.

Gallagher, V. 1988. Coupled substitutions in schorl-dravite tourmaline: New evidence from SE Ireland. Mineralogical Magazine, 52: 637-650.

Gallagher, V. 1989. Geological and isotope studies of microtonalite-hosted W-Sn mineralization in SE Ireland. Mineralium Deposita, 24: 19-28.

Ghasemi, A., Talbot, C. J. 2006. A new tectonic scenario for the Sanandaj-Sirjan zone (Iran). Journal of Asian Earth Sciences, 26: 683-693.

Ghorbani, M. 2002. Introduction to the economic geology of Iran. National Geoscience Data Base of Iran, Report No: 2, 695p.

Haj Zein Ali, M. A. 1992. Geology and exploration at Nezam Abad tungsten deposit, Geological Survey of Iran, Internal report (in Persian).

Hallenstein, C. P, Pedersen, J. L. 1983. Scheelite mineralization in central east Greenland. Mineralium Deposita, 18: 315-333.

Hashemi, M. 2002. Gold mineralization associated with igneous body of Astaneh, Arak, Iran. Unpublished MSc thesis (in Persian), Teacher Training University of Tehran, Iran.

Hedenquist, J. W., Lowenstern, J. B. 1994. The role of magmas in the formation of hdrothermal ore deposits. Nature, 370: 519-526.

Heidari, S. M., Rastad, E., Mohajjel, M., Shamsa, S. M. J. 2006. Gold minerralization in ductile shear zone of Kervian (southwest of Saqez-Kordestan province). Geosciences, 58: 18-37.

Heinrich, C. A. 1990. The chemistry of hydrothermal tin-(tungsten) ore deposition. Economic Geology, 85: 457-481.

Hezarkhani, A., Williams-Joens, A. E. 1998. Controls of alteration and mineralization in the Sungun porphyry copper deposit, Iran: Evidence from fluid inclusions and stable isotopes. Economic Geology, 93: 651-670.

Hoefs, J. 2004. Stable isotope geochemistry. Springer-Verlag, Berlin, Germany.

Holtz, F., Johannes, W. 1991. Effect of tourmaline on melt fraction and composition of first melts in quartzofeldspathic gneiss. European Journal of Mineralogy, 3: 527-536.

Hooper, R. J., Baron, I., Hatcher, Jr., R. D., Agah, S. 1994. The development of the southern Tethyan margin in Iran after the break-up of ondwana, implications for the Zagros hydrocarbon province. Geosciences Iran, 4: 72-85.

Hsu, L. C. 1977. Effects of oxygen and sulfur fugacities on the scheelite-tungstenite and powellite-molybdenite. Economic Geology, 72: 664-670.

Hsu, L. C. 1981. Phase relations of some tungsten minerals under hydrothermal conditions. American Mineralogist, 66: 298-308.

Hsu, L. C., Galli, P. E. 1973. Origin of the scheelite-powellite series of minerals. Economic Geology. 68: 681-696.

Hutchison, M. N., Scott, S. D. 1980. Sphalerite geobarometry in the Cu-Fe-Zn-S system. Economic Geology, 76: 143-153.

Ishihara, S. 1981. The granitoid series and mineralization. Economic Geology, 75th Anniversary Volume: 458-484.

Ishihara, S. 2004. Metallogenic mineralization vs the granite series in the Mesozoic-Cenozoic Circum-Pacific plutonic belts. The Ihihara Symposium: Granites and Associated Metallogenesis. Geoscience Australia, 77-80.

Jackson, J. Mackenzie, D. 1984. Active tectonics of the Alpine-Himalayan belt between western Turkey and Pakistan. Geophysical Journal of the Royal Astronomical Society, 77: 185-264.

Jahangiri, H. 1999. Investigation into W-Sn anomalies in the areas of Nezam Abad and Bamsar, Internal report (in Persian), Geological Survey of Iran.

Karimzadeh Somarine, A., Moayyed, M. 2002. Granite- and gabbrodiorite-associated skarn deposits of NW Iran. Ore Geology Reviews, 20: 127-138.

Kelly, W. C., Turneaure, F. S. 1970. Mineralogy, paragenesis and geometry of the tin and tungsten deposits of the eastern Andes, Bolivia. Economic Geology, 65: 609-680.

Kojima, S., Sugaki, A. 1985. Phase relations in the Cu-Fe-Zn-S systems between 500^0 and 300^0 C under hydrothermal conditions. Economic Geology, 80: 158-171.

Kowsari, S. 2004. Detailed geochemical exploration of the Shazand area, scale: 1: 5000. Geological Survey of Iran.

Kretschmar, U. K., Scott, S. D. 1976. Phase relations involving arsenopyrite in the system Fe-As-S and their application. Canadian Mineralogist, 14: 364-386.

Lang, J. R., Baker, T. (2001). Intrusion-related gold systems: the present level of underestanding. Mineralium Deposita, 36: 477-489.

London, D. and Manning, D. A. C. 1995. Chemical variation and significance of tourmaline from Southwest England. Economic Geology, 90: 495-519.

MacCoy, D. T., Newberry., R. J., Layer, P. W., DiMarchi, J. J., Bakke, A., Masterman, J. S., Minehane, D. L. 1997. Plutonic related gold deposits of interior Alaska. Economic Geology, Monograph 9: 191-241.

Maddox, L. M., Bancroft, G. M., Scanini, M. J., Lorimer, J. W. 1998. Invisible gold: Comparison of Au deposition on pyrite and arsenopyrite. American Geologist, 83: 1240-1245.

Manning, D. A. C. 1982. Chemical and morphological variation in tourmalines from the Hub Kapong batholith of peninsular Thailand. Mineralogical Magazine, 45: 139-147.

Manning, D. A. C. 1986. Contrasting styles of Sn-W mineralization in Peninsular Thailand and SW England. Mineralium Deposita, 21: 44-52.

Manning, D. A. C., Henderson, P. 1984. The behaviour of tungsten in granitic melt-vapour systems. Contribution to Mineralogy and Petrology. 86: 286-293.

Marignac, C. H. 1989. Sphalerite stars in chalcopyrite: Are they always the result of an unmixing process ?. Mineralium Deposita, 24: 176-182.

Masoudi, F. 1997. Contact metamorphism and pegmatite development in the region SW of Arak, Iran, PhD thesis, The University of Leeds, UK.

Masoudi, F., Yardley, B. W. D. and Cliff, R. A. 2002- Rb-Sr geochronology of pegmatites, plutonic rocks and a hornfels in the region South-West of Arak, Iran, Journal of Sciences, Islamic Republic of Iran, 13(3).

Mehrabi, B., Yardley, B.W.D., Cann, J.R., 1999. Sediment-hosted disseminated gold mineralization at Zarshuran, NW Iran. Mineralium Deposita, 34: 673-696.

Moghaddam, G., 2003. Gold mineralization in the shear zone Zartorosht mining area, Sanandaj-Sirjan zone. 22th Geology conference, Geological Survey of Iran.

Momen Zadeh, M., Ghanati, S., 1995. Agh Darreh ore deposit: An example of epithermal gold mineralization in Tertiary rocks. 4th proceedings of mining symposium, Yazd University, Iran.

Mohajjel, M., Fergusson, B. C. L. and Sahandi, M. R. 2003. Cretaceous-Tertiary convergence and continental collision, Sanandaj-Sirjan Zone, western Iran, Journal of Asian Earth Sciences, 21: 397-412.

Moore, A. J. McM. 1977. Carrock tungsten mine, Cumbria, in: Gallagher, V. 1989. Geological and isotope studies of microtonalite-hosted W-Sn mineralization in SE Ireland. Mineralium Deposita, 24: 19-28.

Moritz, R., Ghazban., F., Brad, S. S. 2006. Eocene gold ore formation at Muteh, Sanandaj-Sirjan tectonic zone, Western Iran: A result of late-stage extension and exhumation of metamorphic basement rocks within the Zagros orogene. Economic Geology, 101: 1497-1524.

Nabavi, M. H. 1976. An introduction to geology of Iran, (in Persian), Geological Survey of Iran.

Nekouvaght Tak., M. A. 1997. Study of gold mineralization at Agh Darreh prospect. Unpublished MSc thesis, Shiraz University, 201 p.

Nezafati, N., Herzig, P. M., Pernicka., E., Momenzadeh, M., 2005. Intrusion-related gold prospects in the Astaneh-Sarband area, west central Iran. Proceedings of the Eight Biennial SGA Meeting Beijing, China. 1: 445-448.

Nezafati, N. 2006. W-Sn-W-Cu mineralization in the Astaneh-Sarband area, West-Central Iran. Dissertation, Universität Tübingen, 110 p.

Ojaghi, B., Shabani, K., Asfari, S. and Nezafati, N. 2001. Geological map of the Deh Hossein area, scale: 1:5000. Zaryaban Exploration Co, Internal Report.

Pirajno, F. and Smithies, R. H. 1992. The FeO/(FeO+MgO) ratio of tourmaline: A useful indicator of spatial variations in granite-related hydrothermal mineral deposits. Journal of Geochemical Exploration, 42: 371-381.

Plimer, I. R. 1987. The association of tourmalinite with stratiform scheelite deposits. Mineralium Deposita, 22: 282-291.

Radfar, J. 1987. Petrology of granitic rocks from Astaneh area, Iran. M.Sc thesis (in Persian), Tehran University, Iran.

Ramdohr, P. 1980. The ore minerals and their intergrowth, second edition, Akademie Verlag Berlin.

Ramezani, J., Tucker., R. D. 2003. The Saghand region, Central Iran: U-Pb geochronology and implications for Gondwana tectonics: American Journal of Science, 303: 622-665.

Richards, P.R., Wilkinson, D., Ulrich., Thoumas., 2006. Geology of the Sari Gunay epithermal gold deposit, Northwest Iran. Economic Geology 101, 1455-1496.

Rollinson, H. R. 1996. Using geochemical data: evaluation, presentation, interpretation. Longman Group UK Limited.

Sahandi, M. R., Radfar, J. 1992. Geological map of the Shazand, scale: 100,000. Geological Survey of Iran, Tehran-Iran.

Samin Resources. 2002. Detailed surface exploration at Astaneh Au prospect (Au in hard rock). Internal report, Tehran, Iran.

Schandl, E. S., Gorton, M. P. 2004. A textural and geochemical guide to the identification of hydrothermal monazite; criteria for selection of samples for dating epigenetic hydrothermal ore deposits. Economic Geology, 99: 1027-1035.

Schwartz, M. O. and Askury, A.K. 1989. Geologic, geochemical and fluid inclusion studies of the tin granites from the Bujang Melaka pluton, Kinta Valley, Malaysia. Economic Geology, 84: 751-779

Shamanian Esfahani, G. 1994. Geochemical, mineralogical and fluid inclusion studies on Nezam Abad tungsten mine, Markazi province, Iran. Unpublished M.Sc thesis (in Persian), University of Shiraz, Iran.

Shamanian Esfahani, G. H., Hedenquist, J.W., Hattori, K.H., Hassanzadeh, J. 2004. The Gandy and Abolhassani epithermal prospects in the Alborz magmatic arc, Semnan province, northern Iran. Eocnomic Geology, 99:691-712.

Shelton, K. L., Rye, D. M. 1982. Sulfur isotopic compositions of ores from mines Gaspe, Quebec: An example of sulfate-sulfide isotopic disequilibria in ore forming fluids with applications to the porphyry type deposits. Economic Geology, 77: 1688-1709.

Sillitoe, R. H. 1991. Intrusion-related gold deposits, in: Foster, R. P. Gold metallogeny and exploration. Blackie, Glasgow, 165-209.

Smith, M. P. and Yardley, W. D. 1996. The boron isotopic composition of tourmaline as a guide to fluid processes in the southwestern England ore field: An ion microprobe study. Geochimica et Cosmochimica Acta, 60: 1415-1427.

Stöcklin, J. 1968. Structural history and tectonics of Iran, a review. American Association of Petroleum Geologists Bulletin, 52(7): 1229-1258.

Takahashi, M., Aramaki, S. and Ishihara, S. 1980. Magnetite-series/Ilmenite-series vs I-type/S-type granitoids. Mining Geology, No:8, 13-28.

Thiele, O., Alavi-Naini., M., Assefi, R., Hushmandzadeh, A., Seyed-Emami., K., Zahedi, M. 1968. Explanatory text of the Golpaygan Quadrangle E7. 1:250,000. Geological Survey of Iran, 24p.

Thompson, J. F. H., Sillitoe, R. H., Baker, T., Lang, J. K. and Mortensen, J. K. 1999. Intrusion-related gold deposits associated with tungsten-tin provinces. Mineralium Deposita, 34: 323-334.

Tillman, J. F., Poosti, A., Rossello, S., Eckert, A. 1981. Structural evolution of Sanandaj-Sirjan Ranges near Esfahan, Iran. American Association of Petroleum Geologists Bulletin, 65: 674-687.

Waterman, G. C., Hamilton, R. L. 1975. The Sar Cheshmeh porphyry copper deposit. Economic Geology, 70: 568-576.

Whalend, J. B., Currie, K. L. and Chappel, B. W. 1987. A-type granites: geochemical characteristics, discrimination and petrogenesis. Contributions to Mineralogy and Petrology, 95- 407-419.

White, A. J. R., Chappell, B. W. 1977. Ultrametamorphism and granitoid genesis. Techtonophysics, 43: 7-22.

Winchester, J. A., Floyd, P. A. 1977. Geochemical discrimination of different magma series and their differentiation products using immobile elements. Chemical Geology. 20: 325-343.

Wood, S. A., Samson, J. M. 2000. The hydrothermal geochemistry of tungsten in granitoid environments: Relative solubilities of ferberite and scheelite as a function of T, P, pH, and m $_{Nacl}$. Economic Geology, 95: 143-182.

Appendix 1: Representative analyses of major elements of the main intrusions. For the Astaneh main phase and the Shirmazd microgranites, the marked samples, while for the other intrusions all the samples were used for drawing related diagrams. Mean represents data plotted in figures of chapter 2.

	SiO_2 wt% XRF	TiO_2 wt% XRF	Al_2O_3 wt% XRF	Fe_2O_3 wt% XRF	MnO wt% XRF	MgO wt% XRF	CaO wt% XRF	Na_2O wt% XRF	K_2O wt% XRF	P_2O_5 wt% XRF	(SO_3) wt% XRF	(Cl) wt% XRF	(F) wt% XRF	LOI wt%	SUM	Ti wt% XRF	K wt% XRF	P wt% XRF
Astaneh																		
Main phase																		
AS-9	63.40	0.52	16.00	5.84	0.10	2.73	4.49	2.66	2.51	0.11	<0.01	0.03	0.13	1.20	99.68	0.31	2.08	0.05
AS-10	63.82	0.51	16.02	5.64	0.10	2.75	4.44	2.7	2.51	0.1	<0.01	0.03	<0.05	1.02	99.66	0.31	2.08	0.04
AS-12	63.30	0.56	17.3	5.29	0.07	2.86	4.33	4.05	2.43	0.14	0.01	0.02	0.06	2.14	99.58	0.34	2.02	0.06
AS-16	64.73	0.53	15.78	5.85	0.08	2.53	3.26	2.51	2.67	0.11	<0.01	0.04	0.07	1.52	99.67	0.32	2.22	0.05
AS-28	58.66	0.50	15.87	8.45	0.18	4.85	6.35	1.9	1.65	0.08	<0.01	0.03	<0.05	1.12	99.65	0.30	1.37	0.03
AS-29	62.04	0.49	17.67	4.59	0.04	2.85	4.75	3.53	2.23	0.15	0.01	0.04	0.07	1.13	99.59	0.29	1.85	0.07
AS-44	59.81	0.44	15.65	7.84	0.17	4.81	6.48	1.92	1.36	0.07	0.01	0.03	<0.05	1.07	99.71	0.26	1.13	0.03
AS-48	65.66	0.49	15.53	5.12	0.10	2.32	3.67	2.46	2.83	0.11	<0.01	0.04	0.06	1.28	99.69	0.29	2.35	0.05
AS-56	63.38	0.56	15.66	5.84	0.13	2.74	3.71	2.6	2.52	0.12	<0.01	0.03	0.05	2.28	99.62	0.34	2.09	0.05
AS-61	63.66	0.52	15.66	5.93	0.10	2.86	4.63	2.64	2.57	0.11	<0.01	0.04	<0.05	0.92	99.68	0.31	2.13	0.05
AS-65	61.07	0.81	17.5	4.87	0.08	2.77	5.18	4.30	2.05	0.21	<0.01	0.03	<0.05	0.78	99.66	0.49	1.70	0.09
AS-66	63.60	0.55	15.61	5.99	0.10	2.69	3.93	2.39	2.44	0.12	<0.01	0.01	<0.05	2.22	99.66	0.33	2.03	0.05
AS-67	62.27	0.53	16.03	6.21	0.12	3.3	5.41	2.34	2.20	0.11	<0.01	0.04	<0.05	1.08	99.69	0.32	1.83	0.05
AS-71	59.37	0.52	15.75	8.65	0.19	4.72	6.04	1.70	1.54	0.09	<0.01	0.03	<0.05	0.97	99.61	0.31	1.28	0.04
AS-73	64.30	0.50	15.75	5.59	0.10	2.65	4.75	2.62	2.26	0.11	<0.01	0.03	<0.05	0.9	99.68	0.30	1.88	0.05
AS-75	65.01	0.50	15.82	5.53	0.09	2.73	4.21	2.55	2.32	0.11	<0.01	0.02	0.06	1.21	99.66	0.30	1.93	0.05
AS-76	63.71	0.52	15.30	5.76	0.10	2.78	4.74	2.66	2.30	0.12	<0.01	0.03	0.08	1.01	99.71	0.31	1.91	0.05
AS-78	64.64	0.50	15.90	5.61	0.11	2.68	4.23	2.59	2.61	0.11	<0.01	0.03	0.10	1.07	99.73	0.30	2.17	0.05
AS-79	54.72	0.40	15.46	9.68	0.24	6.75	8.06	2.62	1.25	0.05	<0.01	0.02	0.09	1.47	99.78	0.24	1.04	0.02
AS-80	63.99	0.50	14.20	5.65	0.10	2.69	4.56	2.71	2.41	0.11	<0.01	0.02	0.11	1.08	99.66	0.30	2.00	0.05
AS-106	63.45	0.50	15.73	5.55	0.11	2.58	4.69	2.58	2.74	0.10	<0.01	0.03	0.06	1.76	99.70	0.30	2.27	0.04
AS-107	63.45	0.50	15.55	5.70	0.12	2.81	4.29	2.49	2.71	0.10	<0.01	0.03	0.06	2.02	99.71	0.30	2.25	0.04
AS-108	63.17	0.54	15.44	6.03	0.12	2.67	4.60	2.52	2.61	0.11	<0.01	0.04	<0.05	1.58	99.64	0.32	2.17	0.05
Mean	62.83	0.57	15.97	5.72	0.10	2.80	4.68	2.77	2.45	0.12		0.03		1.57	99.67	0.34	2.04	0.05
Xenolith																		
AS-28	58.66	0.49	15.69	8.45	0.18	4.85	6.35	1.90	1.65	0.08	0.01	0.03	0.05	1.12	99.65	0.29	1.37	0.03
AS-71	59.37	0.52	15.86	8.65	0.19	4.72	6.04	1.70	1.54	0.09	0.01	0.03	0.05	0.97	99.61	0.31	1.28	0.04
AS-80	73.08	0.35	15.75	2.02	0.01	0.54	0.16	0.05	4.33	0.05	<0.01	0.01	<0.05	3.18	99.33	0.21	3.59	0.02
AS-109	77.36	0.07	16.00	0.41	0.01	0.18	0.12	1.48	7.08	0.01	0.01	0.01	<0.05	1.88	99.76	0.04	5.88	0.01

Appendix 1: Continued.

	SiO_2 wt% XRF	TiO_2 wt% XRF	Al_2O_3 wt% XRF	Fe_2O_3 wt% XRF	MnO wt% XRF	MgO wt% XRF	CaO wt% XRF	Na_2O wt% XRF	K_2O wt% XRF	P_2O_5 wt% XRF	(SO_3) wt% XRF	(Cl) wt% XRF	(F) wt% XRF	LOI wt%	SUM	Ti wt% XRF	K wt% XRF	P wt% XRF
Aplite																		
AS-8	73.08	0.35	15.55	2.02	0.01	0.54	0.16	0.05	4.33	0.05	<0.01	0.01	<0.05	3.18	99.33	0.21	3.59	0.02
AS-22	69.65	0.33	16.4	3.60	0.01	1.07	0.09	0.21	5.02	0.05	<0.01	0.01	0.06	3.00	99.50	0.20	4.17	0.02
AS-105	68.41	0.323	15.87	2.25	0.04	1.42	3.04	3.92	3.11	0.12	0.02	0.01	<0.05	1.10	99.62	0.19	2.58	0.05
Nezam Abad																		
Main phase																		
NZ-18	59.86	0.72	15.83	7.32	0.13	4.04	2.53	2.49	2.51	0.16	<0.01	0.02	0.07	3.64	99.32	0.43	2.08	0.07
NZ-21	57.02	0.82	15.90	7.70	0.14	5.17	5.58	2.46	2.70	0.17	<0.01	0.06	0.13	1.82	99.66	0.49	2.24	0.07
NZ-22	57.30	0.80	15.94	7.92	0.17	4.75	4.83	2.43	2.55	0.15	0.02	0.03	0.08	2.58	99.56	0.48	2.12	0.07
NZ-23	63.24	0.53	15.75	5.73	0.12	2.55	4.5	2.68	2.49	0.12	<0.01	0.03	0.08	1.94	99.74	0.32	2.07	0.05
NZ-24	55.80	0.75	16.04	7.79	0.15	6.22	7.74	2.19	1.70	0.12	<0.01	0.08	0.05	0.98	99.61	0.45	1.41	0.05
NZ-25	55.43	0.78	16.27	8.20	0.15	6.17	7.59	2.20	1.65	0.14	<0.01	0.07	<0.05	0.93	99.59	0.47	1.37	0.06
NZ-26	55.23	0.76	15.99	7.96	0.15	6.34	7.85	2.22	1.66	0.13	<0.01	0.06	<0.05	1.22	99.64	0.46	1.38	0.06
NZ-27	63.16	0.50	15.62	5.67	0.11	2.67	4.26	2.54	2.92	0.10	0.03	0.03	0.06	2.05	99.72	0.30	2.42	0.04
NZ-28	57.87	0.74	15.97	7.31	0.13	5.23	3.19	3.00	2.85	0.15	0.01	0.03	0.05	3.11	99.65	0.44	2.37	0.07
NZ-32	55.32	0.69	16.42	7.81	0.15	5.81	7.85	2.30	1.55	0.14	<0.01	0.06	<0.05	1.48	99.57	0.41	1.29	0.06
Mean	58.02	0.709	15.97	7.341	0.14	4.895	5.592	2.45	2.258	0.138		0.047		1.98	99.606	0.42	1.87	0.06
Aplite																		
NZ-51	73.20	0.07	13.68	0.74	0.02	0.16	0.59	3.54	5.54	0.17	<0.01	0.01	0.06	2.02	99.75	0.04	4.60	0.07
NZ-53	75.00	0.11	13.20	0.87	0.01	0.67	0.75	6.06	0.58	0.13	<0.01	0.01	<0.05	2.44	99.77	0.07	0.48	0.06
Mean	74.10	0.09	13.44	0.805	0.015	0.415	0.67	4.8	3.06	0.15		0.01		2.23	99.76	0.05	2.54	0.07
Goushe																		
GO-1	70.70	0.23	14.93	2.35	0.05	0.43	1.91	4.47	3.74	0.07	0.02	0.02	0.05	0.84	99.72	0.14	3.10	0.03
GO-2	72.80	0.18	14.00	1.83	0.05	0.32	1.65	4.12	3.92	0.05	0.02	0.02	0.05	0.76	99.77	0.11	3.25	0.02
GO-3	71.60	0.22	14.53	2.38	0.06	0.41	1.71	4.36	3.72	0.07	0.01	0.02	0.05	0.64	99.80	0.13	3.09	0.03
GO-4	71.50	0.21	14.61	2.24	0.05	0.39	1.71	4.28	3.98	0.07	0.01	0.02	0.14	0.70	99.85	0.13	3.30	0.03
GO-5	71.70	0.21	14.61	2.21	0.05	0.38	1.74	4.26	4.02	0.07	0.01	0.02	0.05	0.54	99.77	0.13	3.34	0.03
GO-6	72.10	0.21	14.38	2.26	0.05	0.40	1.68	4.20	3.88	0.07	0.01	0.02	0.08	0.55	99.83	0.13	3.22	0.03
Mean	71.73	0.21	14.51	2.212	0.052	0.388	1.733	4.28	3.877	0.067	0.013	0.02	0.07	0.67	99.79	0.13	3.22	0.03

Appendix 1: Continued.

Sample	**SiO_2 wt% XRF**	**TiO_2 wt% XRF**	**Al_2O_3 wt% XRF**	**Fe_2O_3 wt% XRF**	**MnO wt% XRF**	**MgO wt% XRF**	**CaO wt% XRF**	**Na_2O wt% XRF**	**K_2O wt% XRF**	**P_2O_5 wt% XRF**	**(SO_3) wt% XRF**	**(Cl) wt% XRF**	**(F) wt% XRF**	**LOI wt%**	**SUM**	**Ti wt%**	**K wt%**	**P wt%**
AS-1	70.02	0.35	15.22	2.36	0.03	1.17	1.32	3.82	2.83	0.10	<0.01	0.01	<0.05	2.44	99.64	0.21	2.35	0.04
AS-7	70.06	0.21	13.75	2.25	0.02	0.36	1.94	2.76	4.75	0.07	0.23	0.01	<0.05	2.70	99.15	0.13	3.94	0.03
AS-13	68.19	0.35	15.49	2.48	0.03	1.23	2.95	3.00	4.26	0.07	0.01	0.01	<0.05	1.48	99.58	0.21	3.54	0.03
AS-21	64.43	0.34	17.00	3.16	0.02	1.61	2.43	3.64	2.77	0.13	0.01	0.01	<0.05	3.99	99.57	0.20	2.30	0.06
AS-31	67.70	0.36	15.61	2.39	0.03	0.98	2.08	3.51	3.73	0.10	0.01	0.01	<0.05	3.12	99.62	0.22	3.10	0.04
AS-32	64.29	0.45	16.83	3.32	0.05	1.87	2.90	4.27	3.07	0.13	0.02	0.01	<0.05	2.36	99.60	0.27	2.55	0.06
AS-58	69.97	0.33	15.77	2.26	0.02	1.12	0.53	3.25	4.18	0.10	<0.01	0.01	<0.05	2.09	99.63	0.20	3.47	0.04
AS-63	63.28	0.51	15.92	5.52	0.08	2.76	3.11	3.32	2.89	0.11	0.04	0.02	0.11	1.91	99.56	0.31	2.40	0.05
AS-64	67.97	0.33	15.29	2.43	0.03	1.29	2.49	3.53	3.92	0.09	<0.01	0.01	0.11	2.23	99.73	0.20	3.25	0.04
AS-74	65.49	0.48	15.20	6.48	0.08	2.50	0.23	1.65	4.09	0.10	<0.01	0.01	0.11	3.19	99.51	0.29	3.40	0.04
AS-82	67.65	0.32	14.84	3.03	0.04	1.30	2.01	3.53	3.17	0.10	0.08	0.01	0.07	3.29	99.43	0.19	2.63	0.04
AS-86	64.52	0.41	16.05	2.59	0.04	0.76	3.53	3.30	3.55	0.12	0.01	0.01	0.12	4.65	99.66	0.25	2.95	0.05
AS-87	69.70	0.27	14.72	3.38	0.02	0.96	0.47	3.10	4.24	0.09	<0.01	0.01	0.05	2.10	99.09	0.16	3.52	0.04
AS-91	67.51	0.39	16.23	2.74	0.03	1.34	1.39	3.61	3.60	0.14	<0.01	0.01	0.05	2.60	99.62	0.23	2.99	0.06
AS-93	69.91	0.38	16.47	2.41	0.03	0.27	0.53	3.40	4.07	0.13	<0.01	0.01	0.05	1.93	99.62	0.23	3.38	0.06
AS-95	68.92	0.39	16.32	2.68	0.04	1.30	0.59	3.86	3.54	0.14	<0.01	0.01	0.07	1.84	99.68	0.23	2.94	0.06
AS-97	69.69	0.40	16.24	3.02	0.03	0.39	0.27	3.43	3.46	0.17	<0.01	0.01	0.12	2.32	99.50	0.24	2.87	0.07
AS-99	64.94	0.45	16.55	3.45	0.04	1.75	2.57	4.01	3.26	0.13	<0.01	0.01	0.05	2.20	99.42	0.27	2.71	0.06
Mean	68.78	0.35	15.6	2.73	0.03	1.02	1.32	3.43	3.76	0.11		0.01		2.27	99.49	0.21	3.122	0.05

Appendix 2: Trace element analyses of the Shazand granitoids. For the Astaneh main phase and the Shirmazd microgranites, the marked samples, while for the other intrusions all the samples were used for drawing related diagrams. Mean represents data plotted in figures of chapter 2.

	Rb ppm INAA	Cs ppm INAA	Sr ppm XRF	Ba ppm XRF	Y ppm INAA	Zr ppm XRF	Hf ppm INAA	Nb ppm XRF	Sc ppm INAA	V ppm ICP	Cr ppm INAA	Co ppm INAA	Ni ppm ICP	La ppm INAA	Ce ppm INAA	Nd ppm INAA	Sm ppm INAA	Eu ppm INAA	Th ppm INAA	U ppm INAA	Pb ppm ICP
Astaneh																					
Main phase																					
AS-9	109	10	175	318	32	118	3	5	16.6	107	62	14	24	24.7	42	18	3.3	0.7	11.4	2.9	9
AS-10	105	8	216	313	36	111	3	4	16.6	111	62	62	23	19.5	35	12	3.1	0.8	10.5	1.7	13
AS-12	154	23	217	306	38	137	2	10	11.8	99	53	53	22	17.0	27	11	2.0	0.5	7.4	2.9	<3
AS-16	101	8	169	350	20	131	2	7	16.5	108	55	55	22	20.9	42	15	3.3	0.7	9.2	3.5	13
AS-28	78	11	164	201	48	100	2	5	24.8	186	11	88	31	13.9	26	9	2.2	0.7	5.4	0.5	8
AS-29	115	13	381	530	16	141	2	10	7.4	63	31	31	30	11.1	18	9	1.7	0.6	5	1.7	<3
AS-44	67	8	179	188	28	50	2	<2	24.7	209	50	90	23	11.5	24	12	2.1	0.5	5.2	3	12
AS-48	101	7	166	349	23	132	3	9	15.3	100	43	43	21	22.4	41	16	3.3	0.8	9.7	1.8	31
AS-56	102	9	179	329	25	127	3	8	17.2	107	57	57	22	27.8	54	19	4.0	0.8	10.5	2.7	10
AS-61	105	8	168	306	32	127	2	6	17.8	105	66	66	21	20.5	41	18	3.5	0.6	11.5	2.1	8.5
AS-65	77	10	345	400	45	150	3	13	10.9	75	15	15	15	17.0	29	11	2.6	0.8	6.1	0.5	4
AS-66	89	8	180	303	37	120	3	8	16.8	100	57	57	23	27.9	52	20	3.8	0.7	14.4	0.5	13
AS-67	89	11	179	309	24	133	3	6	19.5	128	73	73	25	20.9	37	16	3.1	0.7	9.8	2.3	12
AS-71	70	7	162	262	26	102	3	6	24.4	191	161	161	35	16.2	31	15	2.7	0.9	5.5	1.8	7
AS-73	91	6	175	301	26	109	4	4	15.3	99	67	67	21	21.0	44	20	3.2	0.7	9.7	2.4	11
AS-75	101	9	165	287	33	111	2	6	15.6	95	64	64	23	23.6	46	20	3.5	0.9	9.5	2.2	11
AS-76	96	11	174	303	82	121	4	7	16.0	110	68	68	28	25.0	49	22	3.6	0.9	12	2.5	12
AS-78	105	8	168	307	27	114	4	8	15.0	102	62	62	21	18.2	39	16	3.4	0.8	10.1	2.3	10
AS-79	53	<5	164	134	83	81	3	4	24.5	164	347	347	84	17.8	46	17	5.4	0.5	5.8	0.5	10
AS-80	94	<5	178	303	62	114	4	7	15.2	103	60	13	25	25.6	50	19	3.2	0.9	10.5	2.8	10
AS-106	100	9	163	294	22	113	3	8	21.0	99	77	14	19	34.0	61	19	5.4	0.7	10.3	3	12
AS-107	105	6	155	278	19	111	2	6	22.0	101	74	21	20	29.0	38	16	4.5	0.6	11	3	7
AS-108	112	11	163	283	25	111	3	9	22.0	110	79	25	20	29.0	50	19	6.0	0.9	13.2	3	18
Mean	95.3	9.2	198	311	28.6	123	2.83	8.3	18.7	102.1	62.5	34.16	20.3	26.3	44.5	16.8	4.2	0.7	10.8	2.1	11
Aplite																					
AS-8	228	15	12	355	3	154	3	13	4.2	31	<5	<1	4	17.2	26	<5	1.8	<0.20	13.5	7.2	<3
AS-22	186	15	12	365	<3	109	2	6	4.6	39	7	11	4	6.5	13	6	0.9	<0.20	3.6	2.2	116
AS-105	104	11	292	8	<3	149	3	6	1.4	34	8	8	24	11.2	18	5	1.4	<0.20	4.9	1.3	5

Appendix 2: Continued.

	Rb	Cs	Sr	Ba	Y	Zr	Hf	Nb	Sc	V	Cr	Co	Ni	La	Ce	Nd	Sm	Eu	Th	U	Pb
	ppm	ppm	ppm	ppm	ppm	ppm	ppm	ppm	ppm	ppm	ppm	ppm	ppm	ppm	ppm	ppm	ppm	ppm	ppm	ppm	ppm
	INAA	INAA	XRF	XRF	INAA	XRF	INAA	XRF	INAA	ICP	INAA	INAA	ICP	INAA	INAA	INAA	INAA	INAA	INAA	INAA	ICP
Nezam Abad																					
Main phase																					
NZ-18	83	5	227	584	7	164	4	12	24.7	164	206	40	71	22.0	42	9	4.1	1.0	8	3	12
NZ-21	121	11	286	462	10	199	4	12	22.3	190	247	22	93	25.7	49	17	4.4	0.9	7.4	4	18
NZ-22	119	9	258	404	10	200	5	11	21.2	159	249	16	72	25.4	50	13	4.5	0.9	7.9	3	8
NZ-23	101	16	173	296	9	113	4	6	21.5	101	82	19	21	30.5	57	29	4.6	0.7	13.5	5	17
NZ-24	65	5	306	279	6	127	3	4	28.1	216	283	28	77	20.3	36	17	4.0	0.9	7	3	21
NZ-25	65	6	304	264	9	112	3	8	29.0	223	275	29	78	20.4	42	19	3.6	0.9	6.9	3	10
NZ-26	62	7	307	268	9	115	3	6	31.8	222	300	29	79	21.8	40	20	4.1	1.2	6.5	3	15
NZ-27	110	10	156	298	18	110	4	8	23.1	112	94	16	24	30.5	59	29	5.6	1.0	12.7	6	9
NZ-28	68	<1	185	559	9	152	5	7	23.3	157	275	25	90	30.3	59	22	4.9	<0.20	7.1	3	14
NZ-32	59	7	318	256	7	100	2	8	31.1	220	300	31	11	22.5	51	27	5.0	1.1	7	3	6
Mean	85.3	8.4	252	367	9.4	139	3.7	8.2	25.6	176	231.1	25.5	62	24.9	48.5	20.2	4.5		8.4	3.6	13
Aplite																					
NZ-51	169	7	95	213	6	160	<5	15	2.30	<5	18	<3	<3	6.70	12	<5	1.00	0.80	3.4	3	34
NZ-53	15	2	124	55	7	185	<5	16	3.80	<5	6	4	<3	19.30	46	12	4.10	0.90	7.9	4	3
Mean	92	4.5	110	134	6.5	173		16	3.05		12			13.00	29		2.55	0.85	5.65	3.5	18.5
Gousheh																					
GO-1	134	<1	114	270	18	154	5	10	4.70	9	16	3	6	20.00	36	16	4.10	0.20	14.2	7	23
GO-2	133	7	101	267	16	123	3	8	3.70	7	12	2	5	21.90	41	19	3.80	0.40	13.2	5	22
GO-3	144	6	112	283	18	155	5	9	5.60	9	<2	4	8	23.30	46	18	4.40	0.70	13.8	3	24
GO-4	146	10	109	309	20	133	3	8	4.30	8	8	3	2	21.10	37	19	3.70	0.50	12.1	3	23
GO-5	149	6	110	298	22	137	4	10	5.30	8	<2	3	3	25.10	54	20	5.10	0.40	13.6	3	28
GO-6	145	8	106	295	25	144	4	10	5.50	9	<2	4	4	26.30	53	15	4.90	0.20	15.6	3	26
Mean	142		109	287	20	141	4	9.2	4.85	8.3		3.2	4.7	22.95	44.5	17.8	4.33	0.40	13.8	4	24.3

Appendix 2: Continued.

	Rb ppm INAA	Cs ppm INAA	Sr ppm XRF	Ba ppm XRF	Y ppm INAA	Zr ppm XRF	Hf ppm INAA	Nb ppm XRF	Sc ppm INAA	V ppm ICP	Cr ppm INAA	Co ppm INAA	Ni ppm ICP	La ppm INAA	Ce ppm INAA	Nd ppm INAA	Sm ppm INAA	Eu ppm INAA	Th ppm INAA	U ppm INAA	Pb ppm ICP
Shirmazd																					
AS-1	137	6	137	299	24	143	3	17	4.6	34	16	4	12	20.7	34	15	2.7	0.5	11.1	2.5	4
AS-7	181	7	102	291	26	147	3	10	2.9	18	3	9	9	87.6	146	55	8.6	0.6	21.1	9.3	18
AS-13	160	8	244	427	12	135	1	7	5.6	38	12	6	10	13.6	22	7	1.5	0.5	7.5	2.8	3
AS-21	92	6	335	443	10	107	2	5	3.9	34	3	3	12	8.9	15	6	1.3	0.5	3.9	2.2	4
AS-31	164	8	136	368	18	147	3	11	4.6	31	3	6	9	20.8	34	12	2.3	0.5	12.2	2.8	3
AS-32	151	14	292	425	14	146	1	13	5.6	46	8	7	21	14.6	22	10	1.7	0.5	7.7	0.5	5
AS-58	149	7	143	340	19	138	2	14	4.6	25	11	6	9	16.7	27	10	1.7	0.4	16.2	2.6	<3
AS-63	162	12	177	305	24	113	2	8	5	111	70	13	23	23.4	43	16	3.8	0.7	11.8	4.8	9
AS-64	179	9	202	310	11	132	3	14	5	37	12	5	9	28.9	43	12	2.4	0.4	15.7	3.8	6
AS-74	156	8	49	397	60	73	4	6	5.4	181	224	14	30	25.4	58	31	6.2	0.8	8.7	1.7	28
AS-82	131	8	123	268	14	117	4	16	4.7	37	3	11	9	10.8	21	8	1.6	0.6	12.7	2.1	5
AS-86	118	8	154	386	9	141	4	12	5.1	41	8	6	11	13.4	22	-5	1.6	0.5	8.8	2	<3
AS-87	116	9	125	344	13	124	4	12	3.5	27	3	17	12	22.5	40	13	2.5	0.5	16.9	3.3	12
AS-91	139	8	163	396	22	148	4	12	4.4	36	12	5	14	19.4	34	16	2	0.5	10.7	1.4	<3
AS-93	150	8	135	425	15	156	5	15	4.3	32	5	6	8	20.4	38	13	2.4	0.5	12.3	1.6	4
AS-95	130	8	177	391	20	153	5	13	4.6	33	14	6	10	17.8	34	17	2	0.5	12.6	0.5	<3
AS-97	142	9	124	352	15	148	3	13	5.1	44	-3	9	13	23.9	42	17	2.7	0.5	10.6	2.9	12
AS-99	97	9	291	345	15	138	4	13	6	51	3	11	13	16.6	30	15	2	0.5	9.2	2.1	5
Mean	140.6	8	159.7	355	17.6	141.5	3.5	12.6	4.6	34.7	6.5	8.2	10.8	24.9	43.2	17.1	2.8	0.5	12.4	2.8	7.3

Appendix 3: Trace element analyses of the Au-bearing microgranitic rocks and mineralized veins of the Shirmazd Mountain, Astaneh Au prospect.

Sample	Au ppb INAA	Ag ppm ICP	As ppm INAA	Cu ppm ICP	Mo ppm ICP	Pb ppm ICP	Sb ppm INAA	Sn % INAA	W ppm INAA	Zn ppm ICP	Bi ppm XRF
Microgranite											
AS-1	57	0.40	13	145	<1	4	0.5	<0.01	<1	16	<3
AS-7	53	3.40	36	3486	13	18	0.9	<0.01	28	53	6
AS-13	313	0.40	3	410	2	3	0.4	<0.01	14	19	<3
AS-21	<2	<0.30	7	90	<1	4	1.0	<0.01	<1	11	13
AS-31	<2	0.60	24	418	3	3	0.9	<0.01	28	27	5
AS-32	20	<0.30	3	250	<1	5	0.1	<0.01	10	20	7
AS-58	5	0.50	8	221	<1	3	0.5	<0.01	12	15	13
AS-63	76	0.80	9	1044	1	9	0.6	<0.01	7	51	4
AS-64	21	0.40	15	268	<1	6	0.4	<0.01	<1	16	<3
AS-82	10	2.20	183	1912	2	5	1.3	<0.01	7	33	9
AS-86	<2	0.50	83	212	<1	3	1.7	<0.01	5	17	<3
AS-87	111	2.60	489	4266	5	12	7.9	<0.01	6	46	8
AS-91	<2	0.70	9	208	<1	3	0.8	<0.01	6	18	<3
AS-93	<2	0.40	53	289	<1	4	4.9	<0.01	9	14	6
AS-95	<2	0.30	6	101	<1	3	0.3	<0.01	<1	14	<3
AS-97	31	1.70	34	1551	3	12	1.9	<0.01	20	38	<3
AS-99	11	1.80	7	1789	4	5	0.7	<0.01	<1	36	<3
AS-100	83	0.37	1169	71	2	11	3.1	<0.01	2	16	15
AS-101	24	0.15	552	44	3	12	0.6	<0.01	2	17	6
AS-102	870	0.99	9024	214	<1	2	12.0	<0.01	18	12	<3
AS-105	21	0.14	42	130	<1	14	0.3	<0.01	6.8	12	<3
AS-106	9.2	0.09	20	54	<1	3	0.3	<0.01	30.0	62	<3
AS-107	26	0.14	37	114	<1	13	0.3	<0.01	9.2	36	<3
AS-109	27	0.14	88	100	<1	6	0.4	<0.01	3.4	18	<3
AS-110	44	0.23	33	180	<1	4	0.6	<0.01	9.5	16	<3
AS-111	47	0.31	12	275	<1	9	0.3	<0.01	5.4	6	<3
AS-113	280	0.47	14	380	<1	3	0.3	<0.01	13	17	<3
AS-114	100	0.40	26	370	<1	3	0.3	<0.01	13	11	<3
AS-115	34	0.15	129	150	<1	7	0.6	<0.01	5.8	58	<3
AS-116	40	0.26	59	205	<1	6	0.6	<0.01	4.4	47	<3
AS-117	95	0.32	84	287	<1	3	0.8	<0.01	4.9	68	<3
AS-118	95	0.26	92	190	<1	8	1.0	<0.01	5.5	12	<3
AS-119	185	0.39	130	225	<1	3	2.2	<0.01	6.0	10	<3
AS-120	60	0.34	95	245	<1	10	2.2	<0.01	7.6	9	<3
AS-121	47	0.57	305	305	<1	5	3.0	<0.01	4.9	18	<3
AS-122	47	1.40	206	1204	<1	4	2.2	<0.01	9.8	35	<3
AS-123	25	0.36	32	270	<1	3	1.8	<0.01	10	42	<3
AS-124	95	0.22	981	145	<1	8	2.6	<0.01	13	51	<3
Quartz-sulfide vein											
AS-8	1660	0.80	2470	99	<1	<3	143	<0.01	17.0	4	138
AS-104	1300	1.40	11675	369	3	4	28	<0.01	8.9	36	103
AS-108	3200	4.50	19344	1325	<1	2	98	<0.01	8.4	54	56
AS-125	1500	0.99	7767	254	<1	3	25	<0.01	27	11	36
Arsenopyrite vein											
AS-35	5750	4.80	160000	126	<1	27	279	<0.01	<23	<1	38
AS-103	6200	1.10	1042	475	4	6	4.20	<0.01	43	32	22
AS-112	7200	1.10	1042	475	<1	4	4.20	<0.01	43	14	110

Appendix 4: Electron microprobe analyses of sphalerite, Deh Hossein prospect.

Sample DH-13	**S wt%**	**Mn wt%**	**Fe wt%**	**Zn wt%**	**Cu wt%**	**Total wt%**	**FeS mol in Sph mol%**	**CuS in Sphalerite mol%**
1	32.96	0.01	7.83	57.32	0.37	98.49	7.26	0.28
2	33.10	0.02	8.07	56.94	0.38	98.50	7.44	0.29
3	33.09	0.01	7.90	57.31	0.29	98.60	7.30	0.23
4	33.20	0.01	8.19	56.69	0.73	98.81	7.52	0.56
5	33.27	0.00	7.95	57.02	0.59	98.82	7.30	0.45
6	32.92	0.01	8.22	56.63	0.53	98.30	7.60	0.41
7	33.28	0.01	8.06	57.04	0.12	98.50	7.39	0.09
8	33.32	0.01	7.96	56.93	0.13	98.35	7.30	0.10
9	33.33	0.00	8.24	56.96	0.42	98.95	7.54	0.32
10	33.37	0.01	7.97	56.76	0.71	98.82	7.30	0.54
11	33.22	0.01	7.79	57.10	0.40	98.51	7.17	0.30
12	33.33	0.01	8.67	54.95	1.82	98.77	7.90	1.37
13	33.45	0.00	8.13	56.83	0.50	98.91	7.41	0.38
14	33.46	0.00	8.29	56.53	0.53	98.80	7.55	0.40
15	33.29	0.00	8.19	56.00	1.02	98.50	7.50	0.78
16	33.40	0.02	8.39	56.49	0.59	98.88	7.64	0.45
17	33.58	0.02	8.05	56.89	0.56	99.10	7.32	0.43
18	33.38	0.02	7.82	56.77	0.51	98.51	7.17	0.39
19	33.32	0.03	7.97	56.28	0.94	98.55	7.31	0.71
20	33.30	0.02	8.25	56.40	0.97	98.93	7.55	0.73
21	33.34	0.01	8.55	56.53	0.98	99.41	7.79	0.75
22	33.34	0.00	8.54	56.46	0.98	99.32	7.79	0.74
23	33.03	0.00	8.24	56.69	0.94	98.90	7.60	0.72
24	33.41	0.00	8.19	56.51	1.02	99.14	7.48	0.77
25	33.28	0.01	8.19	56.67	1.00	99.14	7.50	0.76
26	33.28	0.00	8.14	57.01	0.98	99.41	7.46	0.74
27	33.17	0.00	8.38	56.59	0.88	99.03	7.69	0.67
28	33.23	0.00	8.15	57.08	0.91	99.37	7.48	0.69
29	33.17	0.00	8.00	56.27	1.34	98.77	7.36	1.02
30	33.41	0.00	7.96	56.97	0.45	98.79	7.29	0.34
31	33.48	0.03	7.71	57.43	0.19	98.85	7.06	0.15
32	33.30	0.02	7.70	57.04	0.15	98.22	7.08	0.11
33	33.44	0.02	7.72	57.29	0.25	98.71	7.07	0.19
34	33.48	0.02	7.77	57.10	0.69	99.06	7.11	0.52
35	33.63	0.01	8.11	55.47	1.75	98.98	7.37	1.31
36	33.26	0.01	8.12	55.97	1.44	98.81	7.45	1.09
37	33.50	0.02	7.77	57.18	0.19	98.66	7.11	0.14
38	33.36	0.01	7.78	56.69	0.68	98.51	7.14	0.51
39	33.36	0.00	7.98	56.72	0.43	98.49	7.31	0.33
40	33.31	0.00	7.87	56.01	1.56	98.74	7.23	1.17
41	33.39	0.00	7.90	56.63	0.88	98.81	7.24	0.67
42	33.13	0.00	8.19	56.23	1.10	98.64	7.53	0.84
43	33.44	0.00	8.09	56.19	0.91	98.63	7.39	0.69
44	33.24	0.00	8.06	56.46	0.79	98.54	7.40	0.60
45	33.31	0.01	8.71	55.33	1.68	99.04	7.94	1.27
46	33.37	0.00	7.83	56.24	1.15	98.60	7.18	0.87
Mean	**33.31**	**0.01**	**8.08**	**56.62**	**0.77**	**98.79**	**7.40**	**0.58**

Appendix 4: Continued.

Sample	**S**	**Mn**	**Fe**	**Zn**	**Cu**	**Total**	**FeS mol in Sph**	**CuS in Sphalerite**
DH-14	**wt%**	**wt%**	**wt%**	**wt%**	**wt%**	**wt%**	**mol%**	**mol%**
1	33.29	0.00	8.03	56.34	0.75	98.40	7.37	0.57
2	33.25	0.01	8.27	56.32	0.68	98.53	7.58	0.52
3	33.28	0.00	8.35	56.32	0.95	98.90	7.64	0.72
4	33.37	0.00	8.45	55.77	1.04	98.62	7.70	0.78
5	33.32	0.02	8.34	56.06	1.15	98.88	7.62	0.87
6	33.37	0.00	8.44	56.28	1.17	99.25	7.69	0.89
7	33.47	0.01	9.00	54.93	2.09	99.50	8.15	1.57
8	33.33	0.02	8.46	56.21	1.01	99.03	7.72	0.76
9	33.25	0.00	8.70	55.65	1.47	99.08	7.94	1.11
10	33.23	0.00	8.42	55.86	1.97	99.48	7.71	1.49
11	33.41	0.01	8.65	56.08	1.43	99.58	7.87	1.07
12	33.25	0.00	8.48	56.21	1.30	99.23	7.76	0.99
13	33.22	0.00	8.36	55.70	1.90	99.18	7.66	1.43
14	33.38	0.02	8.62	56.31	1.15	99.48	7.84	0.87
15	33.31	0.00	8.35	56.71	0.60	98.98	7.63	0.46
16	33.40	0.01	8.26	56.68	0.67	99.02	7.53	0.51
17	33.19	0.01	8.31	56.48	0.86	98.85	7.62	0.66
18	33.17	0.00	8.30	56.37	0.94	98.78	7.62	0.72
19	33.37	0.01	8.49	56.11	1.46	99.44	7.74	1.10
20	33.24	0.00	8.40	56.46	1.05	99.15	7.69	0.80
21	33.33	0.02	8.30	56.58	0.59	98.82	7.59	0.45
22	33.64	0.01	8.10	56.83	0.88	99.45	7.35	0.66
23	33.46	0.00	8.80	55.45	1.46	99.17	7.98	1.10
Mean	**33.33**	**0.01**	**8.43**	**56.16**	**1.15**	**99.08**	**7.70**	**0.87**
DH-18								
1	33.18	0.01	2.58	61.83	1.51	99.11	1.52	2.56
2	33.06	0.00	2.36	63.47	0.77	99.66	0.77	1.80
3	33.03	0.01	2.51	62.51	0.75	98.81	0.76	1.79
4	33.15	0.01	2.41	63.44	0.59	99.60	0.60	1.63
5	33.18	0.02	2.42	62.76	0.57	98.95	0.58	1.61
6	33.24	0.00	2.38	63.30	0.50	99.43	0.50	1.53
7	33.15	0.01	2.45	61.88	1.26	98.75	1.28	2.31
8	32.99	0.01	2.77	61.86	0.80	98.42	0.81	1.84
9	33.32	0.00	2.77	61.46	0.74	98.30	0.75	1.79
10	33.34	0.00	3.51	60.26	1.44	98.55	1.46	2.50
11	33.28	0.01	3.64	60.71	0.99	98.63	1.00	2.04
12	33.27	0.02	3.62	60.48	0.82	98.21	0.83	1.87
13	33.46	0.01	3.63	60.53	0.87	98.49	0.88	1.92
14	33.18	0.01	3.70	60.81	0.65	98.35	0.66	1.70
15	33.23	0.01	3.66	61.04	0.61	98.56	0.62	1.66
16	33.40	0.03	3.63	60.81	0.80	98.67	0.81	1.86
17	33.14	0.02	3.60	60.81	1.02	98.59	1.03	2.07
18	33.06	0.01	2.38	61.67	1.76	98.88	1.78	2.81
19	33.06	0.00	2.37	62.06	1.66	99.14	1.67	2.70
20	33.18	0.00	2.43	62.18	1.54	99.33	1.55	2.59
21	33.18	0.00	2.36	62.01	1.69	99.23	1.70	2.73
22	33.12	0.00	2.38	61.31	2.08	98.89	2.10	3.13
23	33.23	0.00	2.43	61.89	1.80	99.36	1.81	2.85
Mean	**33.19**	**0.01**	**2.87**	**61.70**	**1.10**	**98.87**	**1.11**	**2.14**

Appendix 4: Continued.

Sample DH-19	**S wt%**	**Mn wt%**	**Fe wt%**	**Zn wt%**	**Cu wt%**	**Total wt%**	**FeS mol in Sph mol%**	**CuS in Sphalerite mol%**
1	32.99	0.00	2.95	60.51	2.51	98.95	2.54	3.57
2	33.35	0.01	2.43	63.18	0.50	99.47	0.50	1.54
3	33.35	0.00	2.70	62.50	0.70	99.25	0.71	1.75
4	33.31	0.00	2.42	62.95	0.45	99.12	0.45	1.49
5	33.31	0.01	2.83	61.92	0.89	98.96	0.90	1.93
6	33.21	0.01	3.29	61.52	1.32	99.35	1.33	2.36
7	33.11	0.01	2.52	62.88	0.44	98.97	0.44	1.47
8	33.24	0.01	2.92	62.37	1.04	99.58	1.05	2.08
9	33.18	0.00	2.87	62.01	1.07	99.13	1.08	2.11
10	33.06	0.00	2.53	62.33	1.03	98.96	1.04	2.08
11	33.42	0.01	2.93	61.04	1.59	98.98	1.60	2.65
12	33.01	0.00	2.62	62.14	1.22	99.00	1.24	2.27
13	33.19	0.00	2.94	61.83	0.97	98.93	0.98	2.01
14	33.07	0.00	3.00	61.94	0.95	98.97	0.96	1.99
15	33.24	0.00	2.94	61.48	1.10	98.76	1.12	2.15
16	33.81	0.00	2.91	61.24	1.51	99.47	1.52	2.58
17	33.10	0.01	2.56	61.52	1.50	98.68	1.52	2.55
18	33.20	0.02	3.94	61.19	0.47	98.82	0.48	1.51
19	33.32	0.02	3.88	60.38	0.59	98.19	0.60	1.64
20	33.12	0.02	3.93	60.60	0.81	98.46	0.82	1.85
21	33.15	0.01	2.35	61.04	2.57	99.12	2.59	3.62
22	33.01	0.01	2.35	61.34	2.19	98.89	2.21	3.24
Mean	**33.22**	**0.01**	**2.90**	**61.72**	**1.15**	**99.00**	**1.17**	**2.20**

Appendix 5: Trace element analyses of representative samples of the Deh Hossein prospect.

	As	Cu	Mo	Pb	Sb	Sn	W	Zn	Au	Ag	Bi
	ppb	ppm	ppm	ppm	ppm	ppm	ppm	%	ppb	ppm	ppm
	INAA	ICP	ICP	ICP	INAA	INAA	INAA	ICP	INAA	ICP	INAA
Quartz-sulfide vein											
DH-1	194	5310	4	972	50	<100	<1	678	20	2	3
DH-2	6	34	<1	68	1	<100	10	125	<2	<0.3	75
DH-8	144	149	2	65	13	<100	29	45	28	1	700
DH-9	211	984	1	117	22	9700	20	161	34	2	44
DH-12	2030	10000	<1	64	48	<100	<1	179	<2	14	12
DH-15	1230	2090	<1	230	38	<100	62	580	84	48	<2
DH-16	633	1950	1	1270	38	<100	49	1520	<2	6	<2
DH-17	593	1610	3	46	15	<100	61	187	<2	2.00	<2
DH-18	29	10000	1	5000	141	<100	10	229	15	72	<2
DH-19	13200	107000	9	45	15	125	14	350	280	39	19
DH-20	4793	1105	3	40	102	34	50	190	180	3	2
DH-21	23200	2320	2	30	116	130	6	75	1360	19	200
DH-22	270	3165	3	205	3	500	22	725	36	2	<2
DH-23	24500	9100	3	2900	4	500	45	890	1300	91	16
DH-24	710	5050	4	1470	41	60	<0.50	530	200	3	320
DH-25	157	105	4	210	5	500	12	570	38	1	<2
DH-26	2010	4500	8	440	28	380	8	200	110	3	51
DH-27	1206	2020	6	90	1	350	18	350	82	2	2
Gossan											
DH-28	278	2039	<1	1064	36	150	4	413	34	<0.3	<2
DH-29	1380	2112	51	9793	66	<100	<1	7544	322	27	43
DH-30	16000	4383	<1	3930	1353	47200	150	2010	1101	99	916
Meta-sandstone											
DH-31	62	20	2	10	32	<100	6	280	<2	<0.3	<2
DH-32	52	45	<1	9	2	<100	<1	87	<2	0.50	<2
DH-33	35	67	<1	13	38	<100	12	73	<2	5	<2
DH-34	572	10	<1	222	9	43	19	2542	<2	44	19

Appendix 6: Abbreviations

amph	Amphibole
anda	Andalusite
ap	Apatite
asp	Arsenopyrite
au	Gold
bi	Native bismuth
bio	Biotite
bis	Bismite
bism	Bismuthinite
carb	Carbonate
cc	Chalcocite
chl	Chlorite
cpy	Chalcopyrite
cst	Cassiterite
cv	Covellite
ep	Epidote
fs	Feldspar
gn	Galena
lol	Löllingite
mal	Malachite
mr	Marcasite
ms	Muscovite
mz	Monazite
plg	Plagioclase
po	Pyrrhotite
PPL	Parallel nicols
py	Pyrite
qtz	Quartz
rt	Rutile
sch	Scheelite
scor	Scorodite
ser	Sericite
sph	Sphalerite
tour	Tourmaline
ttn	Titanite
XPL	Crossed nicols
Zr	Zircon

Curriculum Vitae: Mohammad Ali Nekouvaght Tak

Personal Profile

Name: Mohammad Ali Surname: Nekouvaght Tak

Date and place of birth: 17.09.1970, Tehran, Iran

E.mail: nekouvaght@gmail.com

Education

- April 2004-February 2008: Ph.D. in Economic Geology, Institute of Mineralogy and Mineral Resources, Technical University of Clausthal, Germany
- Oct 2003-April 2004: German language course, Interdaf Institute, Leipzig University, Germany
- 1993-1997: M.Sc. in Economic Geology, Faculty of Sciences, Shiraz University, Shiraz, Iran
- 1988-1992: B.Sc. in Geology, Faculty of Sciences, Tehran University, Tehran, Iran
- 1984-1988: Diploma degree, Mofid High School, Tehran, Iran

Work Experience

- June 1997-Oct 2003: Exploration geologist, Geological Survey of Iran, Tehran, Iran

Research Interest

- Hydrothermal ore deposits
- Intrusion-related Au-Sn-W mineralization
- Carbonate-hosted Pb-Zn deposits
- Boron and its role in granitic systems

Personal Affiliation

- Member of Geological Society of Australia
- Member of Society of Economic Geologists

Award

- Ph.D. fellowship, German Academic Exchange Services (DAAD)